Master of Science Thesis

A practical investigation into optimising port geometries to stabilise mixture ratios in hybrid rocket motors via additive manufacturing

ENGINE 2

SÊNOR CLAMP

AE5810: MSc Thesis

Roderick F. A. Wassenaar (4549074)

TUDelft

This page was intentionally left blank

Master of Science Thesis

A practical investigation into optimising port geometries to stabilise mixture ratios in hybrid rocket motors via additive manufacturing

by

Roderick Wassenaar

Student number: 4549074

to obtain the degree of Master of Science at the Delft University of Technology,
to be publicly defended on Thursday, 18 July 2024 at 10:00.

Thesis committee:	Dr. B. V. S. Jyoti,	Supervisor
	Dr. A. Cervone,	Chair
	Ir. M. C. Naeije,	External Examiner
Project Duration:	20 November 2023 - 4 July 2024	
Faculty:	Faculty of Aerospace Engineering, Delft	
Cover:	Cross geometry, test 1 (14 March 2024)	

TUDelft

This page was intentionally left blank

Preface and acknowledgements

This thesis marks the culmination of eight years of study at TU Delft, and there are many people I would like to thank as I close this chapter of my life.

First and foremost, I would like to thank my supervisor, Jyoti, for her initial intrigue and guidance in helping me find and shape my thesis topic. Her support and the freedom she granted me were invaluable throughout this journey.

My gratitude also goes to Rolf, whose thesis laid the foundation for my work. His willingness to answer my questions and our sanity-check video calls were crucial. I am also thankful to Dion for his seemingly endless knowledge about hybrid propulsion.

I am deeply appreciative to Barry, whose office door was always open - what were meant to be brief ten-minute chats often turned into enriching 1.5-hour discussions on various topics. Despite this, Barry always apologised for taking up my time, a sentiment I found quite ironic given that I often felt I was the one intruding on his busy schedule.

Thanks also to Johan and Viktor, the ACH technicians, who were always ready to help with any questions I had.

My journey as a student took unexpected turns, significantly shaped by my involvement with DARE. Starting as a part-time launch tower engineer for Stratos III, I moved on to a full-time role as propulsion engineer for Stratos IV. This led to being end-responsible for launch pad operations during the Stratos IV campaign, along with propulsion and roll control duties in mission control. I also had the honor of contributing to DARE in various capacities, from hybrid propulsion to roles on the Executive and Supervisory Boards, and as a Safety Officer.

While not directly involved with my thesis, the Stratos IV core team - Lucia, Andrew, Jasper, Jasper-Jan, Jillis, Willem, Nick, Sebastian, Niels, Nico, Alex, Nejc, Pjotr, and Sam - made Stratos IV an unforgettable experience. Without Stratos IV, this thesis might not have been possible.

For the thesis itself, there are too many people who contributed time and effort who I can thank individually, but there are a few mentions.

I would like to firstly thank the entirety of the Chimera team - in no particular order: Jesse, Mary, Martijn, Moana, Eugenio, Noa, Sartaj, Sil, Soham and Thijmen - who assisted me in manufacturing components, and conducting the tests necessary for this thesis, tests that would otherwise not be possible on my own. Special thanks to Niklas for part manufacturing, Christos for access to his regression tool, and Jonathan, Nathaniel, and Leo for their roles as Safety Officers during my tests. Additional thanks to Nick, Florian, and Alan for lending me last-minute feedsystem components or electronics equipment. I am also grateful to Wim, whose parallel thesis journey kept me motivated, and Mark, whose feedback for this thesis was invaluable (and whose cooking during DARE-related dinners I will definitely miss).

While DARE played a massive role in my student like, I would also like to extend my gratitude to the friends outside of DARE who played a significant role in shaping my student experience. Their companionship, support, and many shared moments were also an integral part of my life at TU Delft.

Finally, I extend my heartfelt thanks to my parents, twin sister, and brother for their unwavering support over the years, and to the rest of my family for their interest and encouragement in my endeavours at Delft and DARE.

Roderick F. A. Wassenaar (4549074)
Delft, June 2024

This page was intentionally left blank

Contents

This page was intentionally left blank

List of Figures

This page was intentionally left blank

List of Tables

This page was intentionally left blank

Acronyms

This page was intentionally left blank

Symbols

Symbol	Description	Unit	Pages
Roman letters			
A_{burn}	burning surface area	m^2	16
A_{exit}	nozzle exit area	m^2	15
A_{inj}	cross-section injector area	m^2	14, 15
A_{port}	cross-section port area	m^2	15
A_{throat}	nozzle throat cross-sectional area	m^2	43
C_d	discharge coefficient	–	14
C_F	thrust coefficient	–	43
G	mass flux	$\text{kg}\,\text{m}^{-2}\,\text{s}^{-1}$	5
G_{ox}	oxidiser mass flux	$\text{kg}\,\text{m}^{-2}\,\text{s}^{-1}$	5, 15
g_0	acceleration on Earth at sea level	$\text{m}\,\text{s}^{-2}$	15
I_{sp}	specific impulse, calculated	s	38, 47
$I_{\text{sp},v}$	specific impulse, vacuum	s	15
$\dot{m}_{\text{f}}$	fuel mass flow	$\text{kg}\,\text{s}^{-1}$	15, 16, 38, 47
$\dot{m}_{\text{ox}}$	oxidiser mass flow	$\text{kg}\,\text{s}^{-1}$	14–16, 38, 47
n	mass flux exponent	–	15
O/F	oxidiser-to-fuel ratio	–	16, 38, 47
P_{amb}	ambient pressure	Pa	15
P_c	combustion chamber pressure	Pa	14, 15, 38, 43, 47
P_{tank}	tank pressure	Pa	14, 16, 38, 47
R	specific gas constant	$\text{J}\,\text{kg}^{-1}\,\text{K}^{-1}$	15
$\dot{r}$	regression rate	$\text{m}\,\text{s}^{-1}$	15, 16
T	(fluid) temperature	K	16
T_c	combustion temperature	K	15
T_h	thrust	N	15, 43
Greek letters			
α	regression rate coefficient	$\text{m}^{1+2n}\,\text{kg}^{-n}\,\text{s}^{n-1}$	15
Γ	Vandenkerckhove function	–	15
γ	specific heat ratio	–	16
ρ	density	$\text{kg}\,\text{m}^{-3}$	14, 16
ρ_{f}	fuel density	$\text{kg}\,\text{m}^{-3}$	16

This page was intentionally left blank

Executive Summary

This thesis concerned further development on the design and testing of an ABS-N$_2$O hybrid rocket motor (HRM) and was performed at Delft Aerospace Rocket Engineering (DARE), a student rocketry team at Delft University of Technology (TU Delft).

At its foundation, HRMs - while safer to handle compared to their solid rocket motor (SRM) counterparts, and half the complexity compared to liquid rocket engines (LREs) - exhibit numerous disadvantages that have prevented wider adoption within commercial markets; in fact, outside of amateurs and student rocketry teams, adoption is close to non-existent. One such disadvantage concerns the shifting mixture ratio (also known as the oxidiser-to-fuel (O/F) ratio). This phenomenon, practically unique to hybrid rocket motors, changes the operating efficiency point of the rocket motor over the course of a motor burn.

Another such disadvantage concerns the generally slower regression rates - how quickly a fuel is consumed - compared to SRMs. This leads to the volume taken up by HRMs being greater compared to the performance they have, as well as having to be more slender for the equivalent performance from an SRMs. This last effect is especially challenging as this can affect the stability of rockets which use HRMss (as an example, it was this slenderness ratio that contributed to the roll-pitch coupling effect that caused DARE's Stratos III to have an in-flight anomaly in 2018).

To that effect, this thesis therefore mainly focuses on minimised the shifting of the mixture ratio by taking two different port geometries that, especially for SRMs, exhibit regressive burn profiles (double anchor and cross geometry). In other words, the peak performance occurs at the start of the motor test and decreases over time. These were chosen since the oxidiser used was N$_2$O, which is "self-pressurising", meaning no additional pressurant is required. Due to this characteristic, however, the oxidiser mass flow decreases over time, leading to the decision to have a greater burning surface area at the start of the test when compared to the end. In theory, both the oxidiser and fuel mass flow will decrease at similar rates, leading to a mixture ratio that is constant over time. It is due to the ability to use additive manufacturing (also known as 3D printing) that these geometries can be easily tested, since the traditional manner of casting hybrid rocket fuel can be a labour-intensive process with specialised moulds that would make iteration and optimisation an expensive endeavour.

In order to tackle the regression rate, a double hole geometry was also chosen as a testing geometry, which due to its multi-port nature, has a greater regression rate when compared to the reference geometry (which was the fourth, and last geometry chosen for this study). The outer dimensions, as well as the dimensions for the reference grain all came as a result from Wubben 2022 [1].

After a comprehensive literature study was performed to establish the feasibility and applicability of this technology, simulations were run to lay the groundwork in regard to the performance of the motor - in terms of the combustion chamber (CC) pressure performance, as well as its thrust. The O/F ratio was also examined, and as expected, the simulations indicated that for the regressive burn profiles, the mixture ratio was considerably more constant when compared to the reference geometry. A shift in the mixture ratio of approximately {0.7 [−]} was observed for the reference geometry, while for the double anchor and cross geometry, this was lowered to approximately {0.3 [−]} and {0.1 [−]}, respectively (at the cost of the mixture ratio itself lowering from around {6.5 [−]} to around {3 [−]}).

Three test campaigns were carried out, the first and third providing valid results for analysis. In the first test campaign, several methods for determining the mixture ratio were attempted, leading to the acquisition of additional sensors to reduce these uncertainties. The results themselves showed promise when compared to the simulation results, especially for the mixture ratio. For the third test campaign, the oxidiser mass flow (specifically) could be modelled with fewer assumptions, however due to several issues, only the double anchor and cross geometries provided sufficient analysable data to be compared. The results were nonetheless promising, however it is clear that without a direct measurement of the oxidiser mass flow, the methods employed to determine the propellant mass flows were heavily dependent on constants and design metrics, metrics that were calculated via external software packages, or otherwise assumed with no manner to verify their validity. These metrics were also the source of several numerical instabilities which led to having to change metrics such as the discharge coefficient of the injector manifold purely to have a stable numerical simulation.

The simulation and experimental results were also compared, and on the extreme end, an error in the range of {15 [%]} to {20 [%]} was fairly constant for the thrust and CC pressure, however results closer to the simulation was also present (in the range of {5 [%]}). This deviation changed over the course of the burn time of the specific motor test.

Ultimately, this study shows that it is possible to overcome some of the common disadvantages for HRMs, but a big limiting factor on assumptions concerning the modelling of the propellant mass flow had a great impact to the extent a definitive conclusion could be drawn. Nonetheless, with an improved model, the ability to measure the oxidiser mass flow directly and further testing, major optimisations are able to be performed which would give propulsion engineers another tool in their metaphorical toolbox to provide hybrid propulsion systems that meet performance requirements for in-space operations.

All data collected in this thesis can be requested from the author at `rfawassenaar@gmail.com`.

Introduction and Background Information

Building on previous work conducted by Wubben 2022 [1] and Whitmore et al. 2015 [2], this thesis aims to further develop the understanding of a HRM which employs ABS as its fuel and N_2O as its oxidiser. The foundational work that currently exists demonstrates the potential of this propulsion system, yet there remains significant room for optimisation and enhancement, especially surrounding some of the inherent disadvantages that HRMs have.

In section 1.1, the overview a history of rocketry propulsion is lightly touched upon, mostly highlighting the three major propulsion systems available for rockets - with each having respective benefits and drawbacks. Section 1.2 describes the umbrella project this thesis was performed under within DARE, and is followed by section 1.3 where the potential uses of this technology are described. Section 1.4 showcases some of the main downsides to the technology (which contributes to the lack of adoption of HRMs outside of amateur and student projects). Sections 1.5 and 1.6 illustrate what the goals of this thesis are, as well as the major requirements that restrict the project. Section 1.7 details the research objective (RO) and research questions (RQs) that will guide the research performed. The chapter finished with a conclusion in section 1.8, as well as a description of the structure of the remainder of the report - which can be found in section 1.9.

1.1. Overview and History

Within the field of rocketry, and more specifically propulsion, three main motor and engine types are used[1]. On the one side, the oxidiser and fuel components are mixed and stored into a single solid form. Known as SRMs, these are the simplest motors to use (once developed). This propulsion method cannot be stopped once the motor ignites, and increased care has to be taken when handling this type of rocket motor. Nonetheless, these motors can provide a great deal of thrust and is still a very common solution for launching large payloads into space as a first stage - one example being European Space Agency (ESA) and their (now no longer available) Ariane 5 (figure 1.1). Common SRMs propellants can include - within the amateur rocketry community - so-called KNSB (also known as rocket candy) which uses Sorbitol and KNO_3 to much more advanced such as Ammonium Perchlorate Composite Propellant (APCP).

On the other side of the spectrum, LREs use the fuel and oxidiser is a generally liquid state (with commercial companies, especially on the larger scale, opting for cryogenic temperatures). These engines combine propellants in a CC, and with an ignition source, these propellants combust. LREs are (theoretically) infinitely re-ignitable, the thrust can be throttled while the engine is running, and under the right design choices, have unlimited burn times. All major rocketry companies and organisations utilise LREs for their needs (such as SpaceX's Falcon 9, but also ESA's Ariane class of rockets to name but two). Compared to SRMs, these are more versatile, but also more complex due to the need for multiple feedsystems (not to mention that the propellants need to arrive in a precise order in the CC). Some fuels include RP-1 and CH_4, while two examples of oxidisers are liquid O_2 and H_2O_2.

---

[1]Propulsion methods such as electric propulsion is not included in this list since these propulsion methods are not in a state to launch rockets (and are more suitable as propulsion methods once the payload is in space).

Figure 1.1: Image of ESA's Ariane 5 rocket taking off with two SRMs as side-boosters. Image credit: ESA/CNES/Arianespace.

Within this spectrum, a third category of rocket motor uses a mix, namely an oxidiser in a liquid/gaseous state with its fuel in solid form. The fuel is cast (or otherwise) into a single, or multiple, grain(s). This combination is called a HRM[2]. This type of motor shares characteristics from both extremes of the propulsion spectrum. A feedsystem is required (although only half the complexity since the oxidiser is the only fluid that needs to be transported), while also requiring certain solid components such as fuel grains. They are also technically re-ignitable and can be throttled (more easily than SRMs).

Hybrid propulsion technology has fluctuated throughout history, but currently it is amateur and student rocketry that mostly utilise the technology. The bigger driving factors revolve around the ease of handling compared to other solid propellants, ease of acquiring components needed to make the fuel, as well as, arguably, a lower complexity to its liquid counterpart.

1.1.1. Hybrid rocket fundamentals

Figure 1.2 illustrates the core components necessary for a HRM on a rocket. Going from right to left, a pressurisation system with an oxidiser tank is needed. The pressurisation system ensures that the oxidiser is pushed to the CC. The pressurisation system can take many forms (high pressure N_2 or He is common), or properties from the oxidiser itself can also be taken advantage of. Pumps are also a possibility.

Next, a valve connects the oxidiser to the rest of the motor, and once the valve opens, the motor can be ignited with an ignition system (via an ignitor). Ignition occurs normally in the "pre-chamber", before the combusting products enters the fuel port of the motor and allows combustion to take place within the entire motor.

Some HRMs will also include a "post-chamber", and this is used to further encourage mixing and combustion. A "mixer" can sometimes be used to further encourage this process. Lastly, a nozzle accelerates the flow and produces thrust.
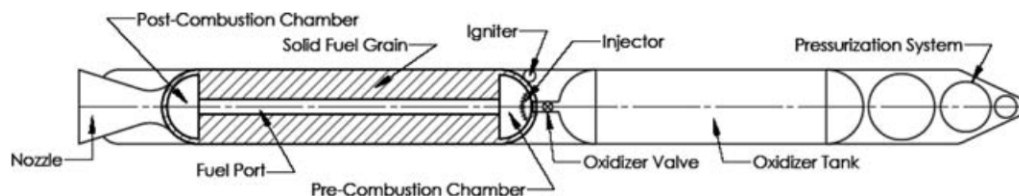
Figure 1.2: Basic schematic showing the different components required for a rocket using HRM technology. Source: Kuo and Chiaverini 2007 [3, pg. 39].

---

[2]The reverse, with a solid oxidiser and liquid fuel is also known as a reverse hybrid.

1.2. **Project Chimera and Project Inferno II**

The foundation of this thesis would not have been possible without the student rocketry team DARE - a student team associated with the TU Delft. DARE facilitates students of the TU Delft (and other educational institutions) to research and develop interests in various aspects of (amateur) rocketry. This ranges from research into propulsion systems to parachutes and other recovery systems; develop rockets with specific goals, as well as rockets to facilitate, as an example, the annual Dutch CanSat competition.

Within DARE, the hybrid rocketry team - Project Chimera - focus their attention on testing ABS-N_2O hybrids, specifically using liquid N_2O. This team started off, however, experimenting with the initial design that is also used for this study, and was founded Rolf Wubben, who wrote his thesis on a similar subject (which in itself was based on the second iteration of the roll control system for DARE's flagship rocket Stratos IV[3]). With the support of the Chimera team, Project Inferno II was founded for the purpose of this study, with the goal of experimenting with an ABS-N_2O system (using gaseous N_2O).

For this thesis, several testing campaigns were carried out which experimented with various port geometries - this was also partially done by Wubben 2022 [1] who tested a circular and spiral port geometry. For this study, three additional port geometries were tested with a specific aim to overcome potential deficiencies which have made HRMs unattractive for the wider commercial market. This research provides a stepping stone for further HRM optimisation for specific use cases, and provides propulsion engineers another tool to solve practical problems. The three geometries, specifically, are a so-called "double anchor" and "cross" geometry which were selected due to their regressive burn profile behaviour, while a "double hole" geometry was chosen in an attempt to increase the motor's regression rate. This is further touched upon in section 1.5.

This propulsive system, relying on additive manufacturing - a technology that is increasingly prominent within the engineering world - has the potential to optimise specific missions based on requirements in performance, mass or cost (amongst others), especially when applied to in-space propulsive missions. This does not even mention the added safety associated with HRMs when compared to the toxic chemicals used in most in-space propulsion systems (such as N_2H_4), or the added complexity when requiring feedsystems and infrastructure for the greener solutions that are slowly replacing the chemically-toxic systems.

Ultimately, HRMs can become a true contender in the current market dominated by LREs.

1.3. **Potential applications**

In-space propulsion systems provide several different purposes and can achieve different goals, depending on the specific mission. Since missions vary, requirements also differ, meaning the applicability of a HRM can be of relevance within a market that is mostly focused on LREs for all of its needs.

As established in Wassenaar 2023 [4, table 2.4], different categories of in-space propulsion can be created which are grouped among common requirements and performance characteristics. This is shown in table 1.1. Six different categories were established, ranging from high impulse and thrust manoeuvres, to variety in thrust and performance requirements, as well as different numbers of re-firings required. Additionally, table 1.2, also from Wassenaar 2023 [4, table 3.1], aims to quantify, in a back-of-the-envelop approach, parameters such as the change in velocity or the number of restarts that a specific category might require.

Table 1.1: General characteristics of the semi-arbitrary in-space propulsion categories [4, table 2.4].

Category	General characteristics
ADCS	Many refirings, general short burst to be used during the entirety of the mission, accuracy is paramount
De-orbiting	Two or three refirings, at the end of the vehicle's life, does not have to be too accurate
Planetary ascent/descent vehicles	High impulse and thrust, one to several firings of the propulsion system
Inter-planetary orbit transfer	High impulse and thrust, potential long burn times (depending on exact propulsion performance)
Intra-system orbit transfer	Two refirings minimum, variable impulse and thrust
Greater manoeuvres	Great variability in thrust, impulse, refirings - ultimately depends on the use-case

Ultimately, the literature study concludes that the categories that require an extreme number of restarts (namely Attitude Determination and Control System (ADCS) and "Body hopping") would not be feasible for this motor technology since the number of restarts demonstrated by Whitmore and Walker 2017 [5] are far below the order-of-magnitude requirements for these types of missions. The burn time limit was left as more of an open

---

[3]https://dare.tudelft.nl/stratos4/

Table 1.2: Summarising table for back-of-the-envelope performance requirements [4, table 3.1].

Category	ΔV $\left[\mathrm{m\,s^{-1}}\right]$	Number of restarts [-]	Burn time [s]
ADCS	70	350	0.5 to 50
De-orbiting	250	3	Variable
Ascent/Descent vehicle	100 to 2×10^3	2 to 5	100 to 500
Inter-planetary transfer vehicle	5.3×10^3	5 to 7	Variable
Final orbit manoeuvres	3.9×10^3	4	Variable
Body hopping	Variable	50	Variable

question since the requirements can vary drastically, and for a hybrid system, it is primarily limited by the amount of propellant loaded onto the spacecraft (ignoring potential e.g. thermal issues that could arise from very long burn times).

The categories of "Final Orbit Maneouvres" and "De-orbiting" were established to be categories that could be served well by this technology. In the de-orbiting case, the number of times the motor would have to ignite would be only a handful, and if the motor performs slightly better, or slightly worse than expected, this would not hinder the mission (assuming sufficient safety margins are put in place). This system could even be combined with a N_2O cold gas ADCS system, and once the mission is complete - and with greater pressure being put on corporations to not clutter up Earth's orbital environment - the ignitor can be activated to give the satellite the final push to be put into an orbit that removes all debris that would otherwise be left from the satellite.

1.4. Disadvantages of hybrid rocket motors

While HRMs have advantages, it is ultimately clear that several major disadvantages exist for the technology, which fundamentally has played its role in this technology being popular among mostly student teams such as DARE, while not showing any presence in the commercial market (although a handful of companies such as HyImpulse in Germany, and Delta V from Türkiye (at time of writing) are attempting to create commercial products with HRM technology).

One major disadvantage, also established by Whitmore, Peterson and Eilers 2011 [6] comes down to an increased difficulty in getting consistent results. The fuel grains have to be manufactured consistently (and tightly controlled), the ignition has to also be consistent, and oxidiser pressure inherently affects the performance, both during the entire motor burn time, but also depending on if the motor is firing for the first time, or if it has already been fired previously. The oxidiser can also impact performance - since no external pressurant is used, the pressure of the N_2O is entirely dependent on its temperature, which therefore needs to be regulated sufficiently well for consistent, predictable performance. For LREs, this is less of an issue. Most LREs will use a pressurant to control the pressures, and once the firing sequence and timings with the various valves has been worked out, these systems can end up being extremely consistent (and therefore, great indicators for performance).

Another disadvantage can be that the technology tends to also take longer to reach an equilibrium (should it reach an equilibrium at all!). Barato 2013 [7] discusses this as one of several contributing factors for less-wide adoption, especially in the area of fine motor control. On top of this, as explained by Pastrone 2012 [8], the mechanism that HRMs operate under requires the fuel to heat up, and this physical delay leads to HRMs having slower transients when compared to LREs - this can impact the versatility of the technology, since options such as throttling end up being less responsive.

One other major aspect of HRMs is the fact that the O/F ratio will shift over time. In a motor setup, the regression rate - the rate at which the fuel gets consumed - is directly linked with the oxidiser mass flow, but also with the port area (see equation (2.4)). Due to this, even with a constant oxidiser mass flow, the regression rate will most likely decrease (the rate of which will depend on the particular coefficients and exponents which are determined experimentally) over time since the port area increases. But, while the regression rate might decrease, the total surface area that is available to burn will also change. Using a simple circular port, the surface area will increase as the port expands. The ultimate effect is that the ratio of the oxidiser and fuel will change over time, which has the effect that the motor will not be running at its most effective point. It is particularly this that will drive this project's testing goals.

The regression rate can also be seen as one of the disadvantages of HRMs. Since this rate is lower compared to

SRMs, a large surface is generally needed to produce the equivalent amount of performance, leading to HRMs needing to be longitudinally bigger, which can lead to metrics such as fuel loading being worse. Different approaches exist to enhance this characteristic (and further discussed in Pastrone 2012 [8]), but strategies such as having multiple ports and various (metal) additives are common choices to enhance a HRM's regression rate.

Nonetheless, modelling the regression rate is already a complicated phenomena, since the factors that influence the regression rate depends, amongst others, on a parameter called the mass flux (often denoted as G). Figure 1.3 shows this. Depending on the mass flux, the CC pressure can have a greater impact on regression rate, so certain assumptions have to be made, or improvements to the ballistics model will have to be considered in order to accurately model this behaviour. For the remainder of this project, an assumption will be made that the regression rate is constant longitudinally over the whole motor. This allows certain simplifications to be made, namely that the mass flux is based on the mass flow entering the motor, also known as the oxidiser mass flux, denoted by G_{ox}.
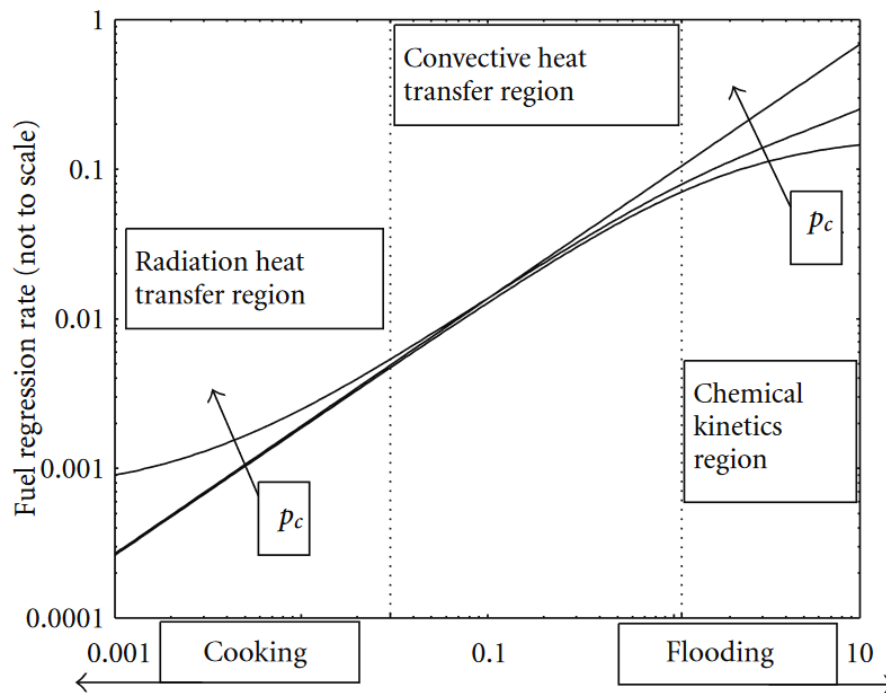
Figure 1.3: Regression rate behaviour for HRMs depending on operating regime. Source: Pastrone 2012 [8, fig. 2].

1.5. Project Goals

While a HRM is combusting, its O/F ratio (using a standard circular port geometry) will shift over time. This will have an effect on parameters such as combustion temperature, but also on its specific impulse etc. Wubben 2022 [1, fig. 3.9] created several graphics to outline the impact of a varying mixture ratio, shown in figure 1.4.

In order to try to counteract this problem, the project took inspiration from particular geometries undertaken in SRM design, namely the port geometry. Several different geometries are shown in figure 1.5. These different geometries can be classified under three general terms: progressive, neutral and regression burn profiles. Progressive burn profiles, such as the geometry indicated as the "tubular configuration" in figure 1.5 increases its thrust over time. A neutral burn profile can be achieved with e.g. the star configuration, the thrust is more constant over time. The regressive burn profile, however, such as the double anchor geometry, has most of its performance at the start of the motor burn, and generally decreases over time.

Since it is known *a priori* that N_2O will be used without a pressurant, meaning the oxidiser mass flow decreases over time, regressive burn port geometries were taken as inspiration for trying to flatten the O/F ratio shift during a motor firing. Since these geometries have a great amount of surface area (and therefore burning fuel) at the beginning of a motor test, and a smaller surface area later, the mixture ratio, in simple terms, shift less. This is further explained in chapter 2. The geometries chosen were therefore the "double anchor" and "cross" geometries.

One disadvantage of HRMs that has not yet been mentioned are their generally lower regression rates. This
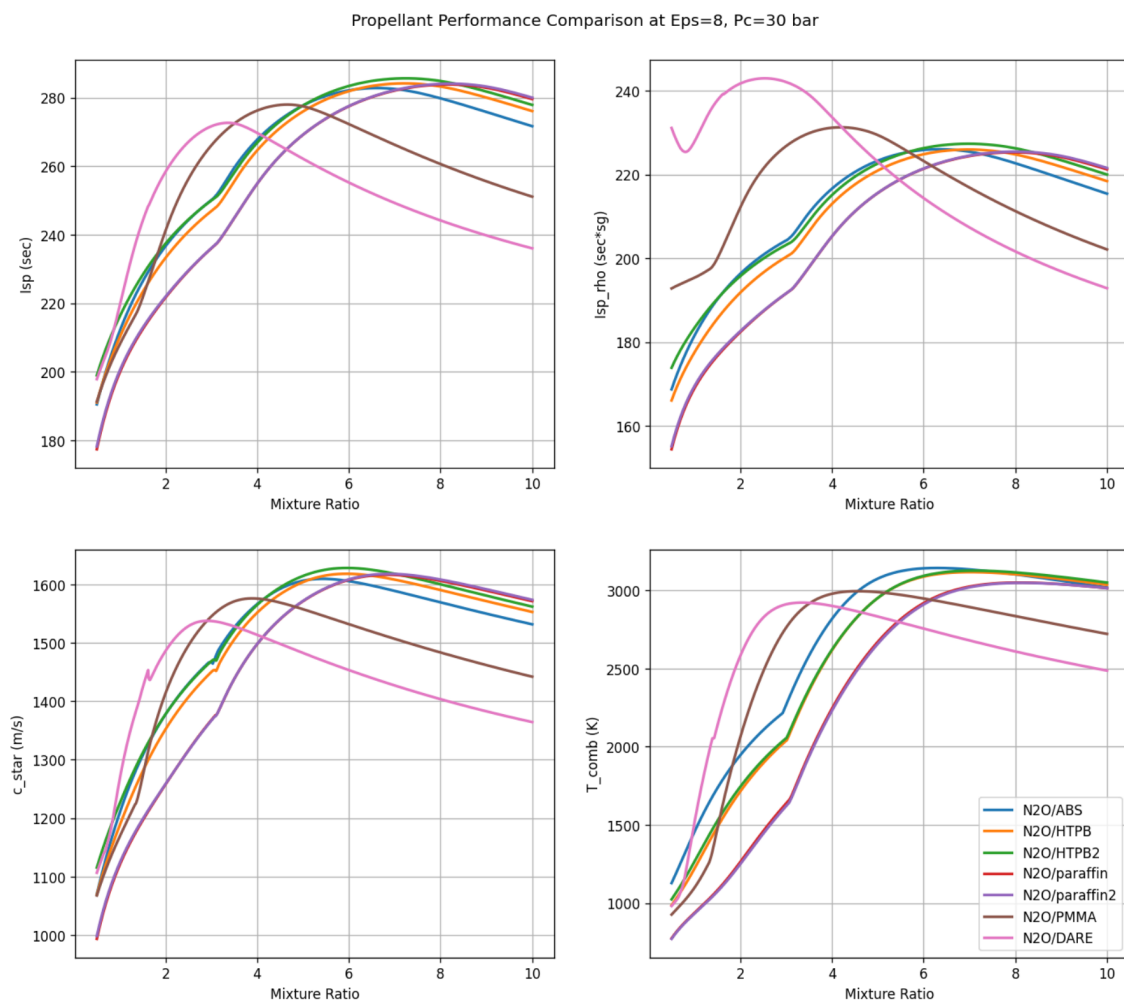
Figure 1.4: Performance curves of selected fuels over a range of mixture ratios. Source: Wubben 2022 [1, fig. 3.9]).

1 = Tubular configuration   2 = Rod & tube configuration
3 = Star configuration   4 = Cross configuration
5 = Double anchor configuration   6 = Multi-fin configuration
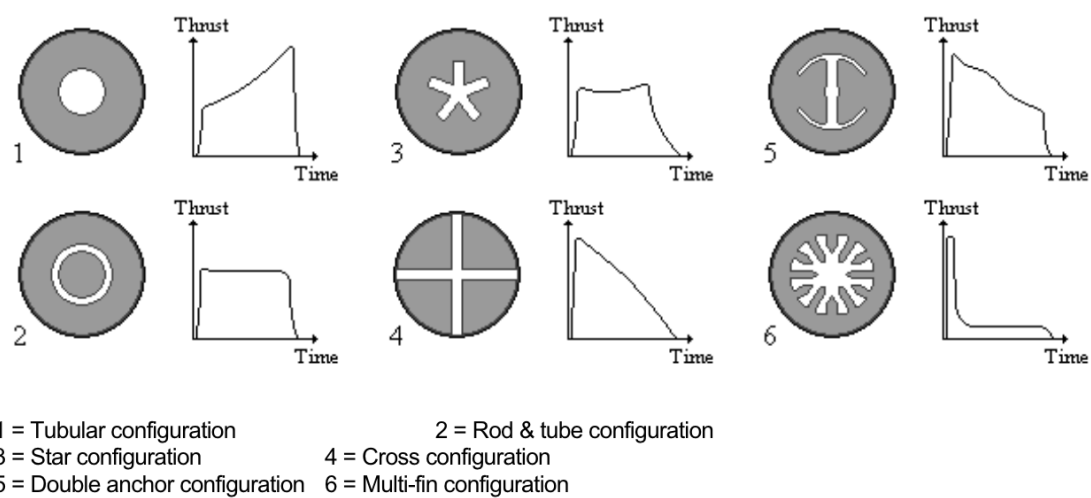
Figure 1.5: Internal-burning charge designs with their thrust-time programs. Source: Zandbergen 2022 [9, fig 7].

ultimately influences burn time for rockets, and is a contributing factor to the slender nature of the HRM-powered rockets launched by DARE - the burn times need to be longer to extract a similar performance compared to a SRM. In order to counteract the generally lower regression rate, especially in HRMs, multiple ports can be used which allow faster burning times. A HRM project, among others, using a multiple-port geometry was attempted by Story et al. 2003 [10]; this motor was capable of producing approximately {1.1 [MN]} of thrust. This project came with its own unique engineering challenges and was not developed further. A higher regression rate, for this project, will be treated via the "double hole" grain geometry.

At its heart, this project will aim to investigate these disadvantages, and explore whether additive manufacturing can be taken advantage of for this purpose. If this turns into a feasible solution, optimisations can be run which would allow engineers to further tailor performance needs into their motor designs which would otherwise have to be achieved in a more complex way with the current market solutions.

1.6. Requirements

Several requirements are set which dictated how the project would commence. These requirements are high-level, and were based on the requirements formulated in Wassenaar 2023 [4]. Some requirements were also based on Wubben's work and carried over to this project. Specifically, the equipment used and the outer dimensions of the HRM are kept the same.

One of the most critical requirements dictated the scale of the testing available for this thesis. The TU Delft has various locations available for test, with each location having its own set of testing requirements (most critical being maximum allowable noise (in dB) for the surrounding environment). Therefore, any testing should adhere to the requirements associated with this location. By default, this will also require any testing to be approved by DARE's Safety Board - including the presence of a DARE Safety Officer (SO) during testing whose sole responsibility is the safety of the people, equipment and surrounding environment - as well as any TU Delft personnel whose purview this experiment falls under.

Another requirement dictated the scale of the project in terms of hardware and software. On the hardware front, the majority of the testing equipment (elaborated on in appendix F) is owned by DARE - this puts limits on the information that can be collected during a test. The addition of more sensors is possible, provided they fall within the budget provided by the university. On the software front, for the Data Acquisition system (DAQ), DARE owns a National Instruments (NI) compact Reconfigurable Input Output (cRIO) (9035 model) which uses a 2019 version of LabVIEW to operate tests and collect sensor data. A version of the testing software was written by Wubben which will act as a foundation.

Lastly, the system itself shall use ABS as its fuel with N_2O as its oxidiser.

1.7. Research Objectives and Questions

First, a RO with associated RQs is established. The ground work for this was done during the literature study (Wassenaar 2023 [4]). The RO for this study will be:

> Investigate the effectiveness of using additive manufacturing for geometrical changes to ABS-N_2O HRMs that lead to wider adoption of the technology for in-space propulsive applications.

With this experimental study, additive manufacturing technology is used to alter the performance of the HRMs that were tested, with the explicit goal of counteracting some of the known problems present in HRMs (touched upon in section 1.4). In order to achieve this, the following RQs are established.

> 1. What categories of in-space propulsion applications can benefit from ABS-N_2O HRMs?
>   (a) Which characteristics can be deemed relevant to judge a propulsive system's appropriateness for various in-space propulsion applications?
>   (b) Which characteristics from HRMs are inherent advantages and disadvantages of the technology?
>   (c) Which class of in-space propulsive applications can benefit from 3D printed ABS-N_2O HRMs?

The first RQ establishes the foundation for this study, especially the inherent trade-off made with HRMs. Supported by the literature study performed, the different applications and requirements for propulsion systems are established and evaluated, especially to the extent where the technology used in this thesis can be ultimately

adopted for wider use in industry.

While the first RQ establishes a more theoretical basis, an experimental approach can be taken to investigate the RO, which establishes a need to also consider, practically, the feasibility of the research and how that can be achieved.

> 2 Which design parameters, within a grain geometry, can be altered to increase the suitability of ABS-N_2O HRMs for specific propulsive needs?
>
>> (a) Which design parameters can be altered that can facilitate test campaigns within TU Delft and DARE testing limitations?
>>
>> (b) What theoretical metrics can be used to determine the effectiveness of a particular design?
>>
>> (c) Which characteristics can be determined with the available test suite?
>>
>> (d) To what extent is it possible to establish the effectiveness of these changes from experimental data?
>>
>> (e) To what extent do the current testing limitations affect the ability to draw concrete conclusions about the impact of the changes made to the designs?

The second RQ deals with the technology in a practical sense. It is relevant to establish all the parameters that are available to the author that can alter a motor's performance, and how one can determine whether the changes made had the impact that was expected. Theoretically, many different parameters can be altered, however testing limitations are present - it is therefore also equally relevant that realistic expectations be set for how the changes can be measured with the sensors available. It should also be realised that particular parameters will have to be modelled since these cannot be measured; this ultimately means that an inherent uncertainty and inaccuracy will be present, and it should therefore be looked at how great this discrepancy might be after the experimental phase, and how these uncertainties can be reduced with different testing setups.

1.8. Conclusion

In conclusion, hybrid propulsion technology has generally taken the back seat when it comes to the adoption of propulsion technology in the commercial space, however, especially with the advent of 3D printing, it does not have to be this way.

The first RQ, repeated below, can already be answered.

> 1. What categories of in-space propulsive applications can benefit from ABS-N_2O HRMs?
>
>> (a) Which characteristics can be deemed relevant to judge a propulsive system's appropriateness for various in-space propulsion applications?
>>
>> (b) Which characteristics from HRMs are inherent advantages and disadvantages of the technology?
>>
>> (c) Which class of in-space propulsive applications can benefit from 3D printed ABS-N_2O HRMs?

Several characteristics have been proposed to judge a propulsion system's suitability for in-space applications. Seen in tables 1.1 and 1.2, the amount of performance a motor can provide, how long it is expected to burn for and how many times it can restart are a concrete foundation on what the expected performance metrics can be when an organisation is looking for a propulsion system. Depending on the mission requirements, the propulsion system is defined, and by extension, there are categories of missions where hybrid technology is suitable.

In terms of advantages and disadvantages of HRMs, their inherent safety and lower complexity can offer satellite designers more flexibility in designing their subsystems, not to mention the potential of mass savings. This does not mean that the technology is perfect - having a consistent performance will require extensive testing and modelling - however if this is combined with the right mission category, this can be less important than a mission where e.g. pointing accuracy is critical.

Therefore, with a mission where a satellite will have to e.g. de-orbit, a thrust profile can be established that respects other requirements from the mission (e.g. acceleration limits). Additive manufacturing has the potential to be a very versatile solution for such a use case.

1.9. **Report Structure**

For this report, chapter 2 details the simulations performed which laid the groundwork for this research, both in the manner in which the regression of the fuel grains was performed, as well as the ballistics model. The assumptions that had to be made for this model are also discussed (including potential impacts).

Chapter 3 details the manufacturing and testing process for this thesis. Both testing campaigns are described, including the lessons learned from the first campaign, and how these lessons impacted the later campaign and tests. The test data collected is also assessed and evaluated in its usefulness.

Chapters 4 and 5 depict the two test campaigns, showcasing the data collected, and how particular parameters such as the O/F ratio behaved for the different motor configurations. The individual motors are also compared amongst themselves with several metrics.

Chapter 6 evaluates the original model with the test data. Several small changes are made to make the simulation as representative to the conditions experienced during the test.

Chapter 7 explores the conclusions of the work performed, including future research recommendations.

This page was intentionally left blank

2
Simulations

In order to achieve the goals and objectives set out in this thesis, simulations are performed. This simultaneously provides information on expected performance (and whether the design changes affect what is expected), but also after-the-fact provides information whether particular assumptions are valid. This can also indicate whether there exists a fundamental knowledge gap.

In this chapter, therefore, the model is described with its various equations. The initial results of the simulation are not presented, but instead are included and discussed in section 4.1.

A regression model was used to describe how an arbitrarily shaped port geometry regresses over time. This is described in section 2.1. The ballistics model follows this regression model, and is described in section 2.2. Lastly, core assumptions made in the model are described in section 2.3.

2.1. Regression model

In order to simulate the ballistics of a HRM, there are various levels of complexity. For this thesis, since multiple different port geometries are being tested, this needs to be modelled. It stands to reason that the easiest to model would be a circular port, however it gets significantly more complex with arbitrary shapes.

In order to tackle this, a DARE in-house tool, written by Margaritis 2023 [11], was used. The tool itself had the original goal of simulating SRMs, and is split into two parts - the regression model, and the ballistics model. Therefore, the regression model part of the tool will be used, with a separate ballistics model for a HRM (this is further explained in section 2.2).

The grain regression part of the tool has been verified by comparing the results to various analytical solutions. Analytical solutions of grain regression were compared to the results from the simulation tool. Most common cases of grain core geometry elements were covered. Analytical solutions of constant regression for the total burn area, port area, wet area and web thickness of Bates, square, slot and star cores were derived and subsequently compared to the results produced by the tool. In addition to this, a simple case of variable regression of a cylindrical core was analytically described, which was also used to further verify the tool [11].

The regression tool starts by taking a .STL file as the core geometry. All grain geometries (including the core) can be found in figures G.1a to G.1d. This allows the user to input (in principle) an arbitrary core geometry. The grain dimensions are subsequently input. For this thesis, the outer diameter of a grain is {39.5 [mm]}. The grain regression behaviour can be seen in figure 2.1.

A mesh is generated and this is regressed via a constant regression depth. Every regression depth, a new mesh is generated. During this process, information such as the area of the port and the burning surface area are computed. This information is ultimately used in a later step in the ballistics model, described in section 2.2. For the rest of this project, this tool will be taken as a black box, treated similarly to e.g. third-party Python packages and assumed to produce reliable results.

Once the testing is complete, the regression shape, over time, can be compared to pictures of the grains to visually compare whether the tool describes the regression accurately.

(a) Reference grain regression over arbitrary time.

(b) Double anchor grain regression over arbitrary time.

(c) Cross grain regression over arbitrary time.

(d) Double hole grain regression over arbitrary time.
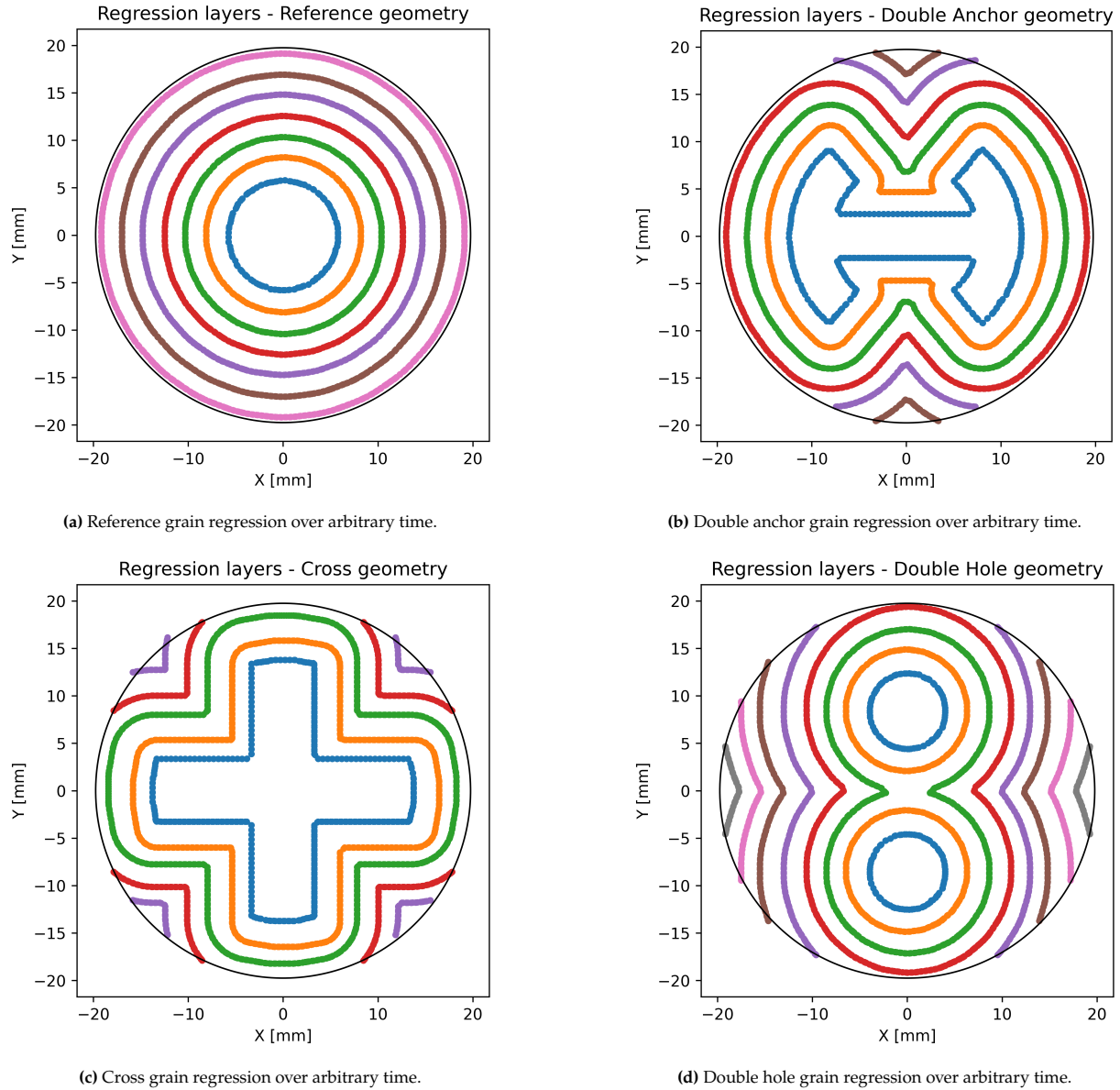
Figure 2.1: Time-independent geometry regression based on the simulations written by Margaritis 2023 [11]. The black outline dictates the outer diameter of the grain.

2.2. Hybrid ballistics model

The hybrids ballistics model is responsible for modelling the internal behaviour of the design HRM. Taking the regression data from the regression model detailed in section 2.1, every time step (taken to be {0.001 [s]}) calculates the various parameters that dictate the performance of a rocket engine. In this case, the parameters are the CC pressure and thrust, as well as the O/F ratio.

The temporal simulation begins by requesting the current port area from the data in the regression model. This is the first step in figure 2.2. The second step linearly interpolates tank pressure for every time step. The values for every second are found in table 2.1.

The third step uses a Python module CoolProp [12] to calculate the N_2O density based on the pressure in the tank from the previous step, and assumes a constant temperature of {20 [°C]}. The temperature assumption will be a source of discrepancy.

For the initial simulations, with a burn time of {4 [s]}, and following the pressure trend in figure 2.3a, the density of gaseous N_2O starts at {120 $\left[\text{kg m}^{-3}\right]$} which drops to around {100 $\left[\text{kg m}^{-3}\right]$} at {34 [bar]} [13]. In reality, due to the oxidiser density acting under a square root (equation (2.1)), with everything else being equal, a {15 [%]} deviation at most can be expected. For initial simulations this will be accepted.
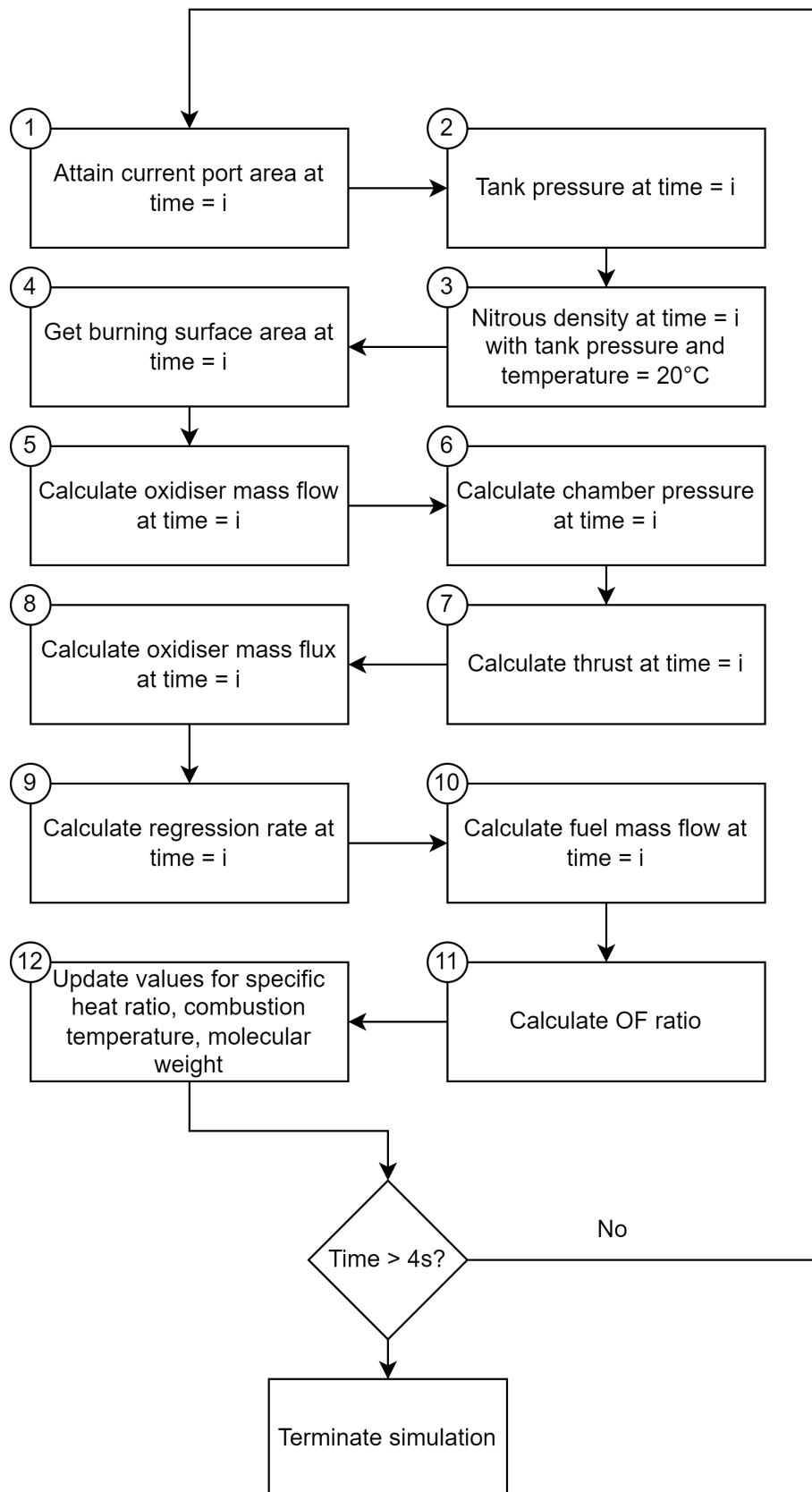
Figure 2.2: Flow diagram for the modelling of the HRM ballistics.

Table 2.1: Tank pressure over time based on historical data from Wubben 2022 [1].

Time [s]	0	1	2	3	4	5	6	7	8
Pressure [bar]	44	41.5	39	36.5	34	31.5	29	26.5	24

While the run-tank empties, the oxidiser will cool down to as much as below the freezing point of water (depending on how long the emptying process occurs for). In this process, the density of the gaseous phase will decrease (by as much as a factor of two) while the liquid phase - assuming some is present - will increase in density.

Figures 2.3a and 2.3b showcase the behaviour of the temperature and density of N_2O over a range of pressures. In the graphs, going from right to left can be treated as the run-tank emptying, which means the temperature drops, with this also affecting the density of the different phases of the oxidiser. The graphs were generated under saturation conditions over a range of pressure values.
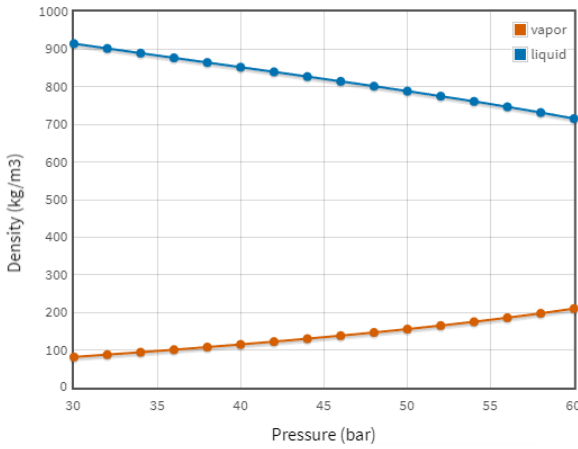
(a) N_2O pressure versus density.
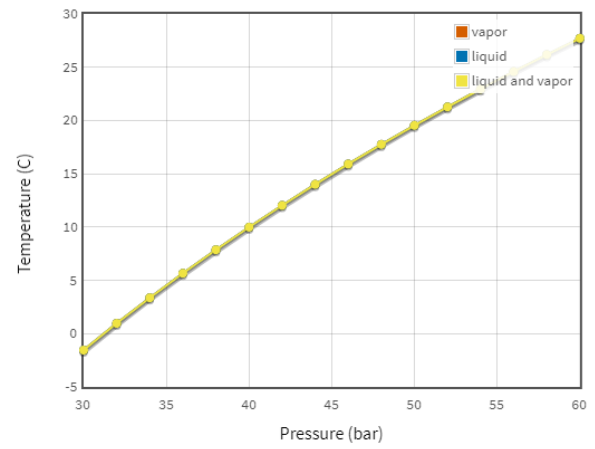
(b) N_2O pressure versus temperature.

Figure 2.3: N_2O behaviour of density and temperature over pressure range. Source: Eric W. Lemmon et al. 2023 [13].

The fourth step, similar to the first step, attains the total burning surface area from the regression model.

$$\dot{m}_{\text{ox}} = C_d \cdot A_{\text{inj}} \cdot \sqrt{2\rho \cdot (P_{\text{tank}} - P_c)} \tag{2.1}$$

where $\dot{m}_{\text{ox}}$: oxidiser mass flow $[\text{kg s}^{-1}]$
        C_d : discharge coefficient $[-]$
        A_{inj} : cross-section injector area $[\text{m}^2]$
        ρ : density $[\text{kg m}^{-3}]$
        P_{tank} : tank pressure $[\text{Pa}]$
        P_c : combustion chamber pressure $[\text{Pa}]$

Step five, by using equation (2.1), calculates the oxidiser mass flow per time step. This requires several assumptions. In the first time step, the CC pressure is at ambient. The density of the oxidiser is taken from step three, while the tank pressure is taken from step two. The discharge coefficient for the entire system is assumed to have a value of {0.3 [−]}. This is based on Wubben 2022 [1, fig. 7.20], where the discharge coefficient is at {0.3 [−]} at a tank pressure of {40 [bar]}. At this stage, the discharge coefficient is modelled to remain constant. If the discharge coefficient was modelled with the line-of-best-fit, as shown in Wubben 2022 [1, fig. 7.20], for the initial simulation the discharge coefficient would increase from {0.3 [−]} to around {0.36 [−]}. This is an increase of around {20 [%]} (with everything else remaining equal). Since the discharge coefficient increases by {20 [%]}, while the oxidiser density decreases by around {15 [%]}, this should counteract each other and have a negligible effect on the results.

$$P_c = \frac{(\dot{m}_{ox} + \dot{m}_f)\sqrt{T_c \cdot R}}{A_{inj} \cdot \Gamma} \tag{2.2}$$

where			
	P_c	: combustion chamber pressure	[Pa]
	$\dot{m}_{ox}$	: oxidiser mass flow	[kg s^{-1}]
	$\dot{m}_f$	: fuel mass flow	[kg s^{-1}]
	T_c	: combustion temperature	[K]
	R	: specific gas constant	[J kg^{-1} K^{-1}]
	A_{inj}	: cross-section injector area	[m^2]
	Γ	: Vandenkerckhove function	[−]

Step six (via equation (2.2)) calculates the CC pressure (which will be used in the next time step for step five). In the initial time step, the fuel mass flow will be zero, and an assumed combustion temperature of {2500 [K]} was chosen semi-arbitrarily. This was based on the bottom-right graph in figure 1.4. The specific gas constant was taken to be {299 [J kg^{-1} K^{-1}]}. This value was attained in initial simulations via RocketCEA (a Python wrapper of NASA's CEA code [14], written by Taylor 2024 [15]), via the `get_IvacCstrTc_ChmMwGam` function[1].

The Vandenkerckhove function take the specific heat ratio of the combusting products as input - the initial value was taken to be {1.3 [−]}, as used in Newlands 2012 [16], since the first time step will only include N$_2$O. Most of these parameters (namely the combustion temperature, specific gas constant and Vandenkerckhove function) are updated in step 12.

$$T_h = (\dot{m}_{ox} + \dot{m}_f) \cdot I_{sp,v} \cdot g_0 - P_{amb} \cdot A_{exit} \tag{2.3}$$

where			
	T_h	: thrust	[N]
	$\dot{m}_{ox}$	: oxidiser mass flow	[kg s^{-1}]
	$\dot{m}_f$	: fuel mass flow	[kg s^{-1}]
	$I_{sp,v}$	: specific impulse, vacuum	[s]
	g_0	: acceleration on Earth at sea level	[m s^{-2}]
	P_{amb}	: ambient pressure	[Pa]
	A_{exit}	: nozzle exit area	[m^2]

The thrust is calculated via equation (2.3) as step seven. A (vacuum) specific impulse of {255 [s]} is assumed in the first time step. This was chosen based on the top-left graph in figure 1.4[2]. Since the vacuum specific impulse is taken, this will over-estimate the thrust performance (under the assumption that the propellant mass flow is accurate). Based on the original NASA CEA written by Gordon and Mcbride 1994 [14, pg. 27, eq. 6.9], the vacuum specific impulse incorporates the pressure term (with no ambient pressure). This will still overestimate the thrust. This will be a constant difference equal to the ambient pressure and the nozzle exit area[3]. This comes out to a deviation of {4.5 [N]}. This is the second half of equation (2.3).

$$\dot{r} = \alpha \left(\frac{\dot{m}_{ox}}{A_{port}}\right)^n = \alpha G_{ox}^n \tag{2.4}$$

where			
	$\dot{r}$	: regression rate	[m s^{-1}]
	α	: regression rate coefficient	[m^{1+2n} kg^{-n} s^{n-1}]
	$\dot{m}_{ox}$	: oxidiser mass flow	[kg s^{-1}]
	A_{port}	: cross-section port area	[m^2]
	G_{ox}	: oxidiser mass flux	[kg m^{-2} s^{-1}]
	n	: mass flux exponent	[−]

Steps eight and nine are calculated via equation (2.4). As input for the regression rate, the oxidiser mass

---

[1] A CC pressure of {40 [bar]}, a mixture ratio of {7.6 [−]} and a nozzle expansion ratio of {3.61 [−]} was used. The function outputs the combustion products' molecular weight of {27.8 [g mol^{-1}]}. This value is used to divide the universal gas constant of {8.3145 [J mol^{-1} K^{-1}]} to get the aforementioned (initial) specific gas constant.

[2] A sensitivity study was conducted to determine the influence of this initial guess - the impact was negligible.

[3] The ambient pressure is taken to be {1 [bar]} and the nozzle exit area being {4.5×10^{-5} [m^2]}.

flux is calculated based on the oxidiser mass flow and the port area (taken from step one). The regression rate coefficient and mass flux exponent are required to model the regression rate - these are taken to be $\{0.312\,040 \times 10^{-3}\ [\text{m s}^{-1}\,\text{kg}^{-n}\,\text{m}^{2n}\,\text{s}^{n}]\}$ and $\{0.2722\ [-]\}$ respectively, as reported by Wubben 2022 [1] and Whitmore 2018 [17].

$$\dot{m}_\text{f} = \dot{r} \cdot \rho_\text{f} \cdot A_\text{burn} \tag{2.5}$$

where	$\dot{m}_\text{f}$	:	fuel mass flow	$[\text{kg s}^{-1}]$
	$\dot{r}$	:	regression rate	$[\text{m s}^{-1}]$
	ρ_f	:	fuel density	$[\text{kg m}^{-3}]$
	A_burn	:	burning surface area	$[\text{m}^2]$

Step 10 calculates the fuel mass flow based on the regression rate, the density of the fuel (remaining constant at $\{1040\ [\text{kg m}^{-3}]\}$ [1, table 3.2]) as well as the burning surface area calculated in step four. For a circular port - the reference geometry - this would be the equivalent of the surface area of a cylinder, excluding both ends. This calculation does not take into account the burning surface area of the pre-chamber - but it is assumed to be negligible compared to the rest of the grain.

$$\text{O/F} = \dot{m}_\text{ox}/\dot{m}_\text{f} \tag{2.6}$$

where	O/F	:	oxidiser-to-fuel ratio	$[-]$
	$\dot{m}_\text{f}$	:	fuel mass flow	$[\text{kg s}^{-1}]$
	$\dot{m}_\text{ox}$	:	oxidiser mass flow	$[\text{kg s}^{-1}]$

Step 11 calculations the O/F ratio based on the oxidiser and fuel mass flows. This value then gets used in step 12 and the Python package RocketCEA to get updated values for the specific heat ratio, combustion temperature and molecular weight (which affects the specific heat ratio). The simulation will continue until a burn time of $\{4\ [\text{s}]\}$ is reached.

2.3. Assumptions and tools

For the initial model used (prior to any testing), several assumptions had to be made, namely knowing tank pressure over time. There are several methods to attain this - one model detailed by Newlands 2012 [16] utilises the isentropic equations, models N_2O as a real gas (including a compression coefficient) and iterates per time step. This relies on guessing a compression coefficient. The general flow chart for this calculation is shown in figure 2.4.

While this gives the most flexibility in terms of modelling, it will nonetheless introduce errors. Therefore, a second approach will be taken in the initial simulations. This relies on knowing the tank emptying process *a priori*. Data acquired from Wubben's testing campaigns were used as input (namely table 2.1). This significantly eases the isentropic relationship steps as the only assumptions that remain is the specific heat ratio, and that the emptying of the tank does not include a (significant) phase change of N_2O - in other words, that the run-tank remains filled with gaseous N_2O during the emptying process. This will no longer be valid once attempts are made to explicitly use the liquid phase of N_2O as this is not an isentropic process [16].

$$\frac{T_2}{T_1} = \left(\frac{P_\text{tank,2}}{P_\text{tank,1}}\right)^{\frac{\gamma-1}{\gamma}} = \left(\frac{\rho_2}{\rho_1}\right)^{\gamma-1} \tag{2.7}$$

where	T	:	(fluid) temperature	$[\text{K}]$
	P_tank	:	tank pressure	$[\text{Pa}]$
	ρ	:	density	$[\text{kg m}^{-3}]$
	γ	:	specific heat ratio	$[-]$

Since the run-tank pressure data is known *a priori*, and the ambient temperature is also known, the density of N_2O can be determined at the start of the simulation. Then, via equation (2.7), the density over time can be simulated since the start pressure and density are known, as well as the tank pressure at an arbitrary time step, meaning the associated density of the N_2O at an arbitrary time step is known. As mentioned above, this

Guess Z based on previous time iteration's P2

Calculate T2 based on Zguess

Calculate P2 based on T2

Calculate Z based on P2

Zguess less than Z?
increase Zguess slightly and loop back

Zguess greater than Z?
decrease Zguess slightly and loop back

Zguess equal to Z? (to a set percentage)
Done, exit loop
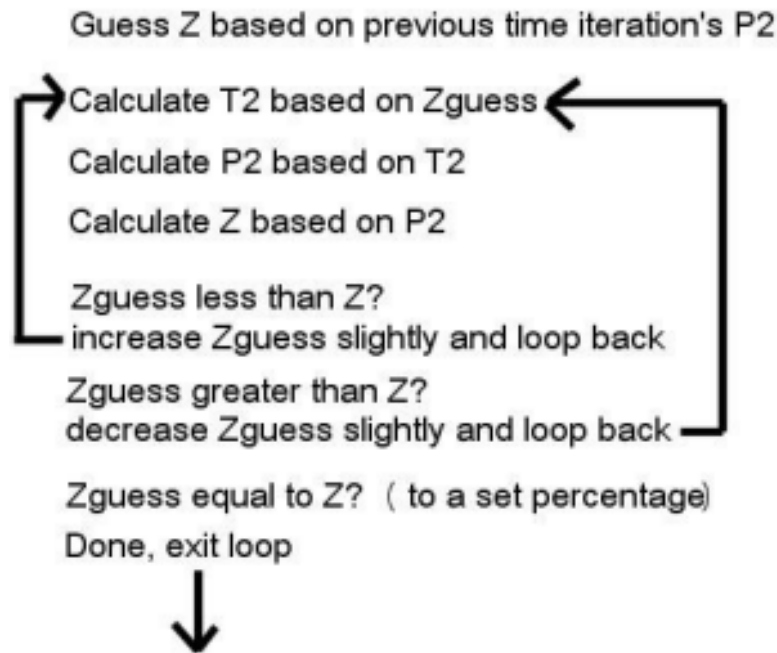
Figure 2.4: Iterative loop to attain compression coefficient per time step in modelling an emptying N_2O tank [16, pg. 6].

relies on the assumption asserted by Newlands 2012 [16] that the emptying of a gaseous N_2O run-tank can be modelled accurately (enough) as an isentropic process.

Another assumption relies on a constant discharge coefficient. For the entire system (run-tank to CC), a value of {0.3 [−]} was taken. This corresponds to Wubben's data for the start pressure. One indication about this accuracy of this assumption shall be the oxidiser mass flow. This should come out to around {20 $\left[g\,s^{-1} \right]$} [1].

The last assumptions are that the freestream total pressure - which corresponds to the initial CC pressure - starts with a value of {1×10^5 [Pa]}, and that the expansion ratio of the area of the throat to the area of the exit of the nozzle remains constant. In Wubben's work, the graphite nozzle degraded over time, however isostatic graphite was taken for this study which should be able to withstand the conditions during firing. The throat of the nozzle is set to {4 [mm]} while the exit diameter is {7.63 [mm]}[4]. If during the experiment the nozzle degradation warrants it, this assumption shall be adjusted accordingly.

RocketCEA is used for modelling some characteristics within the internal ballistics of a HRM. This is step 12 in figure 2.2. Parameters such as the specific heat ratio, combustion temperature and molecular weight (as well as performance indicators such as specific impulse and the characteristic velocity) are calculated based on several inputs - namely the CC pressure, the O/F ratio and expansion ratio. The package also requires the ABS to be defined as fuel. The same definition that is found in Wubben 2022 [1, app. C.1] was taken. This is valid since the same ABS filament was used as with Wubben's experiments[5].

2.4. Conclusion
Ultimately, a DARE-developed regression tool was combined with a hybrid ballistics model to simulate the performance of the different grain geometries. The model was described by its analytical equations, including the input from the Python packages RocketCEA and CoolProp. The assumptions and tools used were also described, and their potential impact on the results were assessed.

---

[4]This project ultimately had a design iteration on the graphite nozzle. One effect of this was that, while the divergent angle remained the same, the divergent section itself became longer, resulting in an exit diameter of {8.43 [mm]}.

[5]123 3D - ABS Grijs - `https://www.123-3d.nl/ABS/1-75-mm-ABS/Grijs-p7359.html` - Accessed May 2024.

This page was intentionally left blank

<div style="text-align: right; font-size: 3em;">3</div>

Manufacturing and Testing

In this chapter, the manufacturing and testing process will be treated. Manufacturing is showcased, including the difficulties experienced during the process.

The testing process is also discussed. For each set of tests, the goals are mentioned, followed by the calibration information, as well as an evaluation regarding the usability of the data. The further processing and analysis of the data will be handled in chapters 4 and 5.

It should also be noted, in this chapter, the first test campaign (also referred to as the first test) consisted of one test day on 14 March 2024. The second test campaign consisted of two test days (and is also referred to as the second and third test days). These happened on 24 April 2024 and 7 May 2024. The biggest changes occurred between the first and second test campaign. This incorporated design improvements of the system, as well as the addition of sensors to reduce the uncertainty in the data analysis.

Section 3.1 (and its associated subsections) detail the first test campaign, including the manufacturing process and the test setup. The data collected is analysed and assessed regarding usability, including the calibrations associated with the sensors used. Improvements for the later tests are also touched upon.

Subsequently, section 3.2 details the second test campaign in a similar fashion with section 3.1, incorporating the improvements from the initial test campaign. The data is assessed again for usability, and the calibrations applied to the data for the two test days are also presented.

3.1. Campaign 1

The first test campaign served several objectives, and consisted of one day of testing (in March 2024). The objectives, in no particular order:

- Provide data and affirm the design changes made as a "proof-of-concept".
- Perform a design cycle in case the grains (or testing components) did not perform as expected.
- Show whether there were limitations in the data collected, and whether improvements could be made.
- Showcase whether alterations need to be made to the testing procedures in regard to the data collected that is used for analysis.

3.1.1. Manufacturing and test setup

For the first test campaign, some equipment was usable from the work of Wubben 2022 [1], however this only allowed one motor testing at a time. Since several configurations were to be tested, and a limited possibility to test, three more motor testing units were manufactured. This would allow all geometries to be tested in one day, without the need to remove the fired motor and replace with a new grain on the test day itself.

There were also several changes compared to Wubben 2022 [1]. The first was the change made to the graphite nozzle. While the internal geometry would remain the same, the process to manufacture the graphite nozzle was time-intensive and required very precise, angular tolerances (in the order of $\{\pm 0.1 \ [°]\}$. This design was changed to incorporate an updated steel retainer (figure 3.9b) and a graphite nozzle that had perpendicular surface angles (on the exterior). This did still require a high-tolerance dimension (with a maximum allowed

deviation on the order of $\{-20\ [\mu m]\}$) on the outer diameter, but this is significantly easier to repeat compared to an angular interface, as well as being measurable. The quality of the graphite was also changed, since it was seen that the graphite from Wubben significantly degraded during the motor firings. Isostatic graphite was instead acquired with the aim of having lower degradation. This proved to be successful, meaning the assumption of a constant throat area (compared to a linearly increasing throat diameter assumed in Wubben's work) was valid.

The injector manifold design was also kept constant compared to Wubben's work (who attempted several different configurations). It was decided, based on a high success rate and ease-of-manufacturing (as well as the equipment available to the author) to use an injector manifold with a single main injector hole of diameter $\{2.3\ [mm]\}$ with two $\{0.5\ [mm]\}$ airbrush nozzles. Ultimately five such injector manifolds were usable during the test campaigns. One of the motor casings being produced can be seen in figure 3.1a, while one of the graphite rods used in the manufacturing process for the graphite nozzles can be found in figure 3.1b.

(a) One of the motor casings in the lathe.

(b) Graphite nozzle in the process of being machined.

Figure 3.1: Two of the components of the motor designed in a lathe.

While many components had to be manufactured, the test setup also had to be assembled. A Piping and Instrumentation Diagram (P&ID) can be seen in figure 3.2 which shows the proposed feedsystem, including valves (and their emergency states) as well as sensors. The real-world realisation can be seen in figure 3.3. From left to right, the red arrows indicate the motor, the main valve (MV), the emergency safety valve (ESV) and then the run-tank (under which the fill valve (FV) is located). On the right of the image, the N_2 and N_2O bottles can be seen.
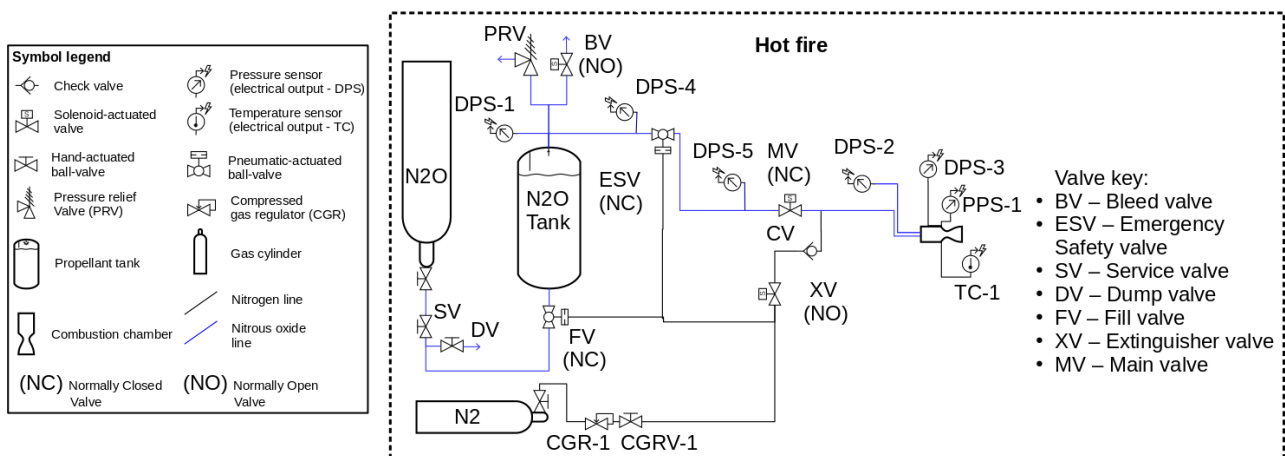
Figure 3.2: P&ID diagram for the feedsystem for the hotfire tests.
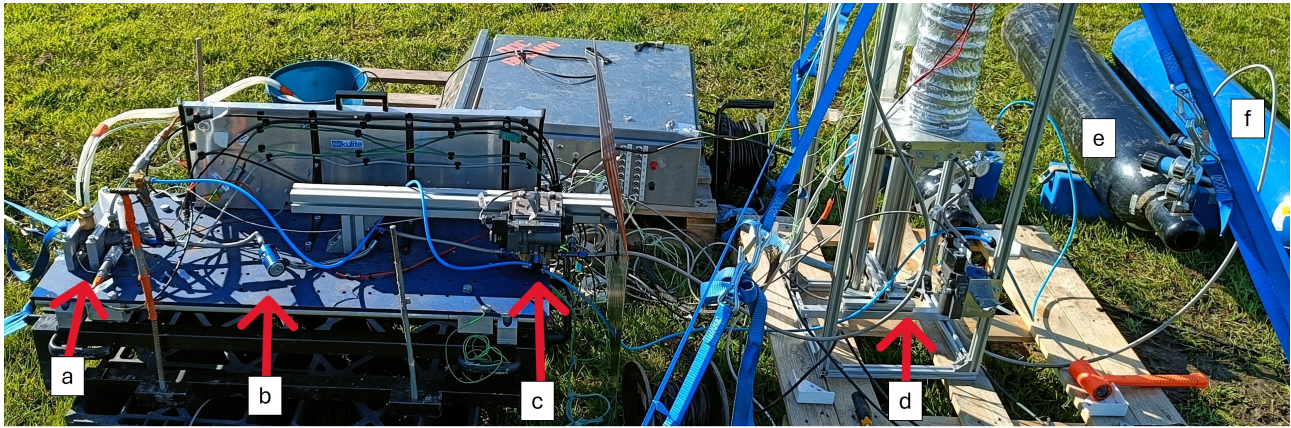
Figure 3.3: Feedsystem setup on the field. (a) the motor being tested; (b) MV; (c) ESV; (d) run-tank with FV; (e) N_2 bottle; (f) N_2O bottle.

3.1.2. Data collected and calibrations - test 1

For the first test campaign, the following information was gathered via the DAQ system:

- Temperature data (from K-type thermocouples) of the top and bottom of the run-tank. This was collected at {100 [Hz]}

- Pressure data of the run-tank, the pressure before the ESV, the pressure before the MV, injector manifold pressure and pressure inside the CC. These are all static pressure measurements. This was collected at {2500 [Hz]}

- Force measurements of the thrust produced by the motor, as well as the mass of the run-tank. This was collected at {50 [kHz]}

- Three piezoelectric sensors logged at {100 [kHz]}. This consists of a dynamic pressure sensor measuring combustion pressures, a microphone external to the motor, as well as vibration sensor attached on the outer body of the motor.

The following calibrations were used for each of the motor tests of the first test day. Table 3.1 consists of the static pressure sensor calibrations for the various locations in the feed system. Subsequently, table 3.2 shows the load cell calibration values, followed by the piezoelectric pressure sensor (also referred to as the PPS) in table 3.3. The temperature data, and piezoelectric vibration sensor and microphone do not have calibrations. The former is automatically converted within the DAQ system, and the latter pair are only used via a spectrogram analysis.

Table 3.1: Calibrations of static pressure sensors for the first test campaign for all grain configurations. Slope unit is [bar A^{-1}] while the offset has the unit of [bar].

Grain geometry	Static pressure sensors [bar]									
	Tank		Pre-ESV		Pre-MV		Injector		CC	
	Slope	Offset	Slope	Offset	Slope	Offset	Slope	Offset	Slope	Offset
Reference Double Anchor Cross Double Hole	6250	-24	6250	-24	6250	-24	6250	-24	6250	-24

3.1.3. Validity of data collected

Prior to analysis, the data collected should be checked whether it is usable. Based on the authors prior experience with the DAQ system and testing, data collection can occasionally go wrong, meaning the data collected is not usable. It can also stand to reason that the test itself causes sensor failure, which will mean that the data collected, while still usable, raises additional uncertainty errors - this analysis should then be taken with an additional grain of salt. The graphs from the first test can be found in appendix A.

In short, all sensors provided functional and usable data for analysis.

Table 3.2: Load cell calibrations for test campaign 1. Slope unit is [N V^{-1}] and [kg V^{-1}] for the thrust and tank mass, respectively. Offset is [N] and [kg], respectively.

	Load cells			
Grain geometry	Thrust [N]		Tank Mass [kg]	
	Slope	Offset	Slope	Offset
Reference		-39.61		-10.02
Double Anchor	-690639.975	-45.81	13409.27	-10.03
Cross		-44.92		-10.12
Double Hole		-47.23		-9.97

Table 3.3: PPS calibration for test campaign 1. Slope unit, per the datasheet (appendix F.3) is [mV MPa^{-1}].

	Dynamic PS	
Grain geometry	Slope	Offset
Reference		
Double Anchor		
Cross	2836	11.1
Double Hole		

Grain images before and after

While the data collected has been treated, images were also taken of the grains, before and after the test, in order to determine the accuracy of the regression analysis. These pictures also serve to determine whether defects were present prior to the test, and whether particular abnormalities were observed after the test was performed.

(a) Reference geometry before first test.

(b) Reference geometry after first test.

Figure 3.4: Before/after reference grain geometry.

Figure 3.4 shows the reference grain. The regression behaved as expected. Not shown are the two burn through holes present on either side of the ignition source for the grain.

Figure 3.5 shows the double anchor geometry. No burn throughs were detected on this grain, and the regression pattern still clearly shows (in figure 3.5b) the double anchor geometry present.

In figure 3.6, the cross geometry is shown. Also, no peculiar observations were made, and the cross geometry is also still present.

Lastly, figure 3.7 shows the double hole geometry. No peculiar observations were made, and the double hole geometry is still present.

3.1.4. Improvements for the second test campaign

Many lessons were learned during the first test campaign, both from a manufacturing perspective, as well as testing.

For manufacturing, the majority of the components made were functional. The two outliers were three of the injector manifolds (for the double anchor, cross and double hole geometries), as well as the graphite nozzle design.

(a) Double anchor geometry before first test.

(b) Double anchor geometry after first test.

Figure 3.5: Before/after double anchor grain geometry.
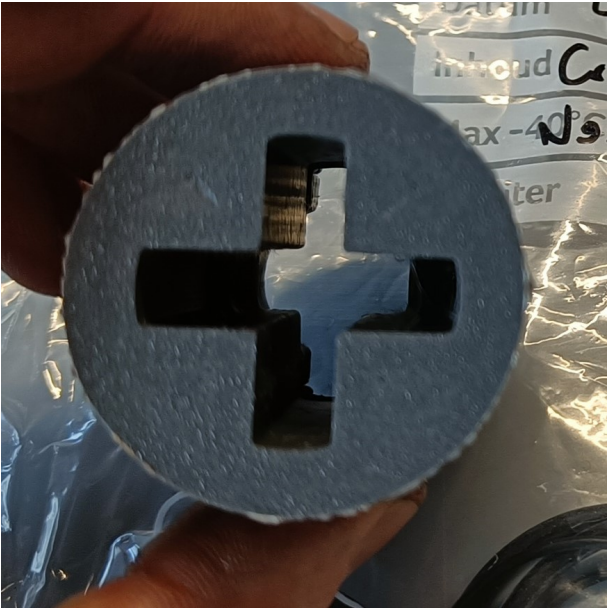
(a) Cross geometry before first test.

(b) Cross geometry after first test.

Figure 3.6: Before/after cross grain geometry.
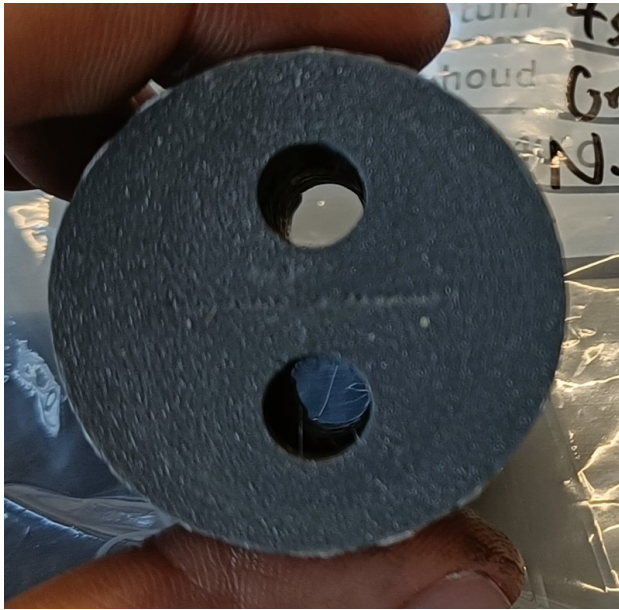
(a) Double hole geometry before first test.   **(b)** Double hole geometry after first test.

Figure 3.7: Before/after double hole grain geometry.

For the injector manifolds, it was discovered, after the first test campaign, that the main injector hole was smaller than designed. While the design diameter was {2.3 [mm]}, it was between {1.9 [mm]} and {2.0 [mm]}. This makes the comparison between the various geometries not entirely consistent, and the main injector hole was increased accordingly for the second campaign.

The graphite nozzle was also an issue during the first test campaign. As showcased in figures 4.5, 4.6 and 4.8, the divergent section of the nozzle (shown on the left of figure 3.8b) broke off at various points during the motor test (this is also later reflected in the thrust data). A nominal nozzle is shown in figure 3.8a. For future tests, the exterior geometry of the nozzle was changed as this design (with the associated support surface inside the steel retainer) was not suitable for its application.

(a) Nominal version 1 of the graphite nozzle.   **(b)** Forensics image of a graphite nozzle with the divergent section broken off during a motor test during the first test.

Figure 3.8: Example before and after first version graphite nozzle.

From a testing perspective, the majority of sensors were deemed sufficient. However, a core part of the analysis for this thesis revolves around determining the oxidiser mass flow. In doing so, several assumptions had to be made, the most important of which being the discharge coefficient of the injector and oxidiser density. In order to tackle the problem, it was determined that adding a thermal probe as close as possible to the injector manifold (with the thermal probe being exposed to the oxidiser flow) removing some of the uncertainty for the analysis - specifically in determining the density of the oxidiser. This was added to the testing setup for the second test

campaign[1]. The discharge coefficient was not further treated, and an assumption remains on its value.

The second improvement from a testing perspective revolves around the run-tank pressure. Since N_2O is a self-pressurising fluid, the tank pressure is not directly regulated. Instead, the temperature of the N_2O dictates its pressure. The pressure can be indirectly regulated by bleeding part of the pressure from the run-tank (however, this naturally comes with a certain error margin). In the first test campaign, this was not focussed on, resulting in a run-tank pressure ranging from {46.8 [bar]} for the reference and double hole geometry, {48.6 [bar]} for the double anchor geometry, and {50.9 [bar]} for the cross geometry. This will influence the pressure and thrust of the individual motors. This will be better regulated for the second campaign (however, the run-tank pressure fluctuation still allows a "proof-of-concept" to be shown). The different tank pressures for the first test can be found in figure A.1.

The last change made for testing was a slight change to the feedsystem. In the first test, the same valve used by Wubben was incorporated into the feedsystem. However, the pressure drop from the run-tank to the motor was deemed pretty significant. Therefore, in an effort to reduce this pressure drop (as well as removing as much of the influence on the behaviour of N_2O from the valve as possible), a valve with a greater orifice size was introduced. This was a duplicate of the ESV[2].

3.2. Campaign 2

The second test campaign had similar objectives to the first campaign, but with several modifications, namely:

- Collect data for both {4 [s]} and {8 [s]} burn times. This would serve to showcase whether the grain geometries are consistent with each other, as well as providing a second temporal data point for e.g. regression rate analysis.
- Better run-tank regulation to allow better data comparison inter-grain geometries.
- Investigate whether the added sensors (thermal probe before the injector) reduces the assumptions needed.
- Investigate whether the second version of the graphite nozzle does not blow out.

3.2.1. Manufacturing

Many components were already present, therefore a focus is drawn on manufacturing the graphite nozzles. The second version (in figure 3.9c) had several improvements over the first version (figure 3.9a). The difference that affected this thesis the most was a reduction in the high-tolerance dimensions. This was not required for the second version since the nozzle did not require a steel retainer ring (figure 3.9b). The high-tolerance was required for the first version, since hot gases should not permeate around the graphite. The second iteration integrates this retainer into the graphite itself. The original design was taken with inspiration from Wubben's work, in order to minimise the potential sources of discrepancy, while making it more manufacturable (as already mentioned, Wubben's nozzle design required a very precise, angular tolerance which is difficult to manufacture and measure after production to verify its dimensions). A technical drawing for the second version of the graphite nozzle can be found in appendix G.2.

3.2.2. Data collected and calibrations - test 2

Similar to the first campaign, the data collected is reviewed to determine validity, and whether particular data should be removed from the analysis. The data collected was the same (including logging rates) as the first test, except for an addition of a thermal probe as discussed in section 3.1.4. For this test, there were complications during testing in each of the different grain geometries.

Reference grain: For the reference grain, the grain did not end up igniting, but instead resulted in a cold flow. Based on camera footage, as well as combining the pressure of the injector manifold and temperature from the thermal probe, the motor initially received liquid N_2O, followed by gaseous N_2O. Figures 3.10a and 3.10b show the transition from liquid to gaseous N_2O flow, with figure 3.10c showing the density over time. Initially, the density is clear to be liquid since the density exceeds {800 $\left[\text{kg m}^{-3}\right]$}, which then drops by a factor of eight. After this spike, the density drops significantly less over time and is fairly constant. The tank pressure for the test started at {46 [bar]}. It is inconclusive to the extent liquid N_2O affects ignition - no cold flows occurred during the first test with all motors successfully igniting, meaning no visual clue is present regarding the phase

---

[1]It should also be noted that acquiring a mass flow meter was theoretically a possibility, however time limitations, as well as budgetary constraints made this infeasible for this work.

[2]Approximately, prior to this change, there was a pressure drop between the ESV and the MV of {1 [bar]}, while the pressure drop from the MV to the injector manifold was approximately {4.5 [bar]}. This change should therefore reduce the total pressure drop from the tank to the injector from {7.5 [bar]} to {4 [bar]} - with everything else being equal.

(a) Section view of first version of the graphite nozzle. The red line indicates the location of the break observed during the first tests.

(b) Steel retainer.

(c) Section view of second version of the graphite nozzle.
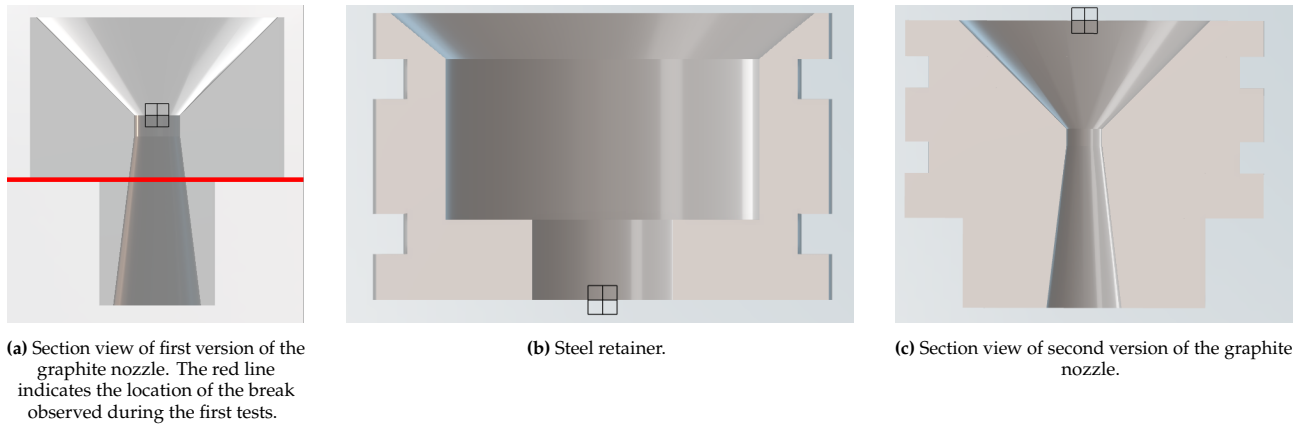
Figure 3.9: Design iteration of graphite nozzle.

state of the oxidiser, and the thermal probe was not present which gives insight into test days two and three, leaving this an open question.

(a) Liquid N_2O phase cold flow.

(b) Gaseous N_2O phase cold flow.

(c) Density of N_2O over time during the cold flow of the reference grain geometry.
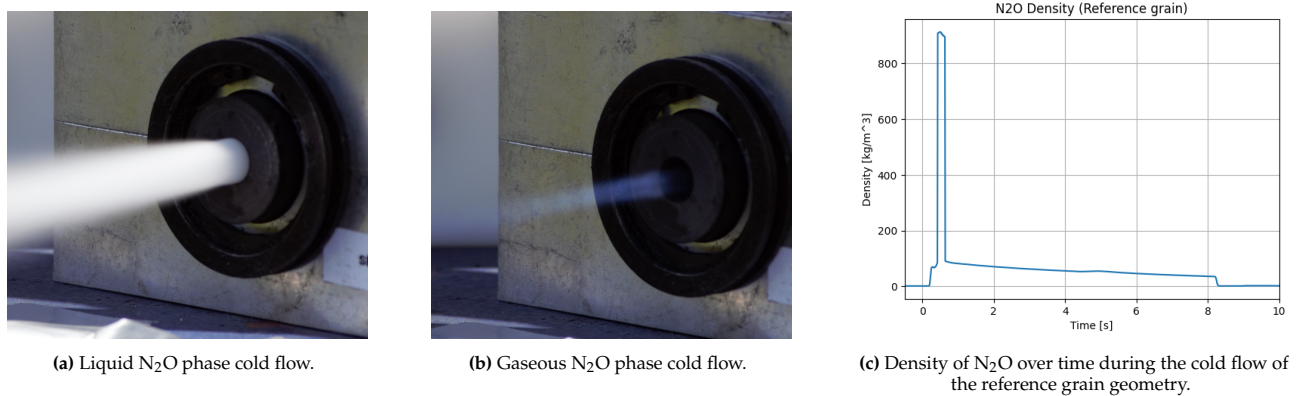
Figure 3.10: Visual and numeric data for reference grain geometry during test 2.

Double anchor grain: For the double anchor geometry, the grain was successful in ignition, however the flame at the start appeared very unstable - it was vibrating forwards and backwards. This indicates that the pressure in the CC and the injector manifold are close to each other. This is reaffirmed in the pressure sensor data, shown in figure 3.11c. The tank pressure for the test started at {44.25 [bar]}.

Cross grain: For the cross geometry, the grain also ignited, however a delayed ignition occurred. The combustion was also unstable[3] (similar to the double anchor geometry, see figure 3.12). Additionally, an automatic abort of the firing sequence occurred. Upon investigation, a single, incorrect signal was sent to the DAQ system, resulting in a test abort. The tank pressure for the test started at {45 [bar]}.

Double hole grain: The double hole grain also had similar issues. Also with a similar delayed ignition, a significant noise exceeding nominal expectations was made at start-up. It was clear from the pressure sensor readings that followed, a detonation event occurred within the motor assembly (as seen by the spike in data to above {70 [bar]} in figure 3.13c). This was also reflected in the thermal probe readings, with an elevated temperature of the N_2O, rather than a decrease (shown in figure 3.13a). Upon disassembly, the injector manifold was also deformed (figure 3.13b). The tank pressure for the test was at {46.5 [bar]}.

In terms of calibrations these were similar for the first test. The PPS calibration remains the same as found in table 3.3. Table 3.4 showcases the pressure sensor calibrations, while table 3.5 showcases the load cell values. It should be noted that the offset calibration for the tank mass load cell is the same for all grain configurations. This is intentional. Ultimately, the start and end value of the tank mass load cell are less important; the difference between the start and end value measured during the test provides the relevant information. This is different

---

[3]It should also be noted that in the data the CC pressure sensor *exceeds*, amongst others, the tank pressure. It was realised, after the test that the pressure sensor was damaged in the double anchor test, meaning the sensor was shifted in its ambient reading by {2.5 [bar]}. This has not been adjusted in the plot in figure 3.12.

(a) Longer flame for double anchor geometry.

(b) Shorter flame for double anchor geometry.

(c) Pressure data in first couple of seconds of the double anchor geometry showing unstable combustion.
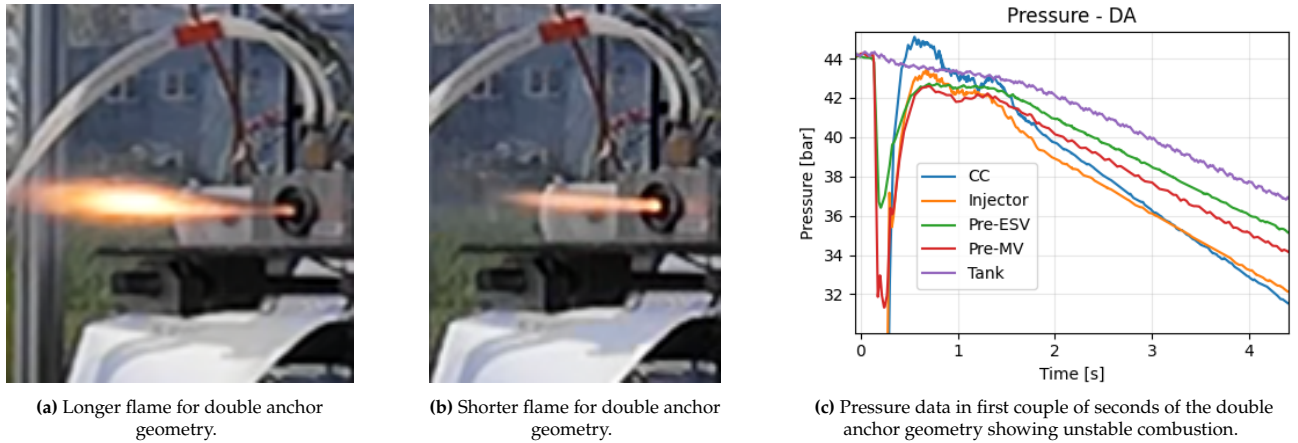
Figure 3.11: Visual and numeric data for double anchor grain geometry during test 2.

(a) Longer flame for cross geometry.

(b) Shorter flame for cross geometry.

(c) Pressure data are all practically identical in terms of value in first seconds of the cross geometry - this shows unstable combustion.
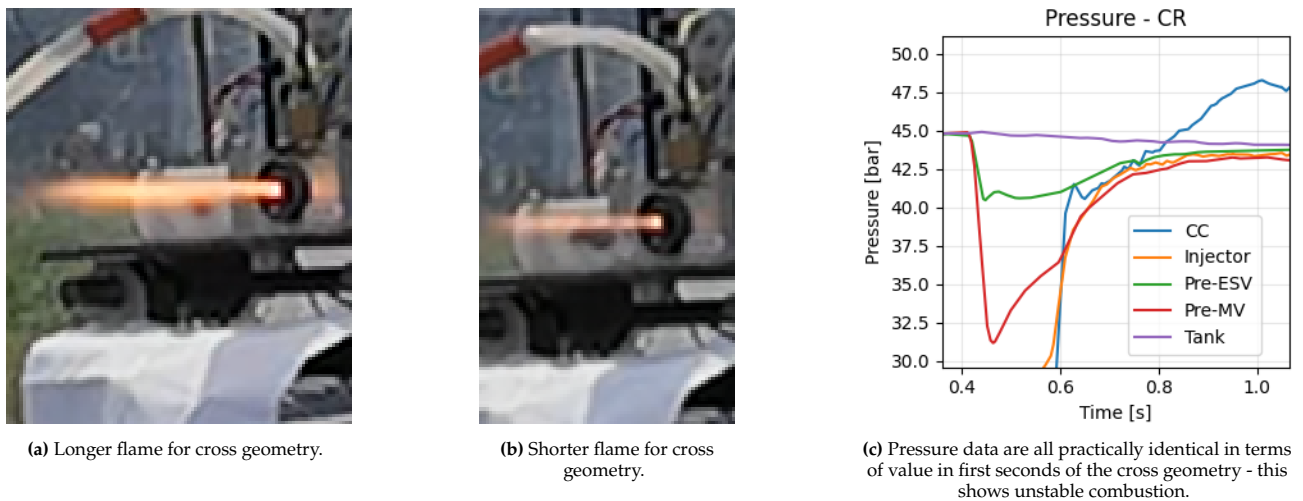
Figure 3.12: Visual and numeric data for cross grain geometry during test 2.

(a) Thermal probe data for double hole geometry.

(b) Broken injector manifold for double hole geometry; (a) lower o-ring groove plastically deformed.

(c) Pressure data for double hole geometry showing unstable combustion.

Figure 3.13: Visual and numeric data for double hole grain geometry during test 2; visual plastic deformation on injector manifold o-ring groove.

compared to the thrust measurement, where the starting value should be zero. Therefore, an identical offset was applied for these sensor measurements.

Table 3.4: Calibrations of static pressure sensors for the second test campaign for all grain configurations. Slope unit is [bar A^{-1}] while the offset has the unit of [bar].

Grain geometry	Static pressure sensors [bar]									
	Tank pressure		Pre-ESV		Pre-MV		Injector		CC	
	Slope	Offset	Slope	Offset	Slope	Offset	Slope	Offset	Slope	Offset
Reference Double Anchor Cross Double Hole	6250	-24	6250	-24	6250	-24	3750	-14	6250	-24

Table 3.5: Load cell calibrations for test campaign 2. Slope unit is [N V^{-1}] and [kg V^{-1}] for the thrust and tank mass, respectively. Offset is [N] and [kg], respectively.
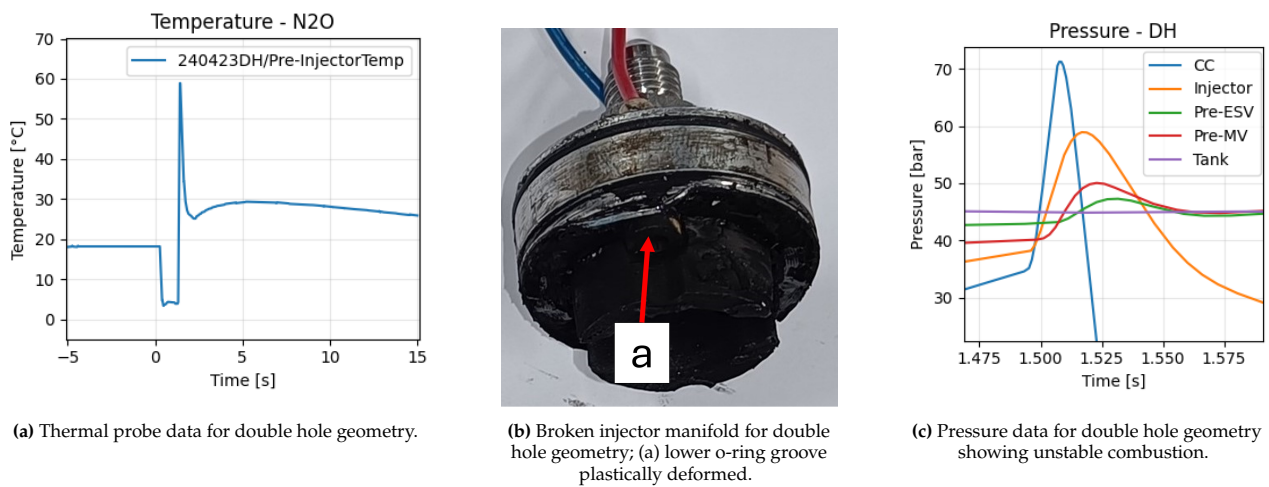
Grain geometry	Load cells			
	Thrust [N]		Tank Mass [kg]	
	Slope	Offset	Slope	Offset
Reference		-50.00		
Double Anchor		-51.00		
Cross	-690639.975	-52.00	13409.27	-10.00
Double Hole		-52.00		

3.2.3. Validity of data collected - test 2

Based on the description of the test events, it is certain that several data points are either unusable, or questionable in their validity. The sensor data itself can be found in appendix B, however a summary is provided here:

- For the reference grain geometry, all sensors performed as expected, and there is little doubt about the validity of the measurements. It is, however, important to note that this test was a cold flow, meaning that the combustion performance is not available. The thermal data from the thermal probe, indicating the temperature of the N$_2$O before the injector, does provide a lower limit regarding oxidiser temperature for this series of tests.

- For the double anchor geometry, the pressure readings from the CC sensor is questionable. This is based on the fact that it did not return to reading an ambient pressure. This behaviour, based on experience, occurs when a pressure sensor experiences a significant temperature and the internal membrane being permanently deformed. This sensor is attached to a standoff tube filled with grease, however this was not reapplied between the two test days. It is reasonable that this caused the sensor to be exposed to greater temperatures than permitted. The remaining sensors have no indication of malfunction.

- For the cross geometry, the first issue arises from the CC sensor. This was not yet replaced from the double anchor test, therefore an offset is present in the measurements. This sensor does return to the same offset after the test, so the pressure data could be applied with a manual offset. However, due to the automatic abort, the test data itself does not paint a significant picture to do a comparative analysis.

- For the double hole geometry, the CC pressure sensor (which was replaced after the cross geometry test) is non-functional after the detonation event. It was with this test that a part of the graphite nozzle also broke off the body (see figure 3.14). This test was manually aborted by DARE's SO.

Grain images after test 2

Similar to the first test, figure 3.15 shows images that were taken of the grains after the test (the images before were not taken since, upon visual inspection, these grains did not showcase any fault. Therefore, the before images from the first campaign can be taken as reference).

Figure 3.15a is an image of the pre-chamber for the reference grain from the second test. It was suspected that the failed ignition arose from the ignition source (indicated by the red arrows) was not functioning properly. Visual inspection did not indicate whether this was ultimately the case.

Figure 3.14: Broken graphite nozzle from double hole test 2.

Figure 3.15b shows the side of the grain, and a significant amount of ABS has been used during the motor burn (especially compared to figure 3.5b). The distinct shape is no longer present as a result of the increased burn time of {8 [s]}. No other abnormalities were found.

Figure 3.15c shows the slight degradation of the fuel prior to the aborting of the test. Otherwise, a successful ignition.

Lastly, figure 3.15d, on the right shows the top of the grain prior to the manual abort of the test. The red arrows on the left of the image, point towards the plastically-deformed groove present in the injector manifold from the detonation event.

3.2.4. Improvements for last test opportunity

Based on inspection of the data and images collected, three significant changes were made for the last test attempt. The first change was the reverting back to using the same valve setup as Wubben 2022 [1]. The pressure drop in the second test were lower compared to the first test, but there was not enough testing time to conclusively evaluate the effect of the lower pressure drop over the system; in other words, it is inconclusive whether the lower pressure drop was (in part) the cause for the second set of tests being unsuccessful compared to the first tests, or whether other factors also contributed (such as manufacturing defects or even weather playing a role). Therefore, this change was made, combined with the second change of testing for only {4 [s]} instead of another campaign of {8 [s]}. Lastly, figure 3.10c shows that liquid N_2O originates in the system. For this thesis, it was assumed that only gaseous N_2O was present in the system. This assumption was made as the filling procedures were followed that promoted only the gaseous phase of the oxidiser entering the run-tank, as well as there not being enough mass present in order for the N_2O to reach its saturation curve (thereby having two phases in the run-tank). This assumption seems questionable at best. This dictates the third change - for the previous two tests, the oxidiser was taken out of the bottom of the run-tank. For the third test, the oxidiser is extracted from the top. In figure 3.16, the red arrow at the bottom of the image shows the old location, while the top (blue arrow) shows the new location for extraction of the oxidiser into the motor.

3.2.5. Data collected and calibrations - test 3

For the last test, likewise with the other two, the data collected and its calibrations are assessed. For this test, there were three successful hotfires with one cold flow (with the cold flow being the reference grain geometry). The calibrations used for the test can be found in tables 3.6 and 3.7 for the pressure sensors and load cells, respectively. Like with the previous tests, the PPS sensor calibration can be found in table 3.3.

(a) Reference geometry after second test. Red arrows point to the ignition source which could be the cause for the cold flow instead of successful ignition.

(b) Double anchor geometry after second test.

(c) Cross geometry after second test.

(d) Double hole geometry after second test.

Figure 3.15: After pictures for all geometries after the second test (23 April 2024).

Table 3.6: Calibrations of static pressure sensors for the third test campaign for all grain configurations. Slope unit is [bar A^{-1}] while the offset has the unit of [bar].

Grain geometry	Static pressure sensors [bar]									
	Tank pressure		Pre-ESV		Pre-MV		Injector		CC	
	Slope	Offset	Slope	Offset	Slope	Offset	Slope	Offset	Slope	Offset
Reference Double Anchor Cross Double Hole	6250	-24	6250	-24	6250	-24	3750	-14	6250	-24

Figure 3.16: Image of the run-tank. The red arrow (bottom, labelled (a)) indicates the extraction from the bottom of the tank, the blue arrow (top, labelled (b)) shows the new location for the third test.

Table 3.7: Load cell calibrations for test campaign 3. Slope unit is $[\text{N V}^{-1}]$ and $[\text{kg V}^{-1}]$ for the thrust and tank mass, respectively. Offset is [N] and [kg], respectively.

	Load cells			
Grain geometry	Thrust [N]		Tank Mass [kg]	
	Slope	Offset	Slope	Offset
Reference		-45.21		
Double Anchor		-44.17		
Cross	-690639.975	-42.57	13409.27	-10.00
Double Hole		-39.58		

3.2.6. Validity of data collected - test 3

As with the other two sets of data, the data collected during the third test is evaluated. The sensor data itself can be found in appendix C, however a summary is provided below:

- For the reference grain geometry, all sensors seem to provide reasonable values, with the exception of the PPS sensor (figure C.6a).

- For the double anchor geometry, all sensors provide reasonable values, but likewise with the reference geometry, the PPS sensor (figure C.6b) seems to not showcase what is expected (especially compared to previous tests). The vibration sensor in figure C.8 is also more irregular than previous tests.

- For the cross geometry, a similar story follows with the sensors (and the lack of usable data from the PPS sensor). The PPS sensor in figure C.6c seems to not be reacting except for ignition. This is reaffirmed that the shapes observed in figure A.5 are not present at all. Most likely the sensor is damaged.

- Lastly, for the double hole geometry, the pressure data from the injector and CC are not usable, as well as the PPS sensor. The thermal probe (see figure C.5) shows an increase in temperature, meaning a detonation-like event took place which caused the oxidiser to increase in temperature rather than decrease during the test.

Grain images after test 3

The grains were also pictured after the third test and can be seen in figure 3.17. It can be observed that the grains that were fired (all except the reference grain) look very similar to figures 3.5b, 3.6b and 3.7b. Visually, this indicates that the combustion of the grains were similar and that the regression behaviour should be comparable. It can then be reasonable to assume that the reference geometry would have also acted similarly, and that some of the data collected from the double anchor and cross geometry (namely the thermal probe measuring the N_2O temperature) could be applied to the data collected from the various geometries in the first test and analysed.

3.3. Conclusion

In conclusion, this chapter addresses the manufacturing and testing process used during this thesis - a foundation already existed, but in furthering the investigation, improvements were able to be made, such as removing many of the machining tolerances that make the experiment difficult to reproduce (either monetarily or time-wise). There were challenges which required a redesign of particular components, and not all data collected ended up being usable for further analysis. It can therefore be said that attention should always be paid to the setup and sensors that are used, but also how to properly set up the DAQ system - this is even more evident for sensors that can experience elevated temperatures, and the proper countermeasures should be taken to mitigate the risk that a sensor stops operating as expected. However, the motor tests that were successful can be analysed with the data collected.

The data was assessed for its suitability, and calibrations of all the sensors were provided (in case in the future the data is to be re-processed for a different study).

Lastly, the various improvements between tests was also gathered, and implemented in order to gather more relevant information which would otherwise have to be modelled or assumed (which by itself would introduce inaccuracies).

(a) Reference geometry after third test.

(b) Double anchor geometry after third test.

(c) Cross geometry after third test.

(d) Double hole geometry after third test.

Figure 3.17: After pictures for all geometries after the third test (7 May 2024).

This page was intentionally left blank

Initial test campaign

This chapter contains the data and analysis for the first set of tests. This data will be used to assess whether the changes made (when compared to the reference design), as a "proof-of-concept", achieve the goals that were set out (as well as showcase where improvements could be made). It was assessed in section 3.1.3 that all sensors reported reasonable data, and this data can be used to analyse the performance of the different motor designs.

4.1. Simulation results

Prior to analysing the data, the simulation results are checked. This shows what to expect from the data (and then ultimately if assumptions made in the model lead to inaccuracies). All simulations follow a tank pressure showcased in table 2.1. This starts at {44 [bar]} and decreases to {34 [bar]} after {4 [s]}.

4.1.1. Thrust

The first simulation result is the thrust, shown in figure 4.1. The thrust profiles are fairly similar. The start values are all around {60 [N]} and all finish around {45 [N]}.
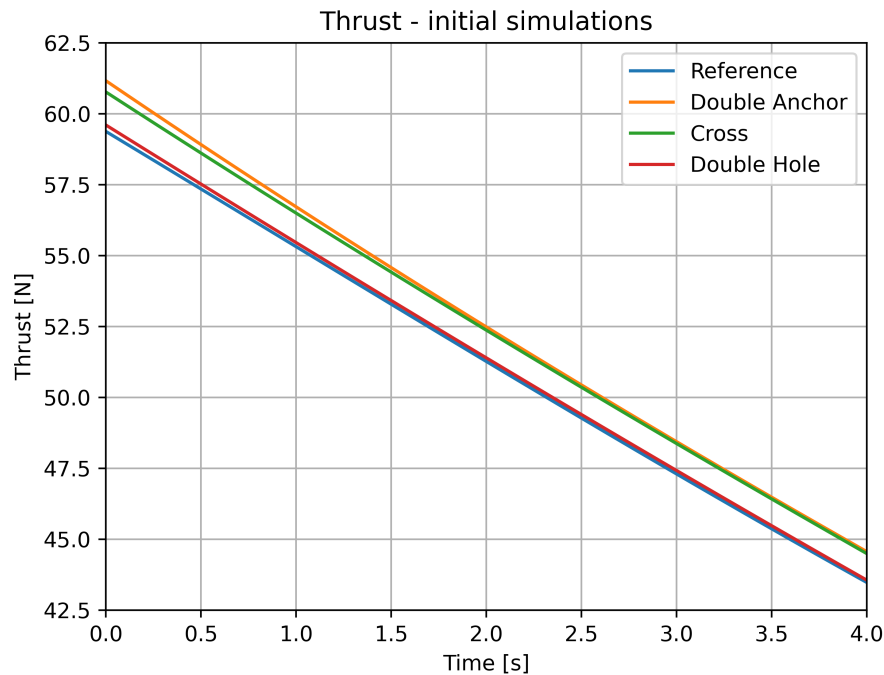

Figure 4.1: Thrust results from the hybrids ballistic model. All geometries operate in a similar regime and seem to have a similar drop-off over the course of the burn time.

4.1.2. Combustion chamber pressure

Concerning the CC pressure, a similar trend as with the thrust estimations can be seen in figure 4.2. The start values are all around {32 [bar]} and decrease to slightly above {24 [bar]}.
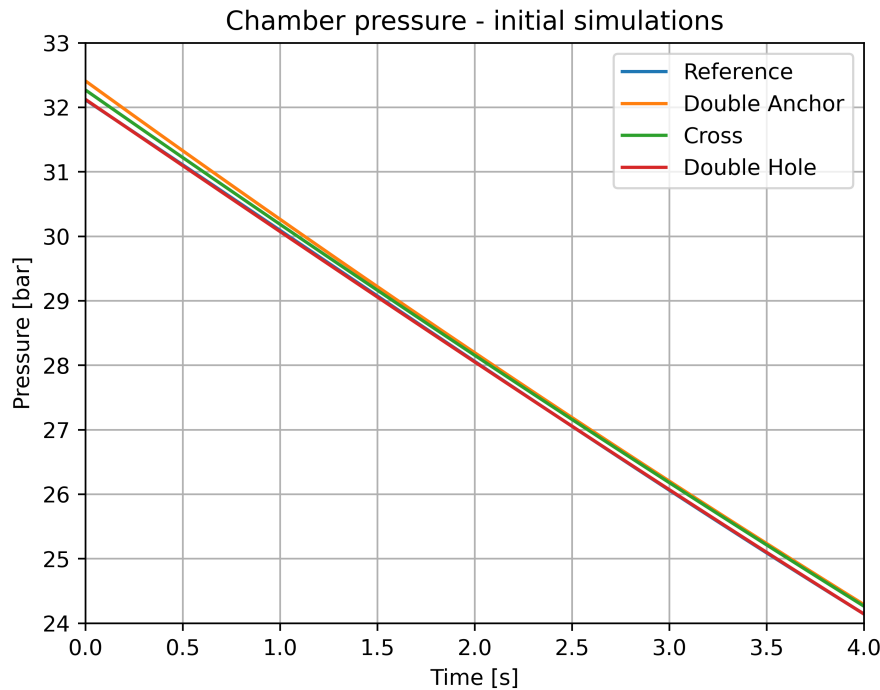

Figure 4.2: CC pressure results from the hybrids ballistic model. All geometries operate in a similar regime (where the reference and double hole geometry are practically identical) and seem to have a similar drop-off over the course of the burn time.

4.1.3. O/F ratio

Lastly, the O/F ratio over time does showcase more differences (see figure 4.3). The first to note is that the reference grain showcases the highest O/F ratio while the double hole geometry has a slightly lower O/F ratio - hovering around a ratio of {5 [−]} - with a slight increase to {5.2 [−]}. The cross geometry is the next geometry with a lower ratio, remaining close to constant at a value of {3 [−]}. Lastly, the double anchor geometry starts with the lowest, and also showcases a greater shift from approximately {2.6 [−]} and peaking at {2.9 [−]} before slightly decreasing again when compared to the cross geometry.

Especially on this front, the simulation shows that the initial proposal in altering and flattening the O/F ratio can be achieved.

4.2. Test results

Table 4.1 showcases the first collection of quantitative data for the first test. The grains and nozzles were measured before and after the test. This campaign also included measuring the dimensions of the grains prior to the campaign to see the difference between the intended design and what the grain ended up being after being printed. All grains are similar in dimensions. It should be noted that the first reference grain attempt was a misfire. The grain itself was not reused, while the nozzle was reused.

Another observation from this is that the assumption concerning the degrading nozzle throat seems to be valid. Most nozzles cracked during the test (as can be seen in figures 4.5b, 4.6b and 4.8b), while the cross geometry nozzle did not. But even with this single "true" data point, the nozzle degradation was {0.07 [g]} - it will be taken therefore for the next campaigns that the nozzle does not degrade significantly to have an effect on performance.

Table 4.2 shows the parameters which are collected and calculated from the tests that were performed. The misfire has not been included in this table. The first observation concerns the thrust - visualised in figure 4.13a, the maximum thrust does differ among the grains. This can however be partially explained by the big variance in the start tank pressure. The highest thrust, produced by the cross geometry at {70 [N]} also had the highest tank pressure at {50.9 [bar]}. The two geometries that had an identical tank pressure were the reference and
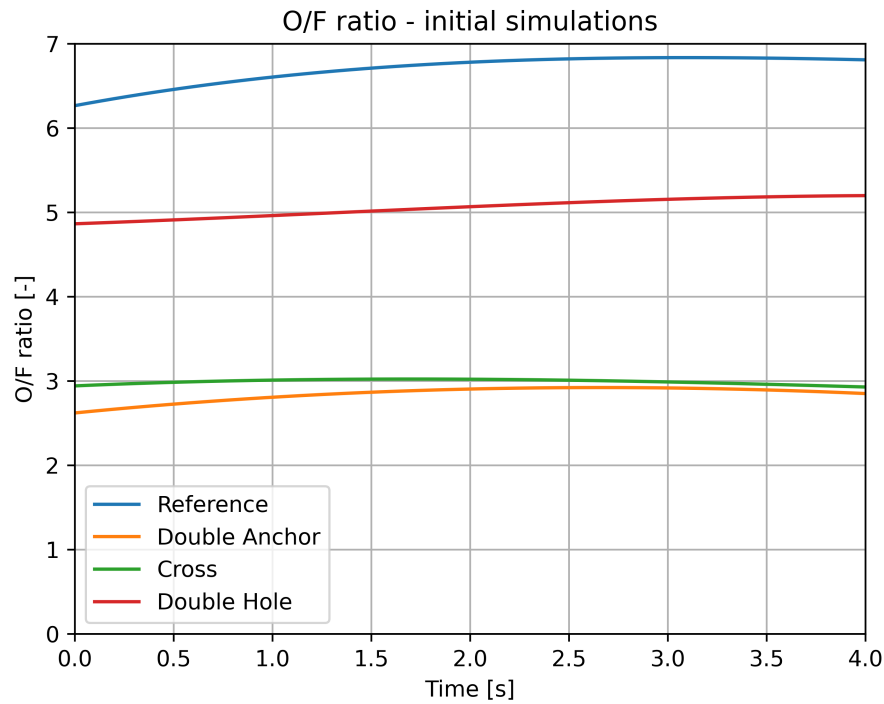
Figure 4.3: O/F ratio results from the hybrids ballistic model. The double anchor and cross geometries exhibit a similar behaviour and are noticeably flatter when compared to the reference geometry. The double hole geometry has a slightly increasing ratio, while the reference geometry has the highest ratio from the available geometries.

Table 4.1: Measured parameters from the various motors tested during the first test campaign ({4 [s]} burn time. The orange cell indicates a misfire, while the yellow cell indicates that the nozzle broke during disassembly (but remained whole during the test). The red cells indicate that the nozzle broke during the motor test. RF: Reference, CR: Cross, DH: Double hole, DA: Double anchor.

Test	Grain mass [g]	Nozzle mass [g]	Before test Outer diameter [mm]	Inner diameter [mm]	Height [mm]	After test Grain mass [g]	Nozzle mass [g]	Notes
RF 4.1	59.52	12.87	39.12	11.50	59.60	N/A	N/A	Misfired, nozzle reused
RF 4.2	59.25	12.87	39.30	11.63	59.60	50.70	12.83	Two burn throughs present on pre-chamber end. Used same nozzle as Reference 4.1, Divergent section broke during firing
CR 4.1	49.13	12.89	39.22	27.20 x 6.82	59.66	35.41	12.82	Divergent section of the nozzle broke during disassembly
DH 4.1	58.78	12.90	39.20	8.18 x 2	59.50	40.79	12.89	Divergent section broke during firing
DA 4.1	53.19	12.91	39.24	24.70	59.60	38.98	12.73	Divergent section broke during firing

double hole geometries - their maximum thrust did differ, where the double hole geometry was higher. This can be explained by the greater (fuel) mass flow due to a greater burning surface area - even though the regression rate should be the same since the port area was identical between the reference grain and the double hole geometry.

Another observation concerns the fuel mass flow. The reference grain exhibited the lowest fuel mass flow. Due to the increased burning area, the cross and double anchor geometry exhibited a higher fuel mass flow, with the double hole geometry having the greatest fuel mass flow.

Oxidiser mass flow

The amount of N_2O used during the test is necessary in order to determine the O/F ratio. Two methods were explored for the first test campaign to calculate this since a mass flow meter for N_2O (with the relevant mass flow rate capacity) was not available.

Tank load cell: The first approach (which was also employed by Wubben) involves a direct measurement of the run-tank. The data collected can be seen in figure 4.4. In this figure several excitations can be seen. Every grain geometry will have two, one corresponding to when the MV opens, and the second corresponding to the same valve closing. For all geometries except the cross geometry, a third excitation is visible (and labelled in the figure). These correspond to the graphite nozzles breaking.

Ultimately, this method proved to be inconsistent and unreliable. In using Wubben's method, a time-average of several seconds before the motor test, followed by a time-average of the load cell after the motor test, a linear mass flow can be calculated by subtracting the end mass from the start mass and dividing by the test duration. However, as seen in table 4.2 (the column labelled with "M1"), the oxidiser mass flow exhibits great variety. Based on literature, the expected oxidiser mass flow (as also used in the simulations) was around $\{20 \left[\mathrm{g\,s^{-1}}\right]\}$. The cross geometry overestimates the mass flow, while the double anchor gets in the correct ballpark. The other two geometries underestimate the mass flow by a factor of two to four. Therefore, a different method will be attempted.

Isentropic relations: Like in the simulation, the isentropic relation (equation (2.7)) can be used since the start and end pressure of the run-tank is known, and the start density is also known. By calculating the density of the oxidiser at all time during the test, the mass of the oxidiser can be found since the volume of the run-tank ($\{3.14 \text{ [L]}\}$) is known. Indirectly a mass flow can therefore be determined. The time-average mass flow can be found in the column labelled "M2".

These values seem more reasonable and are in the same order-of-magnitude as expected. It should also be noted that the specific impulse is also comparable to those attained by Wubben 2022 [1, table 7.1].

Ultimately, for the next test campaign, a thermal probe was acquired which measured the temperature of the oxidiser before the injector manifold. This sensor, combined with the pressure reading from the injector manifold sensor and CoolProp [12] allows the density to be calculated and put directly into equation (2.1). The one downside is that a different discharge coefficient will be required. For the next tests, this value is taken to be $\{0.7 \, [-]\}$. This was taken from Wubben 2022 [1, fig. D.8].

Table 4.2: Calculated parameters from the various motors tested during the first test campaign ($\{4 \text{ [s]}\}$ burn time). RF: Reference, CR: Cross, DH: Double hole, DA: Double anchor.

Test	Maximum thrust	Maximum P_c	Start P_{tank}	Impulse	ABS used (avg. $\dot{m}_f$)	M1 N_2O used (avg. $\dot{m}_{\text{ox}}$)	M2 N_2O used (avg. $\dot{m}_{\text{ox}}$)	avg. O/F - M2	I_{sp}
Unit	[N]	[bar]	[bar]	[N s]	[g] ([g s^{-1}])	[g] ([g s^{-1}])	[g] ([g s^{-1}])	[−]	[s]
RF 4.2	56	36	46.8	178	8.55 (2.14)	35 (8.75)	77.5 (19.4)	9.1	210.9
CR 4.1	70	43	50.9	250	13.72 (3.43)	106 (26.5)	72.3 (18.1)	5.3	296.4
DH 4.1	58	38	46.8	185	17.99 (4.50)	23 (5.75)	67.8 (17.0)	3.8	219.9
DA 4.1	62	40	48.6	205	14.21 (3.55)	68 (17.0)	68.2 (17.0)	4.8	253.7

Fuel mass flow

While the average fuel mass flow can be taken by averaging the difference in mass of the fuel grain measured before and after the test, the model can also simulate the instantaneous fuel mass flow. This can be seen in figure 4.9a. The fuel mass flow is calculated by rearranging equation (2.2) to solve for the fuel mass flow (equation (4.1)). The time-averaged fuel mass flows can be found in the legend of figure 4.9a. The second method will assume a constant fuel mass flow, and use the time-averaged difference in mass from the fuel grain before and after the test, as mentioned previously. This is shown in figure 4.11a and table 4.2.
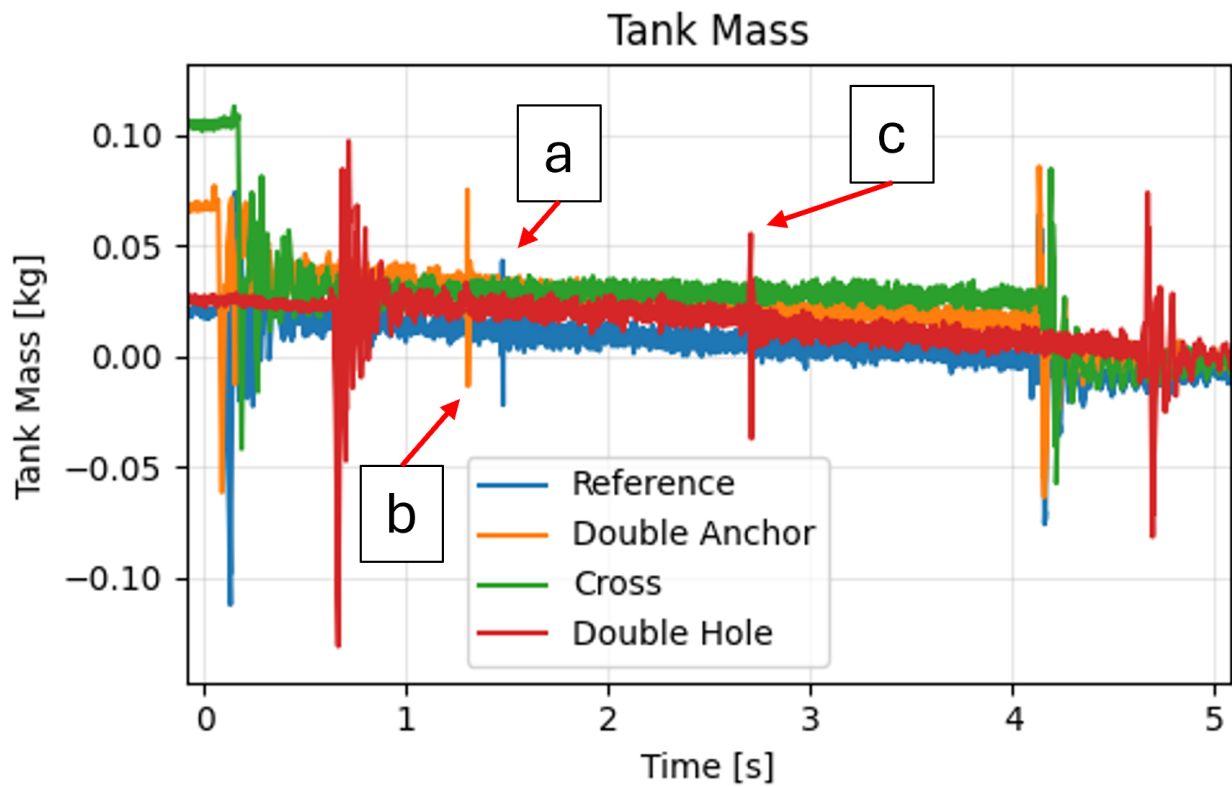
Figure 4.4: Tank mass readings from the load cell of the run-tank. (a) Nozzle breaking for reference geometry; (b) nozzle breaking for double anchor geometry; (c) nozzle breaking for double hole geometry.
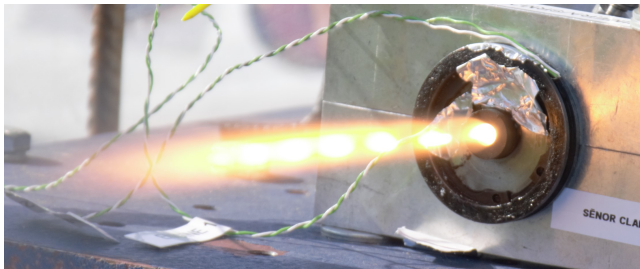
(a) Reference grain at start of engine test.

(b) Reference grain after nozzle broke.

Figure 4.5: Reference grain, 4s test (14 March 2024).

(a) Double anchor grain at start of engine test.

(b) Double anchor grain after nozzle broke.

Figure 4.6: Double anchor grain, 4s test (14 March 2024).

(a) Cross grain at start of engine test.

(b) Cross grain at end of engine test.

Figure 4.7: Cross grain, 4s test (14 March 2024).

(a) Double hole grain at start of engine test.
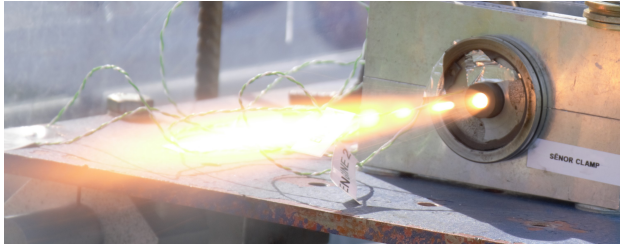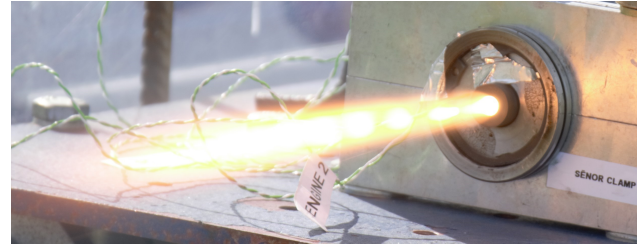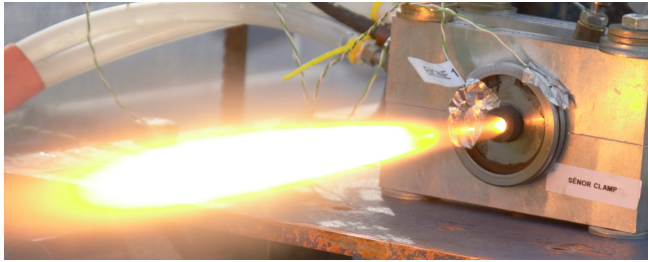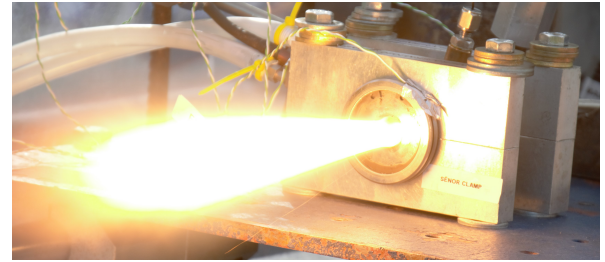

(b) Double hole grain after nozzle broke.

Figure 4.8: Double hole grain, 4s test (14 March 2024).

$$\dot{m}_\mathrm{f} = \frac{P_\mathrm{c} \cdot A_\mathrm{inj} \cdot \Gamma}{\sqrt{T_c \cdot R}} - \dot{m}_\mathrm{ox} \tag{4.1}$$

For the first fuel mass flow method, the values do differ compared to the measured values in table 4.2, but they do remain in a similar ballpark (with the greatest deviation of approximately $\{1.8 \left[\mathrm{g\,s^{-1}} \right]\}$ for the cross geometry). It is also seen in figure 4.9a that the fuel mass flow does decrease with the double anchor and cross geometries (which is one of the reasons these specific geometries were chosen).

The second method is considerably easier, and will provide greater stability since no fluctuating inputs are less likely (with the other method, it was possible that a timestep caused a e.g. very low fuel mass flow, which causes a very low combustion temperature, which subsequently affects the inputs for the next timestep). This is less likely with this second method. This will naturally have the downside of having to assume that the fuel mass flow is temporally constant. The O/F ratio is more constant, and higher than with method one (figure 4.11b).

For the first test campaign, it can be seen that some of the analytical methods produce reasonable results (for example, figure 4.9b is in the correct order-of-magnitude - ignoring the shapes of the curves due to how SciPy created the splines). Others are seemingly a bit more varied. The fuel mass flow in figure 4.9a varies more and has a drastic impact on the O/F ratio in figure 4.9c. To add to this fact, the Python module RocketCEA, which is used to calculate the current combustion temperature also fluctuates drastically, specifically for the reference grain. It is currently uncertain where this fluctuation comes from.

4.3. Inter-motor performance

The performance of the different motors should also be compared. In figure 4.13a, all thrust profiles are presented. The first clear observation results from the sudden decrease in thrust - each of these events for all geometries (except the cross geometry) result from the moment the divergent section of the nozzle broke. This caused a sudden drop in thrust (and then also a decrease in total impulse - which explains the higher impulse for the cross geometry - table 4.2). Another observation is that the thrust curves do not align - this is a DAQ issue insofar that data is written in batches, and the reference used to indicate 'T = 0' is written as a different data file compared to, among others, thrust data. This is manually adjusted for further processing.

The CC pressure can be identified in figure 4.13b. The pressure did not seem to be affected by the nozzles breaking. After the tests, the graphite nozzles were inspected and the break lines were near the throat (on the divergent side) - this means that the throat still behaved as expected for the CC pressure and chocking the flow. The difference in CC pressure performance can therefore be attributed to the different run-tank (starting)
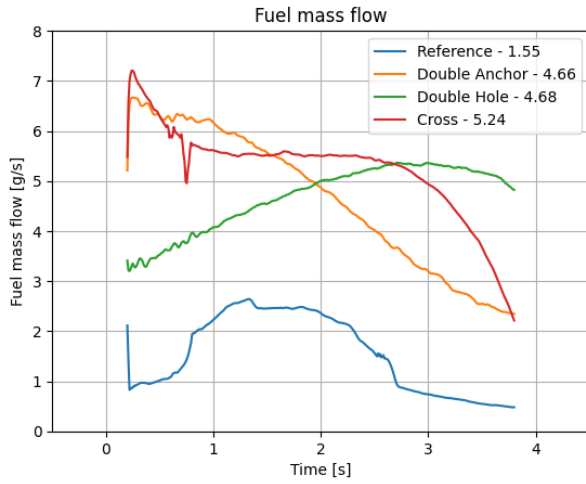
(a) Fuel mass flow (method 1) over time from first test campaign. The numbers in the legend refer to the average of the plotted lines shown.
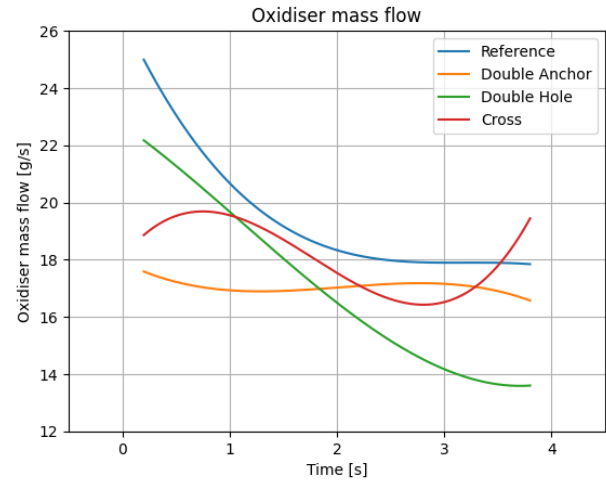
(b) Oxidiser mass flow (smoothened with a spline, using "M2") over time from first test campaign.
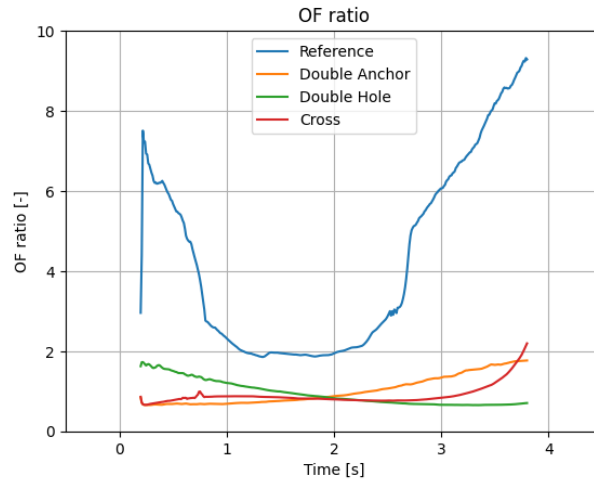
(c) O/F ratio of all different grains.

Figure 4.9: Propellant mass flow and associated O/F ratio over time from the first test using the first method to determine fuel mass flow.
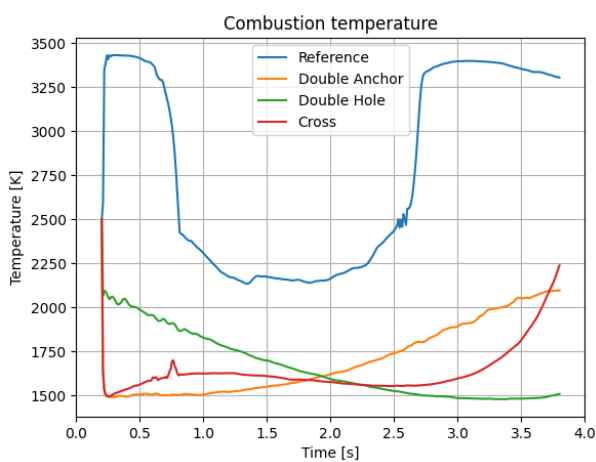
(a) Combustion temperature fluctuations per RocketCEA.
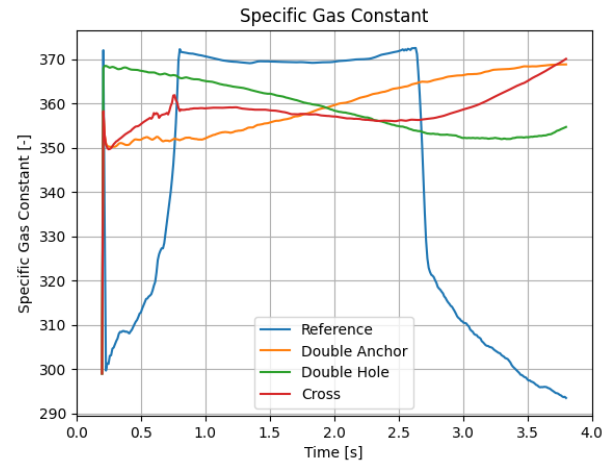
(b) Specific gas constant per RocketCEA.

Figure 4.10: Input parameters with large fluctuations from RocketCEA. These figures correspond to the instantaneous fuel mass flow method via equation (4.1).
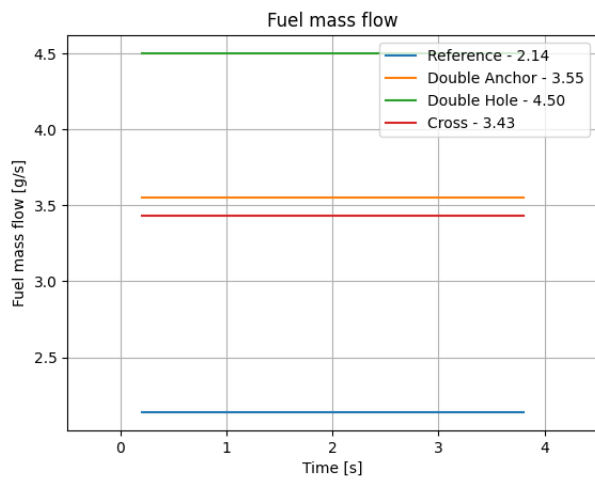
(a) Fuel mass flow (method 2) over time from first test campaign.
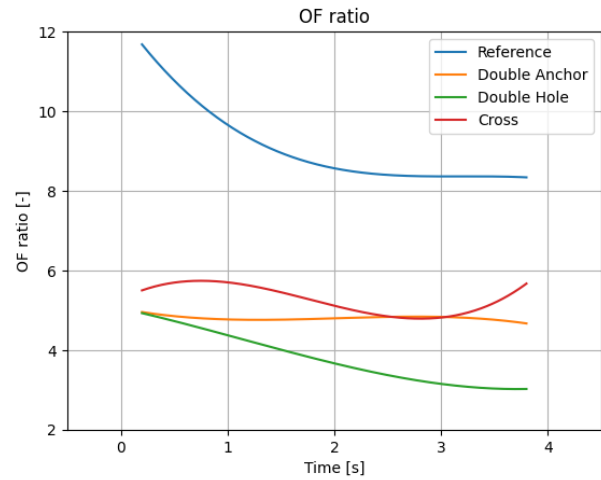
(b) O/F ratio of all different grains with method 2.

Figure 4.11: Propellant mass flow and associated O/F ratio over time from the first test using the second method to determine fuel mass flow.
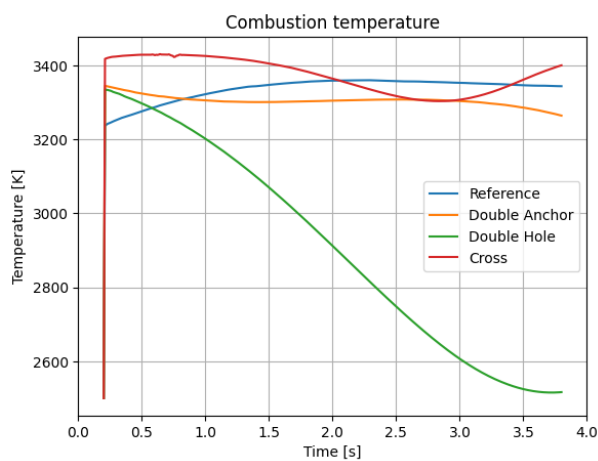
(a) Combustion temperature per RocketCEA (method 2).
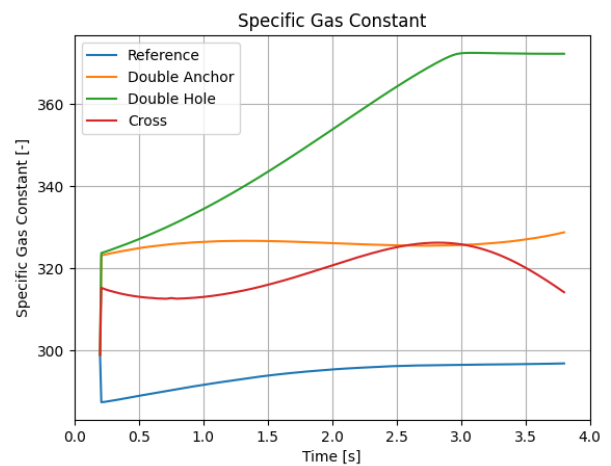
(b) Specific gas constant per RocketCEA (method 2).

Figure 4.12: Input parameters with smaller fluctuations from RocketCEA. These figures correspond to the time-averaged fuel mass flow, taken from the real-world measurements of the fuel grain masses before and after the motor test.

pressures, as well as the different geometries. A similar translation in the writing of data is present, as with the thrust data.

(a) Thrust performance of {4 [s]} grains on first test day.

(b) CC performance of {4 [s]} grains on first test day.

Figure 4.13: Thrust and CC pressure during the first test day.

In order to indicate how well each geometry performed compared to each other, the thrust coefficient can be used - see equation (4.2). This coefficient is a measure of how well the motor and nozzle produces thrust for every unit of CC pressure and throat area. For the first test, this is visualised in figure 4.14. A complete comparison is not possible to make due to the sudden drops in thrust due to the nozzle disintegration, however for the first second in time during the tests, the coefficients are all the same order of magnitude, with the cross geometry being the best at converting its combustion process into thrust for every unit of CC pressure. The double hole is seemingly the least efficient. It should also be noted that the curves are not compensated for the nozzles popping off. This was because the popping of the nozzle occurred close to the throat, so the throat diameter did not change (although the expansion ratio changes instantaneously from the throat diameter of {4 [mm]} to the outer diameter of the divergent section, set to {14 [mm]}.

$$C_F = T_h/(P_c \cdot A_\text{throat}) \tag{4.2}$$

where | C_F | : | thrust coefficient | $[-]$
| T_h | : | thrust | $[N]$
| P_c | : | combustion chamber pressure | $[Pa]$
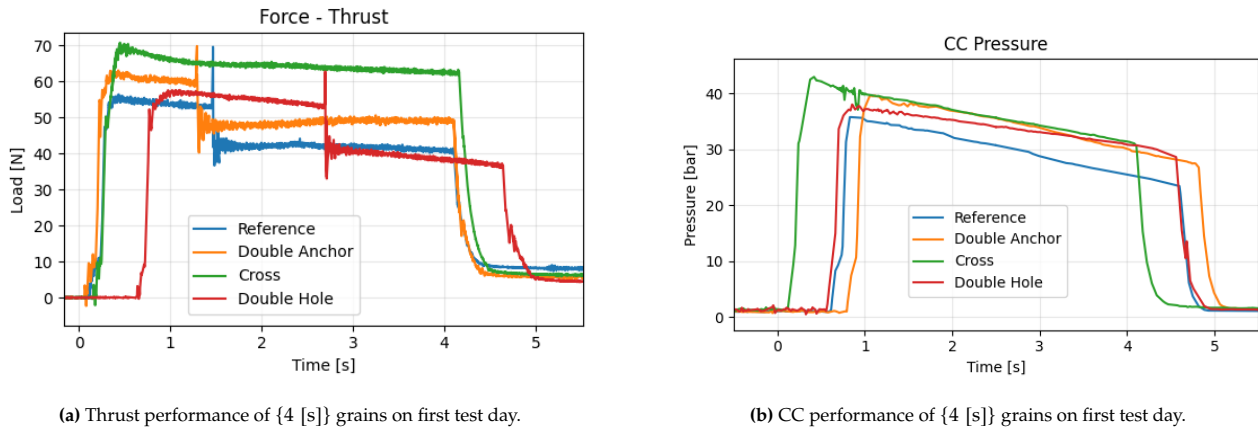| A_throat | : | nozzle throat cross-sectional area | $[m^2]$

4.4. Improvements

Improvements are always possible, and after the first test campaign, this is also the case. Already discussed in section 3.1.4, several improvements were made. From the data analysis front, the isentropic method for determining the oxidiser mass flow can be deemed relatively accurate, however it does operate under the assumption that no liquid appears within the system. It also needs to be heavily smoothened (which results in the peculiar curves seen in figure 4.9b). For the next campaign, the thermal probe will be used to record the temperature of the N_2O prior to the injector, and this information, combined with the injector manifold pressure will provide the density of the oxidiser as it enters the injector manifold. This should be a better representation compared to the current method which has to assume an oxidiser temperature.

4.5. Conclusion

In the first test campaign, sufficient information was gathered to compare the performance to the simulations, as well as comparing the performance between the various motors. Metrics such as the CC pressure and thrust are in the same order-of-magnitude as the test data collected, once consideration is made for the difference in initial conditions (both compared to the simulation as well as intra-geometries).

However, improvements should be made which would allow the gathering of more information which was not available at this stage of the campaign. By gathering more specific information, the modelling can be improved, and some of the assumptions made can be either verified, or replaced by test data. Most important would be the addition of the thermal probe sensor to measure oxidiser temperature - during the first set of tests, it is
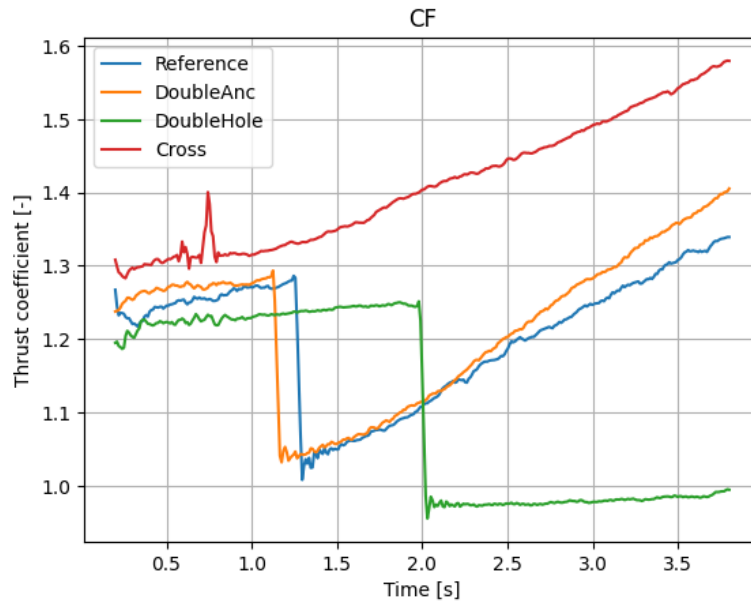
Figure 4.14: Thrust coefficient (with noticeable drop due to nozzle disintegration for the non-cross geometries).

inconclusive what the phase of the oxidiser is, which will inevitably affect ignition but also motor performance (especially if the phase changes throughout the motor test).

5

Second test campaign

The second test campaign entails improvements made with the lessons learned in the first campaign. This mostly includes a greater focus on a consistent tank pressure, as well as adding a thermal probe before the injector manifold. For the second test, the valves were also changed to minimise the pressure drop from the tank to the injector manifold (however this was reversed for the third test since this could have contributed to the variation in results from the second test). The third test also included taking the oxidiser from the top of the tank to promote only gaseous oxidiser - as shown in figure 3.10, the motor started with liquid oxidiser (and further confirmed via CoolProp [12] in the plotting of oxidiser density over time in figure 3.10c).

Lastly, the second test aimed to have four tests of {8 [s]}, which would be repeated for redundancy and repeatability in test 3. However, due to the execution of test 2, also where ignition seemed more unreliable and the lower pressure drop, the third test will consist of {4 [s]} tests - in other words, a repeat of the first test campaign but with the thermal probe and a guarantee of gaseous N_2O.

5.1. Test 2

As already touched upon in section 3.2.3, the second test campaign had many difficulties compared to the first campaign. The first difficulty is that, aside from the double anchor geometry, the data consists either of a cold flow, or a test that was aborted during the test. Secondly, the double anchor geometry was incredibly unstable (reaffirmed by the overlapping pressure data in figure 3.11c). This also means that, since the CC pressure sensor was damaged (determined after-the-fact since the ambient reading did not go back to approximately {1 [bar]} - figure B.1b), a lot of the data required for analysis was not available nor usable.

In light of the above, while the (raw) results of the second test day are viewable in appendix B, they will not be further analysed.

5.2. Test results - test 3

For the third test, the setup was done in such a way that maximised the possibility of gaseous N_2O (by using the top of the tank instead of the bottom), and the setup was reverted to using the same valves of the first test. As already mentioned, the reference geometry failed to fire[1].

Additionally, only the double anchor and cross geometry will be analysed in a similar manner to the first test as this set of results was sufficiently complete to do so. The double hole geometry, however, will only be partially analysed due to the unusable CC pressure.

Oxidiser mass flow

Similarly to the first test analysis, the amount of oxidiser used will be calculated in two methods. So-called "Method 2" (as used for the first test) will be used. This required the isentropic relations, as well as *a priori* information on the behaviour of the run-tank. The so-called "Method 3" uses the thermal probe, alongside the injector manifold pressure to calculate the density of the oxidiser at the injector manifold. Using an assumed

---

[1]On the day it was suspected that a skipped step in setting the motor for ignition was the cause for this. It was attempted to fire the reference geometry after the remaining motors had fired, however a feedsystem failure of the bleed valve (BV) meant that once the double hole geometry was tested, no more testing was possible without a replacement part - which was not possible.

Table 5.1: Measured parameters from the various motors tested during the second test campaign ({8 [s]} burn time). The blue cell indicates a cold flow, while the yellow cells indicate a test abort. The red cell indicates the nozzle broke during the test. RF: Reference, CR: Cross, DH: Double hole, DA: Double anchor.

Test	Before test		After test		Notes
	Grain mass [g]	Nozzle mass [g]	Grain mass [g]	Nozzle mass [g]	
RF 8.1	61.83	49.22	61.83	49.22	Test cold flow. Most likely overcooked the engine, meaning the ignition did not work as intended
CR 8.1	51.95	49.96	47.94	49.96	System auto-aborted due to DAQ mis-interpreting signal
DH 8.1	61.24	49.83	59.37	49.79	Motor test aborted by DARE SO due to anominal visual performance of motor. Upon inspection, partial break in divergent part of the nozzle.
DA 8.1	55.59	49.86	23.50	48.98	Motor test nominal. The exhaust flame appeared unstable in the initial phases of motor firing.

Table 5.2: Measured parameters from the various motors tested during the third test ({4 [s]} burn time). The blue cell indicates a cold flow. RF: Reference, CR: Cross, DH: Double hole, DA: Double anchor.

| Test	Before test		After test		Notes
	Grain mass [g]	Nozzle mass [g]	Grain mass [g]	Nozzle mass [g]	
RF 4.3	62.19	50.10	62.19	50.10	Ignition failed, cold flow
CR 4.2	52.10	50.00	36.70	49.96	Motor firing nominal
DH 4.2	61.53	49.85	41.19	49.71	Firing sequence completed nominally, however motor appeared "stronger" than the other motors. Pressure sensors for CC and injector not usable for data analysis
DA 4.2	56.00	49.78	37.91	49.71	Motor firing nominal and visually stable

discharge coefficient of $\{0.6 \, [-]\}^2$, the oxidiser mass flow can be calculated with equation (2.1). This resulted in the total oxidiser used in table 5.3 under the "M3" column. The different methods can be visualised in figure 5.1a, where "M2" corresponds to the "isen" label in the legend and "M3" as "CC".
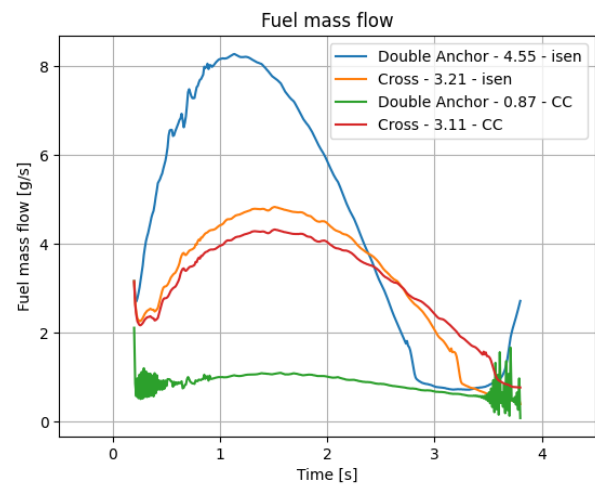
Fuel mass flow

Fuel mass flow, like for the first test, was used in two ways for further analysis. The first is with the same method as test 1, using equation (4.1) (instantaneous fuel mass flow). The fuel mass flow can be seen in figure 5.1b with the legend showing the time-averaged fuel mass flow. As already indicated, a slightly different discharge coefficient was necessary for the system as this otherwise caused numerical instability (specifically for the oxidiser mass flow). The second method is by assuming a constant fuel mass flow, as indicated in table 5.3 and refers to the average fuel mass flow when taking the difference between the start and end mass of the fuel grains measured. This is only for the third test.

Table 5.3: Calculated parameters from the various motors tested during the third test. RF: Reference, CR: Cross, DH: Double hole, DA: Double anchor.

Test	Maximum thrust	Maximum P_c	Start P_{tank}	Impulse	ABS used (avg. $\dot{m}_f$)	M2 N_2O used (avg. $\dot{m}_{ox}$)	M3 N_2O used (avg. $\dot{m}_{ox}$)	avg. O/F - M2	avg. O/F - M3	M2 - I_{sp}
Unit	[N]	[bar]	[bar]	[N s]	[g] ([g s^{-1}])	[g] ([g s^{-1}])	[g] ([g s^{-1}])	[−]	[−]	[s]
CR 4.2	70	38.6	48.1	264	15.40 (3.85)	76.7 (19.2)	76.9 (19.2)	4.98	4.99	292
DH 4.2	70	Unknown	47.4	249	20.34 (5.09)	68.1 (17.0)	Unknown	3.35	Unknown	287
DA 4.2	65	38	48.3	258	18.09 (4.52)	68.5 (17.1)	95.1 (23.8)	3.79	5.26	304
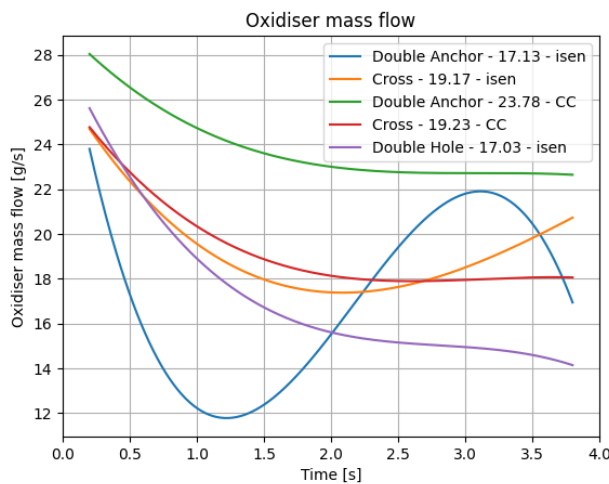
(a) Oxidiser mass flow. The numbers found in the legend refer to the the average of the plotted lines shown.

(b) Fuel mass flow. The numbers found in the legend refer to the the average of the plotted lines shown.

Figure 5.1: Propellant mass flows for the third test with instantaneous fuel mass flow model. The "isen" qualifier refers to the isentropic method of calculating the oxidiser mass flow with equation (2.7), while the "CC" qualifier refers to the method using equation (2.1).

5.2.1. O/F ratio

Using the various methods for determining the oxidiser and fuel mass flow, the O/F ratio can be examined and shown in figure 5.2.

The first observation is between the two sets of data. Figure 5.2a uses a variable fuel mass flow. For the tests that could be analysed, the cross geometry did not seem to differ significantly with either method, which indicates that, for that particular test and conditions, the corresponding discharge coefficient could be reasonable, assuming that the emptying of the oxidiser tank can be modelled isentropically as claimed by Newlands 2012 [16]. On the other hand, the double anchor has a much greater variance. On the variable fuel mass flow front (figure 5.2a), the O/F ratio is very sensitive to the fluctuations near the start and end of the motor test, and is drastically different compared to the isentropic approach. The constant fuel mass flow method's O/F ratio is not a great improvement, however here the influence of the oxidiser mass flow can be clearly seen in figure 5.2b.

---

[2]Originally this had a value of $\{0.7 \, [-]\}$, however this provided a significant instability where the oxidiser mass flow would result in a negative fuel mass flow, which led to a negative O/F ratio, which resulted in nonsensical data from RocketCEA. With a slightly lower discharge coefficient, this was resolved. A plot showing the unstable resultant combustion temperature can be found in appendix D.
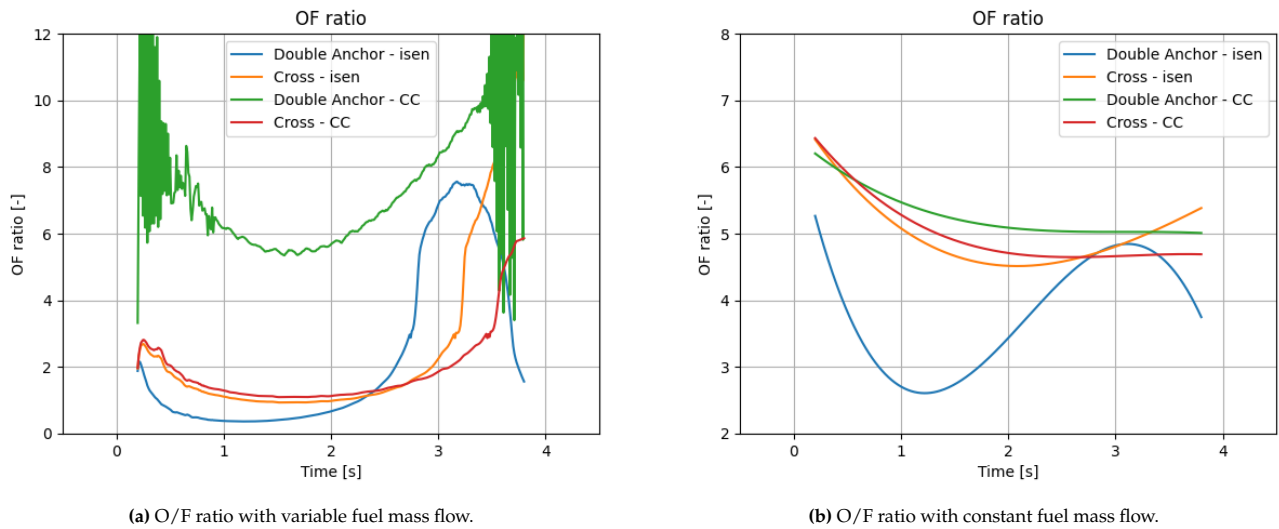
(a) O/F ratio with variable fuel mass flow.

(b) O/F ratio with constant fuel mass flow.

Figure 5.2: O/F ratio on different fuel mass flow models.

Influencing factors

The greater variation can be caused by numerous factors, however the first factor that should be touched upon is the influence of RocketCEA. It has already been seen that, with the current model setup, it is very sensitive to slight changes. For the calculations of the O/F ratio, factors which are taken as input from RocketCEA, as with the first test, include the combustion temperature and specific gas constant.

Figures 5.3a to 5.3d illustrate these various influences. In terms of order-of-magnitude, the fluctuations in value still centralise around the same values as with the constant fuel mass case shown in figures 5.3b and 5.3d, especially for the isentropic oxidiser mass flow method with the double anchor geometry. However, most likely caused by numerical instability, if particular input parameters cause fluctuations in the inputs, the outputs are also affected, and in some cases amplified.

5.3. Inter-motor performance

For the data that is available, the motors can also be compared. As with the first test campaign, the thrust and CC pressure are firstly compared and treated.

The thrust performance (from figure 5.4a) are very similar. The only difference is the reference geometry (which did not ignite) and the double hole geometry which drops off slightly faster than the other geometries. Numerous reasons for this could exist, however it can be a likely cause that this motor had a greater-than-expected pressure performance in the CC, resulting in a lower oxidiser mass flow (however this cannot be confirmed with the current data set). This was the case in the first test campaign (figure 4.13b) when comparing the double hole and reference geometries (which can be the most easily compared since these geometries had the same initial tank pressure).

The CC pressure also behaves very comparably between the two grain geometries with data available - shown in figure 5.4b. The double anchor has a slightly slower decaying CC pressure. While it is not possible to isolate the direct cause, one such factor of a higher fuel mass flow (as shown, via the isentropic oxidiser mass flow method in figure 5.1b) could contribute overall to the combustion process, resulting in a greater back-pressure. Due to the complex nature of the combustion process, this would inevitably also impact combustion temperature, specific heat ratio and the gas constant, all of which being parameters that could not be measured.

Like with the first test, the thrust coefficient was also computed in figure 5.5. Ultimately, the difference is not incredibly different, however the cross geometry is, like with the first test in figure 4.14, the "best" geometry (however the comparison is only possible with one other geometry).

5.4. Conclusion

Ultimately, the second series of tests were not big contributors to understanding the impact of different grain geometries. Several improvements were attempted, however other factors significantly impacted the usefulness of the data, and for the purpose of this study, was ignored.
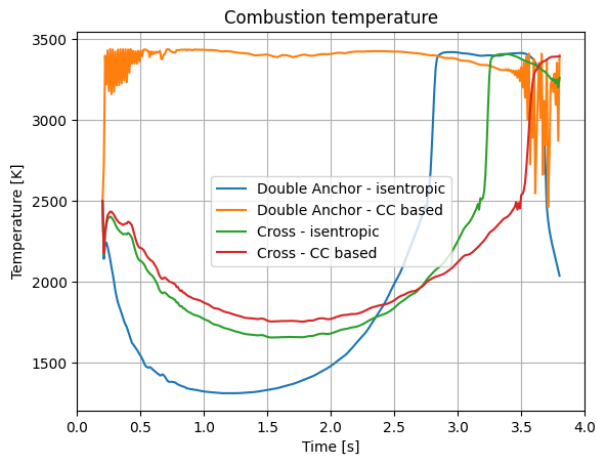
(a) Combustion temperature with variable fuel mass flow, test 3.
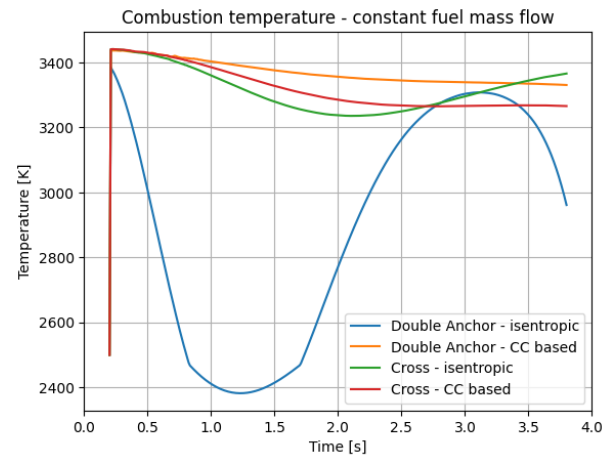
(b) Combustion temperature with constant fuel mass flow, test 3.
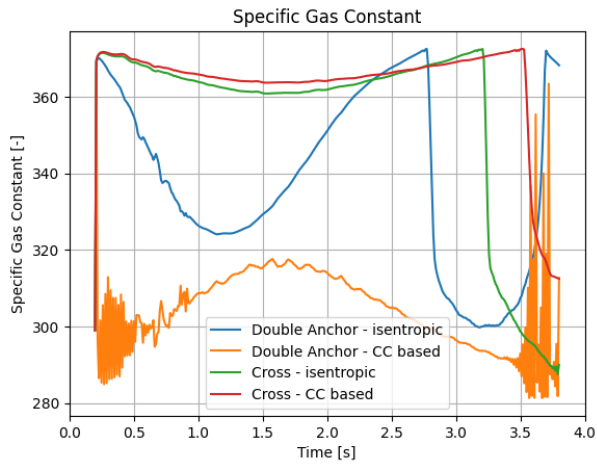
(c) Specific gas constant with variable fuel mass flow, test 3.
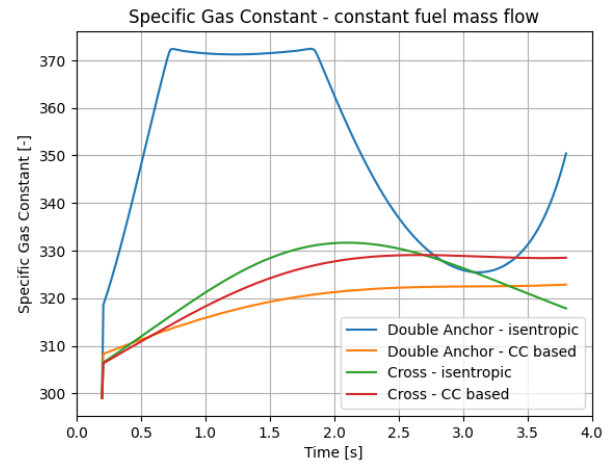
(d) Specific gas constant with constant fuel mass flow, test 3.

Figure 5.3: Inputs to RocketCEA and their sensitivity to varying fuel mass flows.
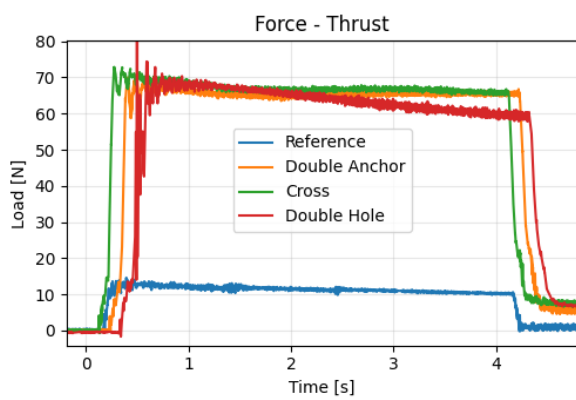
(a) Thrust performance of 4s grains on third test day.
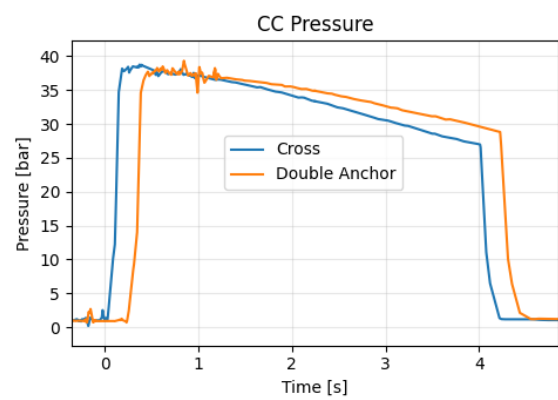
(b) CC performance of 4s grains on third test day.

Figure 5.4: Thrust and CC pressure during the third test day.
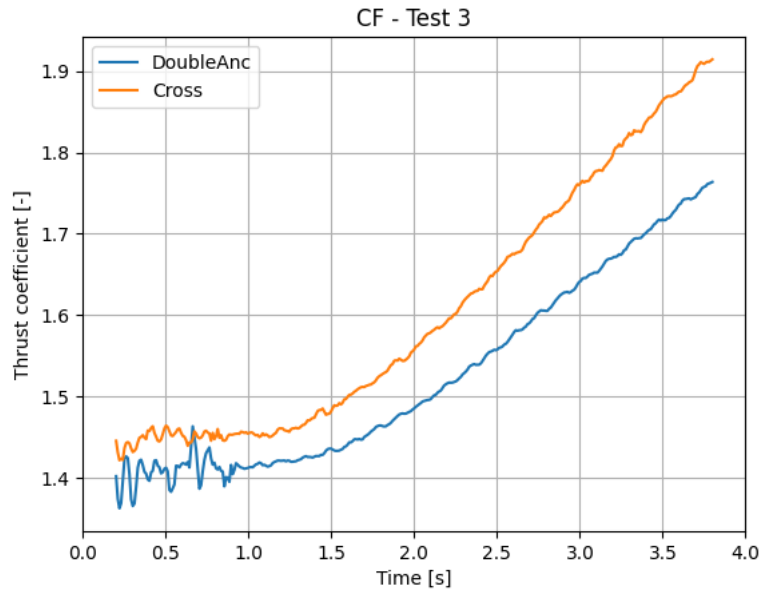
Figure 5.5: Thrust coefficient for test 3.

The third series of tests proved more useful. While the double hole and reference geometry provided no usable data, sufficient information was gathered for the remaining geometries that an analysis could be performed - especially on the front of the O/F ratio (which ultimately is one of the project goals).

6

Verification and Validation

This chapter will focus on assessing the simulation model and comparing this to the data collected, as well as quantifying the differences in particular parameters. Potential sources for discrepancy will also be discussed.

For the purpose of this chapter, the (type of) data that will be compared between the model and experiment has to be carefully selected. This is mostly due to the varied information that was available, per test.

For that reason, the results from the first test will be taken, but purely in terms of performance for thrust and CC pressure. The results from the third test will also include the thrust and CC pressure, however the oxidiser and fuel mass flow will also be assessed.

Additionally, in order to compare how the model simulates performance, several inputs have to be slightly changed. The first input is the tank pressure over time. In the original simulation results (see figures 4.1 and 4.2), the initial tank pressure was set to {44 [bar]} and followed a pressure curve tabulated in table 2.1. Tank pressure over time is known, therefore for every set of test data that is used in the verification and validation process, the respective tank pressure data will be used.

Since the simulation model depends on tank pressure, the ambient temperature measured during every test will also be taken as a varied input per test - this will dictate the starting oxidiser density.

Section 6.1 describes the method by which the deviation between the simulation and the test data is computed, as well as looking at the deviation present between the CC pressure and thrust measured. Subsequently, section 6.2 does the same, but using the data collected during the third test. In addition to the CC pressure and thrust, the O/F ratio is also looked at (however this is compared in absolute terms).

6.1. Comparing test 1 data

For the first test, the CC pressure and thrust performance will be compared (however for the thrust performance, it can only be partially evaluated in terms of accuracy due to the nozzles breaking). For both these parameters, the data will be compared to the simulation, as well as a percentage difference compared to the simulation. The difference will be calculated with equation (6.1):

$$\Delta\% = 100 \cdot \frac{\text{SIMULATION} - \text{EXPERIMENT}}{\text{SIMULATION}} \qquad (6.1)$$

If the experimental data exceeds the simulation data, the percentage difference will be negative (meaning the simulation underestimates the experimental data) and vice versa.

6.1.1. Combustion chamber pressure

The difference between the model and the experimental data can be seen in figure 6.1 (with raw data viewable in appendix E.1). It can be seen that the model can definitely improve, however depending on the geometry, it is fairly accurate. An underestimation of {20 [%]}, to an overestimation of approximately {10 [%]} seems to be the range (geometry dependent). It should also be noted that the y-axis is limited - due to the imperfect alignment of data, the starting values can mathematically differ many orders of magnitude which obfuscates the

remaining data. Therefore, these boundary cases are ignored and the plots showing the differences between the simulation and experimental data are primarily assessed once the difference has stabilised.

The first time period has a greater sensitivity in startup behaviour and alignment of data. It was observed (although not included in this report) that a numerical instability was present in the simulation - mostly caused by a big difference between the CC pressure and tank pressure at startup, when in the next timestep this is over-corrected. These fluctuations take several timesteps to dampen. This problem was resolved by taking a finer timestep at the cost of computation time.

It should also be noted that for the double anchor geometry, the discharge coefficient, proved to be a source of numerical instability. This had to be changed, for the model with the respective "up-to-date" inputs, to $\{0.1 \ [-]\}$. This is a large difference - this has a linear impact on the modelling of the oxidiser mass flow - but nonetheless shows more and more that accurately modelling the oxidiser mass flow for this simulation is a source of inaccuracy, and only demonstrates further the need for a mass flow meter.
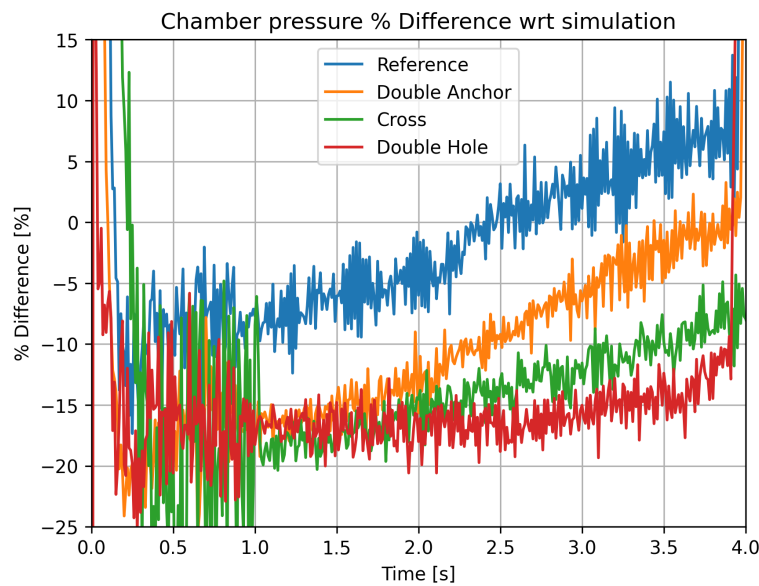

Figure 6.1: Percentage difference of CC pressure experimental data (test 1) vs simulation data.

6.1.2. Thrust

While the CC pressure tended to be underestimated by the simulation, the thrust was regularly overestimated (except for the cross geometry which achieved a full burn). In order to calculate the thrust, the propellant mass flow and specific impulse are inputs - the latter is determined from RocketCEA, but more importantly, the specific impulse was the vacuum rated specific impulse. This can very quickly point to the over-estimation (assuming that the propellant mass flow be accurate enough that the specific impulse be dominant). An additional correction takes place which subtracts the ambient pressure term present in determining the thrust. It is also peculiar that the geometries that had a mid-test anomaly were all over-estimated by the model, while the single geometry that was successful was underestimated. This indicates that, while the specific impulse will be overestimated (in principle), a discrepancy is not being modelled sufficiently and has a greater influence than the specific impulse.

Additionally, for the geometries that had mid-test anomalies, the over-estimation (deviation) is less than $\{10 \ [\%]\}$. It is also observed in figure 6.2, and most obvious for the double hole geometry that the deviation has a negative slope. With some extrapolation, it would not be unreasonable to assume that all thrust curves would end up following a similar trend to the cross geometry.

6.2. Comparing test 3 data

Similar to test 1, the CC pressure and thrust will be checked between the data that was collected and what the simulation indicated. It is also interesting to note that this experimental data contains more supplementary information - as an example, it is known via the thermal probe that gaseous N_2O arrived at the injector manifold. This remains an open question - a question that cannot be answered - for the first test. It is even possible that the
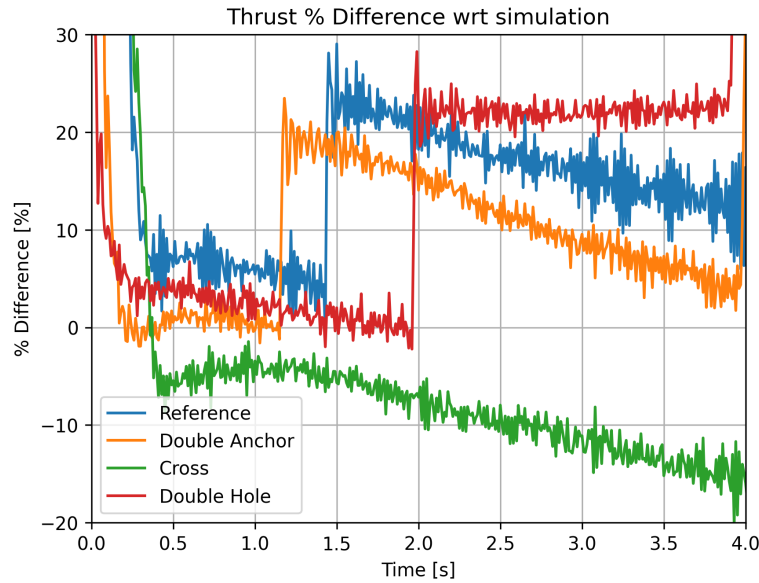
Figure 6.2: Percentage difference of thrust experimental data (test 1) vs simulation data.

first tests started with some liquid oxidiser since the oxidiser supply was taken from the bottom of the run-tank, while for the third test, this was changed to the top.

6.2.1. Combustion chamber pressure

Relatively speaking, the model maintains a similar inaccuracy as with the first test for CC pressure simulation (figure 6.3). In both sets of tests, the double anchor starts with a deviation of $\{-15\ [\%]\}$. In the first test the difference gets to nearly $\{0\ [\%]\}$, while the third test a difference of $\{-5\ [\%]\}$ remains. For the cross geometry, the first test starts at a deviation of $\{-20\ [\%]\}$ and ends also around $\{-5\ [\%]\}$, while the third test starts at $\{-11\ [\%]\}$ and comes to around $\{2\ [\%]\}$ at the end of the test.

It should be noted that a similar numerical stability that was experienced with the cross geometry during the first test - which resulted in a lower discharge coefficient - appeared for the double anchor geometry for this set of test data. Instead of a coefficient of $\{0.3\ [-]\}$, this was decreased to $\{0.25\ [-]\}$. This difference is significantly smaller than the change that was necessary in the first test; a slightly smaller discharge coefficient slightly lowers the oxidiser mass flow, meaning that with all other factors being equal, the CC pressure in the simulation is smaller. This can be seen in the comparison, however other factors like the O/F ratio, combustion temperature etc. will undoubtedly affect the results. It remains an open question of the scale of the impact due to this being a multi-input parameter.

6.2.2. Thrust

The thrust curves in figure 6.4 follow a similar trend with the successful cross geometry during the first test, including a similar order-of-magnitude of inaccuracy (which generally increases over time - the simulation models a greater drop in thrust compared to this set of experimental data). At the start of the test, the model is practically exact with the experimental data, and ultimately decreases to the model underestimating the thrust by $\{20\ [\%]\}$. This could be explained by the impact of a changing specific impulse (which is generally also affected by the O/F ratio amongst other things).

6.2.3. O/F ratio

In this project, the goal was to investigate whether the O/F ratio could be flattened, hereby minimising (with future designs) how much the O/F ratio changes, which in turn would allow engineers to design a grain that operates at optimum conditions (e.g. temperature, specific impulse etc.).

Figures 6.5a and 6.5b showcase the difference in the O/F ratio (in absolute terms) between the simulation results and the two different methods to determine oxidiser mass flow (isentropic and pressure difference over the injector). At the very least, there is a wide discrepancy between the physical results and the simulation data, and with a bigger difference for the double anchor geometry. The cross geometry also differs by a factor of three, however the two oxidiser mass flows with the associated fuel mass flow do present a similar story.
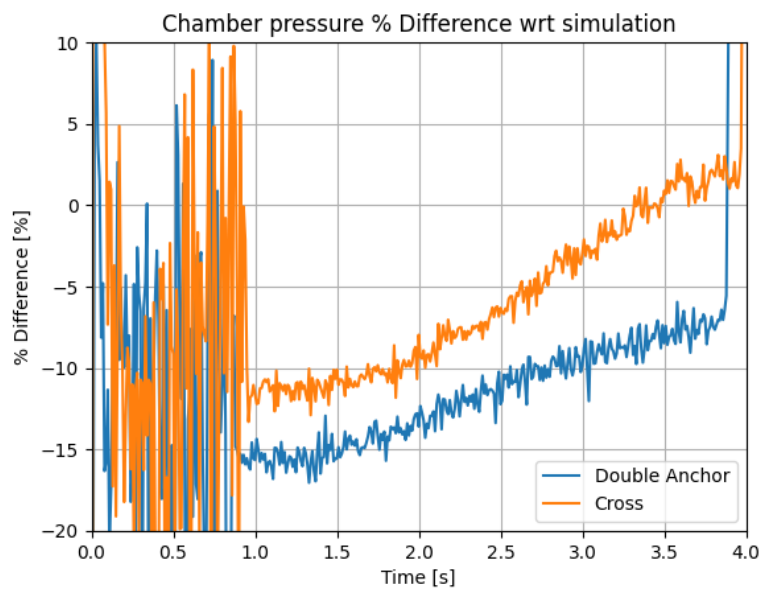
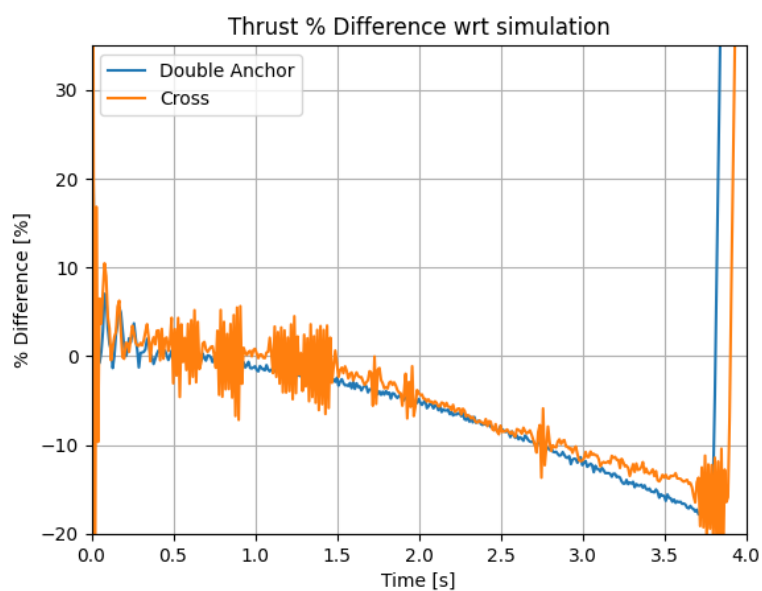**Figure 6.3:** Percentage difference of CC pressure experimental data (test 3) vs simulation data.

Figure 6.4: Percentage difference of thrust experimental data (test 3) vs simulation data.

(a) Double Anchor O/F ratio w.r.t. simulation data.

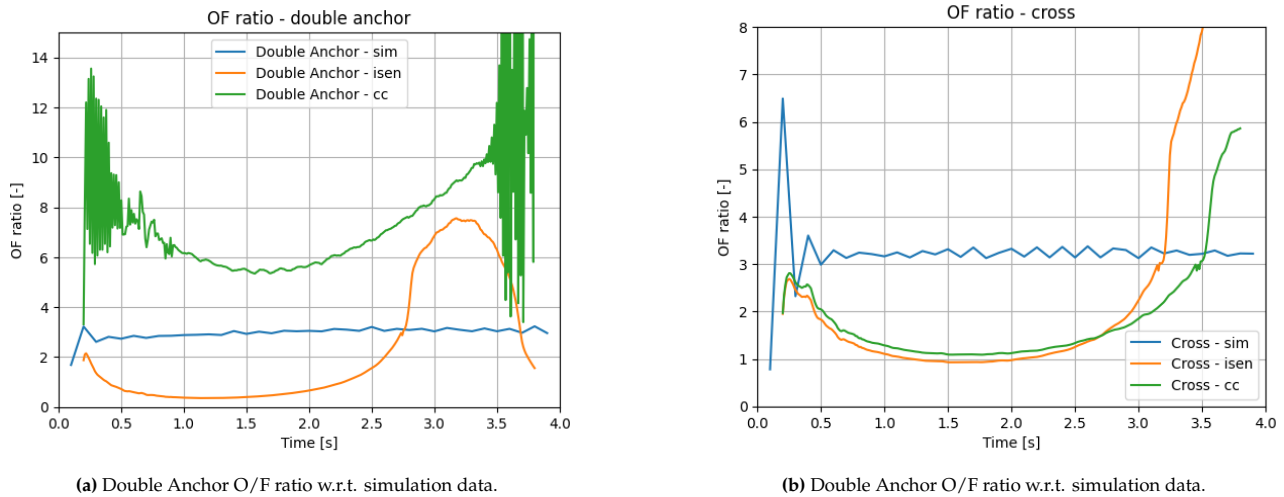**(b)** Double Anchor O/F ratio w.r.t. simulation data.

Figure 6.5: O/F ratio for double anchor and cross geometry (test 3) compared to simulation data.

Both propellant mass flows play a role (with the data plotted in appendix E.3). For the cross geometry, the oxidiser mass flow is fairly accurate, with the simulation overestimating by approximately $\{3\ [\mathrm{g\,s^{-1}}]\}$ at the greatest difference (meaning the simulation either overestimated the oxidiser mass flow, assuming the data processing perfectly models the oxidiser mass flow, or the assumptions such as discharge coefficient underestimated the oxidiser mass flow). This counts for both oxidiser mass flow methods. The double anchor differs here significantly more, and plays a role in the varied O/F ratio. For the fuel mass flow, the cross geometry is quite different when compared between the simulation and the data processing methods, so there is definitely a great source of inaccuracy in this information. It does have to be said, however, that both processing methods produce close to identical results. For the double anchor, the fuel mass flow differs by close to a factor of eight between the two processing methods - however, it is reasonable that the isentropic method better matches the total fuel consumed.

While the CC and thrust results have a reasonable match (for both geometries), it is not possible to conclude that the O/F ratio is accurately modelling with this set of data.

Since the fuel mass flow is calculated with inputs from RocketCEA, and there being a sensitivity to numerical timesteps, there is reason to believe that this also impacts the results, a role that is also difficult to quantify since measures such as combustion temperature, and the specific gas constants (all inputs retrieved from RocketCEA) cannot be verified.

Due to the reasons above, it can be concluded that this aspect of the ballistics tool is not verified or validated. It is entirely possible that the results it produces are accurate, however the limitations in the data processing (and other sources of error) deem this aspect inconclusive.

6.3. Regression rate verification

As discussed in section 2.1, the original purpose for this model was for SRMs - this model was combined with a hybrids ballistics model to simulate how the different design choices made impact performance.

It was also mentioned that, while the model has been verified with certain analytical models, once testing has concluded, the regression model can be visually compared to the grains left over to see if large deviations are present.

Figures 6.6 to 6.9 show a visual match to the regression model. For all geometries, (and most obvious in figure 6.9), the regression ended around the green line in the figures. This visually proves that the shape that the regression takes from the simulation can be taken to be fairly accurate, and not a great source of uncertainty for the simulations. For the double anchor geometry, figure 6.7, the regression appears somewhere between the orange and green lines.
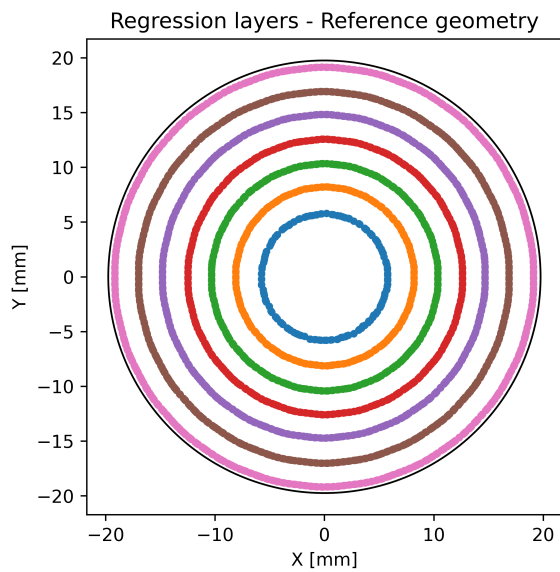
(a) Reference grain regression over time.

(b) Reference grain (test 1) after test.

Figure 6.6: Reference grain regression vs experiment.
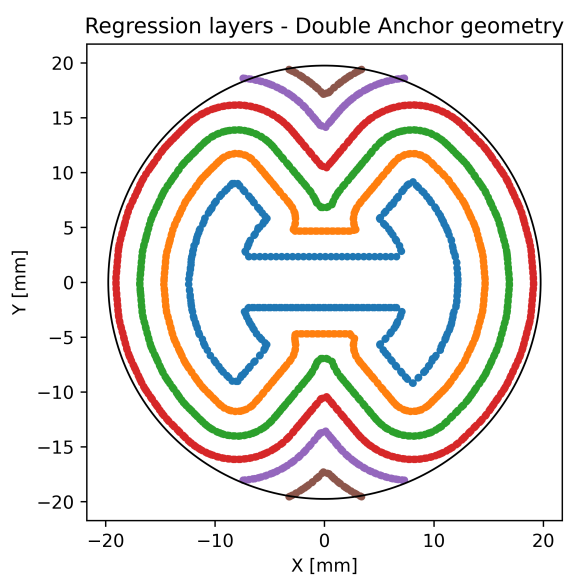
(a) Double anchor grain regression over time.

(b) Double anchor grain (test 3) after test.

Figure 6.7: Double anchor grain regression vs experiment.

(a) Cross grain regression over time.

(b) Cross grain (test 3) after test.

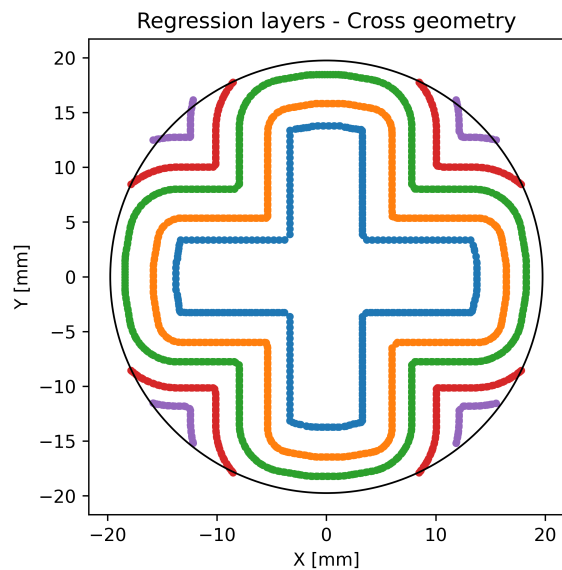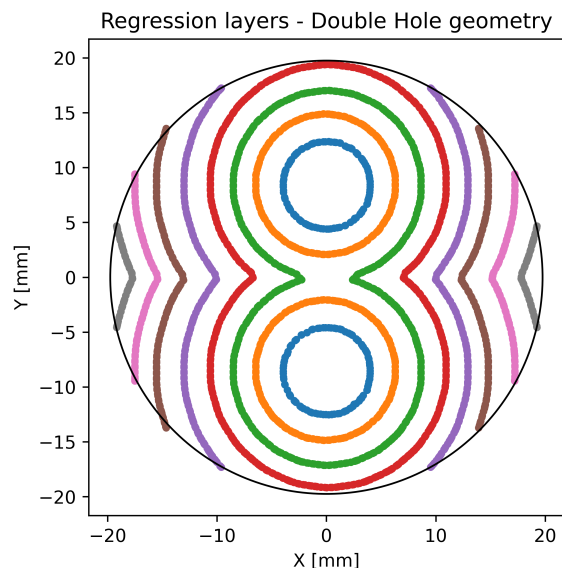**Figure 6.8:** Cross grain regression vs experiment.

(a) Double hole grain regression over time.

(b) Double hole grain (test 3) after test.

Figure 6.9: Double hole grain regression vs experiment.

6.4. Conclusion

The model used for this experimental study does have some strengths, however, whether the difference between results is acceptable is subject to debate. For this study, it could be claimed that it is sufficient - it remains that a proof-of-concept was the goal of this study, and not immediately an accurate simulation, so a discrepancy of {10 [%]} or {20 [%]} can even be acceptable. This does have a caveat - as elaborated on in future recommendations, many assumptions had to be made for modelling the oxidiser mass flow, and was subject to numerical sensitivities which could only be resolved by altering the discharge coefficient. Having equipment which directly measures this quantity would alleviate many sources of errors, and allow further focus on other factors (such as combustion temperature) which undoubtedly also affect the results.

In addition to this, while the characteristics that were measured matched relatively well (thrust and CC pressure), the characteristics which had to be inferred from the data cannot be deemed sufficiently modelled and explained. It is currently not possible to conclude whether the error lies on the simulation and the modelling, or whether a data processing step, numerical instability or simulation feedback is affecting these characteristics (such as propellant mass flow) and therefore this needs to be further evaluated and improved, combined with improved experimental setup to determine where the inaccuracies lie.

7

Conclusion and recommendations

This chapter will present the conclusions and recommendations of this experimental study. The RO and RQs will be reflected upon to evaluate whether these were achieved, or otherwise establish the factors of why this was unsuccessful. The future work and recommendations will also be treated, both in terms of further studies and applications, as well as areas where this study can be improved.

Section 7.1 reiterates the RO and RQs that were posed at the start of this report, and using the information presented, answers the RQs, as well as evaluating whether the RO was met.

Additionally, since many lessons were learned, but also limitations realised with this project, section 7.2 briefly touches upon any future research that can be done, but also how this work could be improved.

7.1. Research objective and questions

To reiterate, the following was established as the RO and RQs, back in chapter 1.

The RO was as follows:

> Investigate the effectiveness of using additive manufacturing for geometrical changes to ABS-N_2O HRMs that lead to wider adoption of the technology for in-space propulsive applications.

The RQs were as follows:

> 1. What categories of in-space propulsion applications can benefit from ABS-N_2O HRMs?
>   (a) Which characteristics can be deemed relevant to judge a propulsive system's appropriateness for various in-space propulsion applications?
>   (b) Which characteristics from HRMs are inherent advantages and disadvantages of the technology?
>   (c) Which class of in-space propulsive applications can benefit from 3D printed ABS-N_2O HRMs?
> 2. Which design parameters, within a grain geometry, can be altered to increase the suitability of ABS-N_2O HRMs for specific propulsive needs?
>   (a) Which design parameters can be altered that can facilitate test campaigns within TU Delft and DARE testing limitations?
>   (b) What theoretical metrics can be used to determine the effectiveness of a particular design?
>   (c) Which characteristics can be determined with the available test suite?
>   (d) To what extent is it possible to establish the effectiveness of these changes from experimental data?
>   (e) To what extent do the current testing limitations affect the ability to draw concrete conclusions about the impact of the changes made to the designs?

The first RQ was answered in section 1.8, concludes that at least two mission types are suitable for this style of propulsion system. HRMs are inherently safer and less complex than the solutions currently available, however

performance consistency can be seen as a big drawback for this system (but can be less important depending on the mission in question).

The second RQ is more difficult to answer, and ranges several chapters in this study. The first two sub-questions can ultimately be taken from chapter 2. In this study, the port geometry was taken to be the design parameter that can be altered. This allows a theoretical difference in performance and efficiency, while maintaining the same size as testing undertaken by Wubben 2022 [1]. The metrics of the O/F ratio was ultimately the main evaluator in the effectiveness between designs (although the actual O/F ratio was less important). If the project goals were to be achieved, the O/F ratio should be flatter compared to the most basic port geometry (the circular port). If this is achieved, future work can use this knowledge to further optimise.

Within testing limitations, this parameter can be indirectly measured. With several assumptions, the oxidiser mass flow can be determined, which ultimately affects the fuel mass flow. By simulating and calculating these parameters, and inputting this information into RocketCEA and CoolProp, the performance from the different motor configuration could be established, and to an extent showcase the effect of the changing geometry. However, the extent to which this was proven is still in question. Due to the indirect nature of measuring the oxidiser mass flow (and having to take certain assumptions regarding e.g. discharge coefficient), not to mention that a constant discharge coefficient was taken, this will provide one of the bigger sources of uncertainty, and therefore limit the conclusion that can be taken on whether the project goals were met. Nonetheless, theoretically the goal was achieved, but experimentally, without equipment to directly measure the oxidiser mass flow, the goal is not achieved.

The experimental data, especially from the third campaign, was similar to each other. Certain conclusions, such as the double anchor geometry having a lower mass flow when compared to the cross geometry (see figure 5.1a) can be drawn and is confirmed using the isentropic model taken from Newlands 2012 [16]. But again, without a direct measurement, this is still an open question.

Therefore, the last sub-question can be answered. Within the budgetary and testing constraints, a certain amount of information can be gathered, however the limitations in the model, especially when it comes to the indirect measurements of certain parameters, still create a lot of speculation about the different geometries and their effectiveness in achieving the project goals. In addition, the verification and validation of the model compared to the test data does show quite a discrepancy. While this can still be deemed sufficient as an "order-of-magnitude" approach, an improved model of the individual components (especially when it comes to modelling the oxidiser behaviour over the feedsystem) should firstly be done before further conclusions can be drawn.

Therefore, the question should be asked - was the RO achieved?

In the end, using additive manufacturing and 3D printing the fuel grains with different geometries did change particular performance metrics compared to the "standard" design. However, certain limitations in testing prevent a full-drawn conclusion to be made concerning the effectiveness. If the simulations are to be believed, a lot of potential exists to make an efficient in-space propulsion system, especially if this is combined with the other sub-systems present on the satellite/mission in question.

7.2. Future work and recommendations

Ultimately, this work paves the way for further research, and therefore certain recommendations can be made.

First off, equipment such as a mass flow meter suitable for the oxidiser and mass flow ranges should be utilised if further testing is to occur. This will allow a direct measurement of the oxidiser mass flow to take place, as well as an improved model for the injector used (and therefore, also improve the injector design which will prevent the events that occurred during test two and three). This will reduce the number of assumptions taken. This will also provide information on the accuracy of Wubben's injector model, especially for design parameters such as the discharge coefficient.

Additionally, a greater suite of temperature data should be gathered during the tank emptying process - assuming an isentropic process as described in Newlands 2012 [16] can definitely be valid, however confirming what the oxidiser temperature is at various points along the height of the run-tank area can further affirm this assumption, or otherwise showcase that this can also be a great source of error.

As determined with the verification and validation of the modelling tool with the O/F ratio, another experimental improvement would consist of the combustion temperature over time. This would remove one of the uncertainties that currently relies on a "black-box" operation from RocketCEA - this is not to say that the output from RocketCEA is unreliable, however due to the intricate relation between the specific heat ratio, O/F ratio and combustion

temperature, a feedback loop could exist which points to incorrect results; results which might balance out in the ballistics model, but results which do not when applied to experimental data.

From an experimental perspective, this study ultimately focused on a constant port geometry over the entire length of the grain. This also encompassed that the entire grain burned radially at the same rate, (which in practise is not the case), as well as the pre- and post-chamber not being taken into account. Therefore, this regression should also be improved as this would have undoubtedly affected the results from this study. By extension, this also means that the port geometry can transition over the length of the grain, a design choice that is definitely not achievable by traditional methods.

Outside the realm of experimental study, it should also be assessed about the market value of this technology. The system is less complex compared to the current market solutions available, but whether the mass and cost benefits exist is yet to be seen. This should also be evaluated, if and when this technology matures beyond the realm of research.

This page was intentionally left blank

References

[1] Rolf Wubben. 'Hydrocarbon Seeded ABS - Nitrous Hybrid Engine Development: Experimental Validation of an Analytical Design Tool'. en. MA thesis. Delft: Delft University of Technology, July 2022. URL: https://repository.tudelft.nl/islandora/object/uuid%3A7655afc0-97f1-4653-be26-b6bc5b003523 (visited on 06/09/2023).

[2] Stephen A. Whitmore et al. 'Development of a Power-Efficient, Restart-Capable Arc Ignitor for Hybrid Rockets'. In: *Journal of Propulsion and Power* 31.6 (2015). Publisher: American Institute of Aeronautics and Astronautics _eprint: https://doi.org/10.2514/1.B35595, pp. 1739–1749. ISSN: 0748-4658. DOI: 10.2514/1.B35595. URL: https://doi.org/10.2514/1.B35595 (visited on 05/09/2023).

[3] Kenneth K. Kuo and Martin J. Chiaverini, eds. *Fundamentals of Hybrid Rocket Combustion and Propulsion*. Reston ,VA: American Institute of Aeronautics and Astronautics, 2007. ISBN: 978-1-56347-703-4. URL: https://arc.aiaa.org/doi/abs/10.2514/4.866876 (visited on 11/12/2023).

[4] Roderick Wassenaar. *Literature Study - An investigation into hybrid rocket motors for in-space propulsion systems and its different applications*. English. Tech. rep. Delft: TU Delft, Oct. 2023.

[5] Stephen A. Whitmore and Sean D. Walker. 'Engineering Model for Hybrid Fuel Regression Rate Amplification Using Helical Ports'. In: *Journal of Propulsion and Power* 33.2 (Mar. 2017). Publisher: American Institute of Aeronautics and Astronautics, pp. 398–407. ISSN: 0748-4658. DOI: 10.2514/1.B36208. URL: https://arc-aiaa-org.tudelft.idm.oclc.org/doi/10.2514/1.B36208 (visited on 29/12/2023).

[6] Stephen Whitmore, Zachary Peterson and Shannon Eilers. 'Analytical and Experimental Comparisons of HTPB and ABS as Hybrid Rocket Fuels'. In: *47th AIAA/ASME/SAE/ASEE Joint Propulsion Conference & Exhibit*. _eprint: https://arc.aiaa.org/doi/pdf/10.2514/6.2011-5909. American Institute of Aeronautics and Astronautics, July 2011. DOI: 10.2514/6.2011-5909. URL: https://arc.aiaa.org/doi/abs/10.2514/6.2011-5909 (visited on 24/10/2023).

[7] Francesco Barato. 'Numerical and Experimental Investigation of Hybrid Rocket Motors Transient Behavior'. PhD thesis. UNIVERSITA' DEGLI STUDI DI PADOVA, Jan. 2013. URL: https://www.research.unipd.it/handle/11577/3423115?1/francesco_barato_tesi.pdf (visited on 24/10/2023).

[8] Dario Pastrone. 'Approaches to Low Fuel Regression Rate in Hybrid Rocket Engines'. In: *International Journal of Aerospace Engineering* 2012.1 (Jan. 2012). Publisher: John Wiley & Sons, Ltd, p. 649753. ISSN: 1687-5966. DOI: 10.1155/2012/649753. URL: https://doi.org/10.1155/2012/649753 (visited on 25/06/2024).

[9] B. T. C. Zandbergen. *Thermal Rocket Propulsion (v2.09)*. TU Delft, Sept. 2022.

[10] George Story et al. 'Hybrid Propulsion Demonstration Program 250K Hybrid Motor'. en. In: *39th AIAA/ASME/SAE/ASEE Joint Propulsion Conference and Exhibit*. Huntsville, Alabama: American Institute of Aeronautics and Astronautics, July 2003. ISBN: 978-1-62410-098-7. DOI: 10.2514/6.2003-5198. URL: https://arc.aiaa.org/doi/10.2514/6.2003-5198 (visited on 23/06/2024).

[11] Christos Margaritis. *A Solid Rocket Motor simulation tool*. Delft, 2023.

[12] Ian H. Bell et al. 'Pure and Pseudo-pure Fluid Thermophysical Property Evaluation and the Open-Source Thermophysical Property Library CoolProp'. In: *Industrial & Engineering Chemistry Research* 53.6 (2014). _eprint: http://pubs.acs.org/doi/pdf/10.1021/ie4033999, pp. 2498–2508. DOI: 10.1021/ie4033999. URL: http://pubs.acs.org/doi/abs/10.1021/ie4033999.

[13] Eric W. Lemmon et al. *"Thermophysical Properties of Fluid Systems" in NIST Chemistry WebBook, NIST Standard Reference Database Number 69*. Ed. by P.J. Linstrom and W.G. Mallard. Dinitrogen Monoxide. Gaithersburg MD, 20899: National Institute of Standards and Technology, 2023. URL: https://doi.org/10.18434/T4D303 (visited on 20/06/2024).

[14] Sanford Gordon and Bonnie J. Mcbride. *Computer program for calculation of complex chemical equilibrium compositions and applications. Part 1: Analysis*. NTRS Author Affiliations: NASA Lewis Research Center NTRS Report/Patent Number: NAS 1.61:1311 NTRS Document ID: 19950013764 NTRS Research Center: Legacy CDMS (CDMS). Oct. 1994. URL: https://ntrs.nasa.gov/citations/19950013764 (visited on 21/06/2024).

[15]   Charlie Taylor. *RocketCEA*. Mar. 2024. URL: https://rocketcea.readthedocs.io/en/latest/index.html.

[16]   Rick Newlands. *Modelling the nitrous run tank emptying*. English. Tech. rep. File had to be accessed via Wayback Machine due to danger warnings in local browser. Aspire Space, Jan. 2012, p. 20. URL: https://web.archive.org/web/20170113233129/http://www.aspirespace.org.uk/downloads/Modelling%20the%20nitrous%20run%20tank%20emptying.pdf.

[17]   Stephen A. Whitmore. 'Three-Dimensional Printing of "Green" Fuels for Low-Cost Small Spacecraft Propulsion Systems'. en. In: *Journal of Spacecraft and Rockets* 55.1 (Jan. 2018), pp. 13–26. ISSN: 0022-4650, 1533-6794. DOI: 10.2514/1.A33782. URL: https://arc.aiaa.org/doi/10.2514/1.A33782 (visited on 18/12/2023).

A
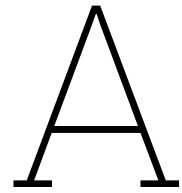
Data Validity - Test 1

In this appendix, all graphs of all sensors from the first test can be found which was used to establish whether particular sensors, from particular motor configurations, had to be ignored due to the values they produced. This could be sensors exceeding their operational range during the test, or otherwise the sensor not returning to a reasonable value. As an example, a pressure sensor that records the pressure within the injector manifold, should return to ambient pressure after a motor test.

A.1. Pressure sensors
Figure A.1 shows all pressure sensor readings collected during the first test. All pressure readings seem usable.

A.2. Load cells
Figures A.2 and A.3 showcase the load cell sensor readings of the different configurations for the first test. No indications of unusable data.

A.3. Thermocouples
Figure A.4 shows the top and bottom temperatures of the run-tank. All readings indicate no abnormalities.

A.4. Piezoelectric sensors
Figures A.5 to A.7 showcase the piezoelectric sensor measurements taken during the first test day. These results seem reasonable and expected since these are comparable to the data collected during the tests conducted by Wubben 2022 [1].
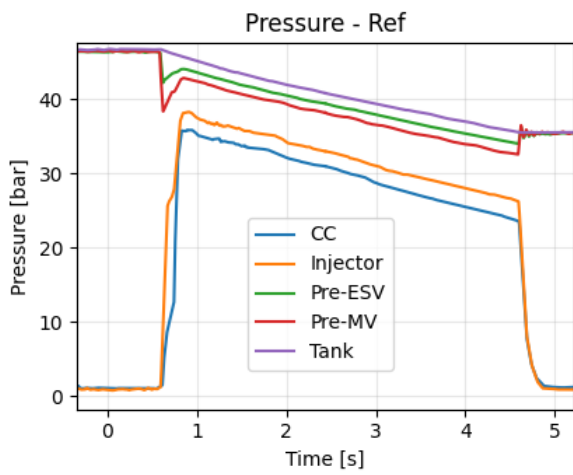
(a) Reference grain geometry
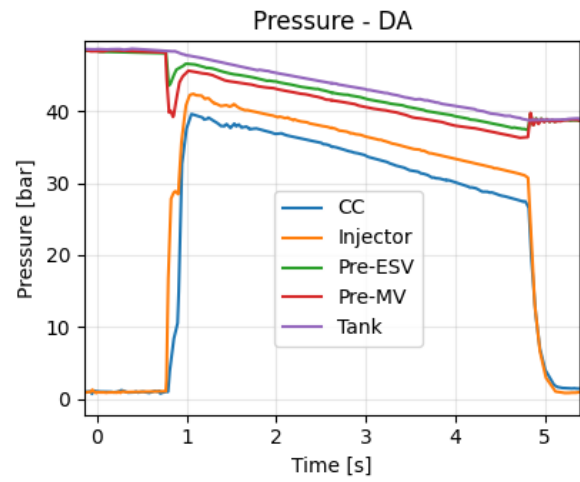
(b) Double anchor grain geometry
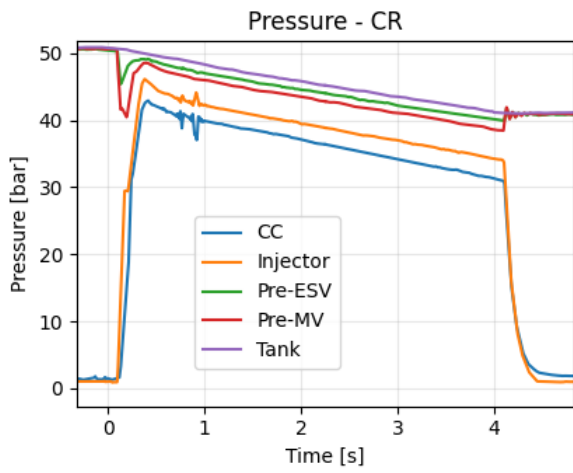
(c) Cross grain geometry
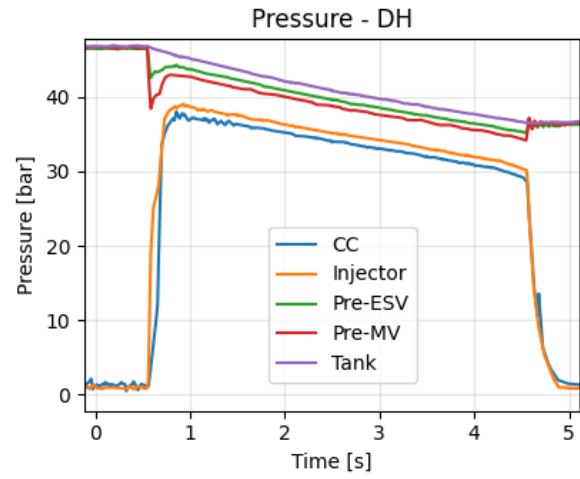
(d) Double hole grain geometry

Figure A.1: Pressure sensor data collected on first test day (14 March 2024)
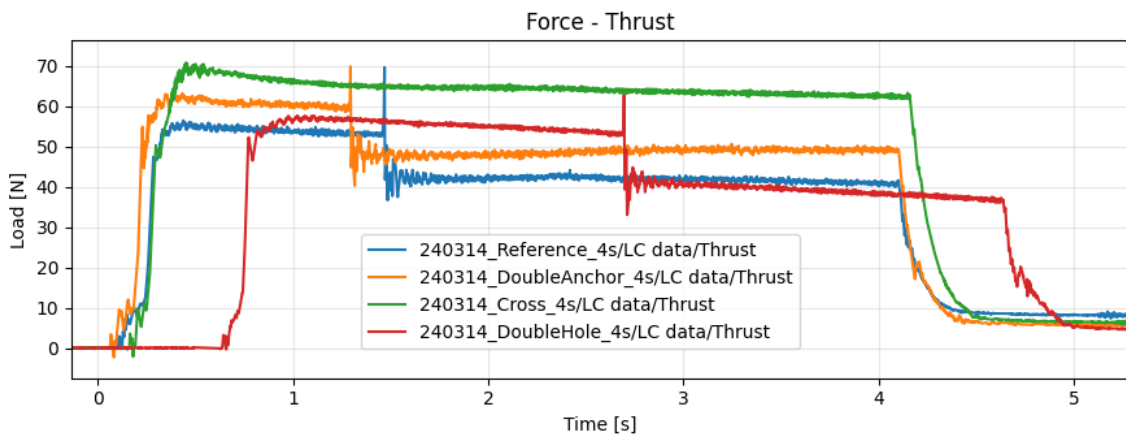
Figure A.2: Thrust data for the first test day (14 March 2024)
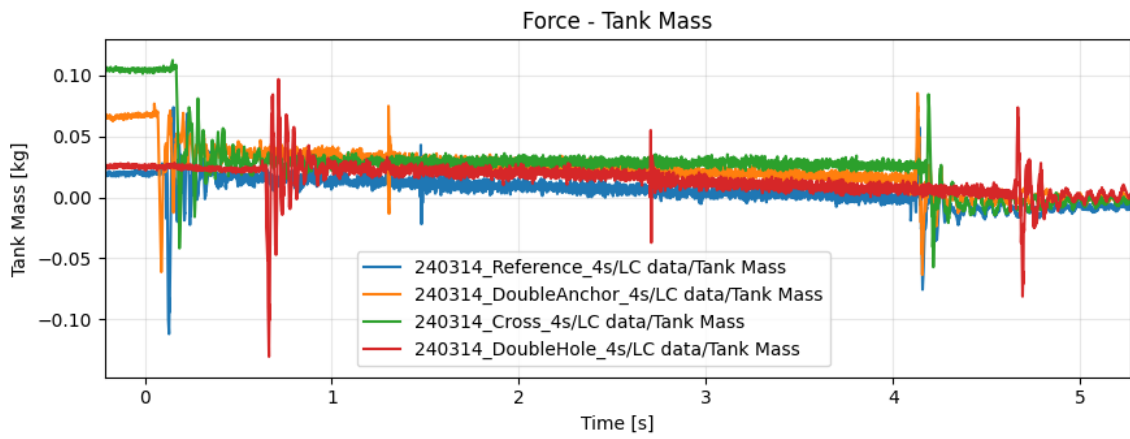
Figure A.3: Tank mass data for first test day (14 March 2024)
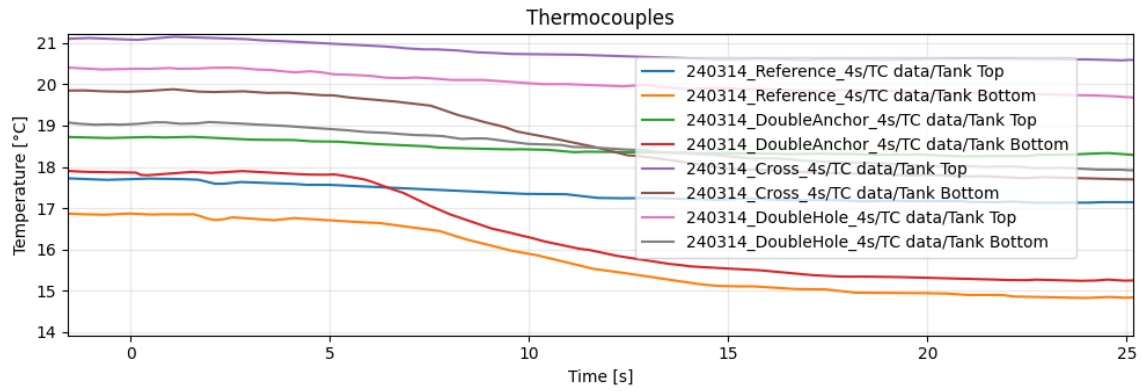
Figure A.4: Tank temperature measurements for the first test day (14 March 2024)
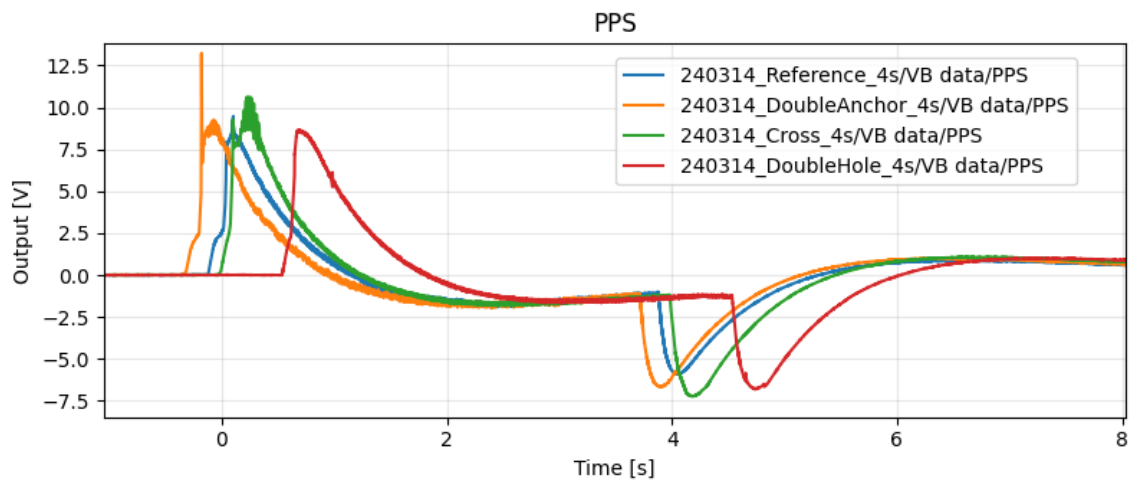
Figure A.5: PPS sensor data for first test day (14 March 2024)
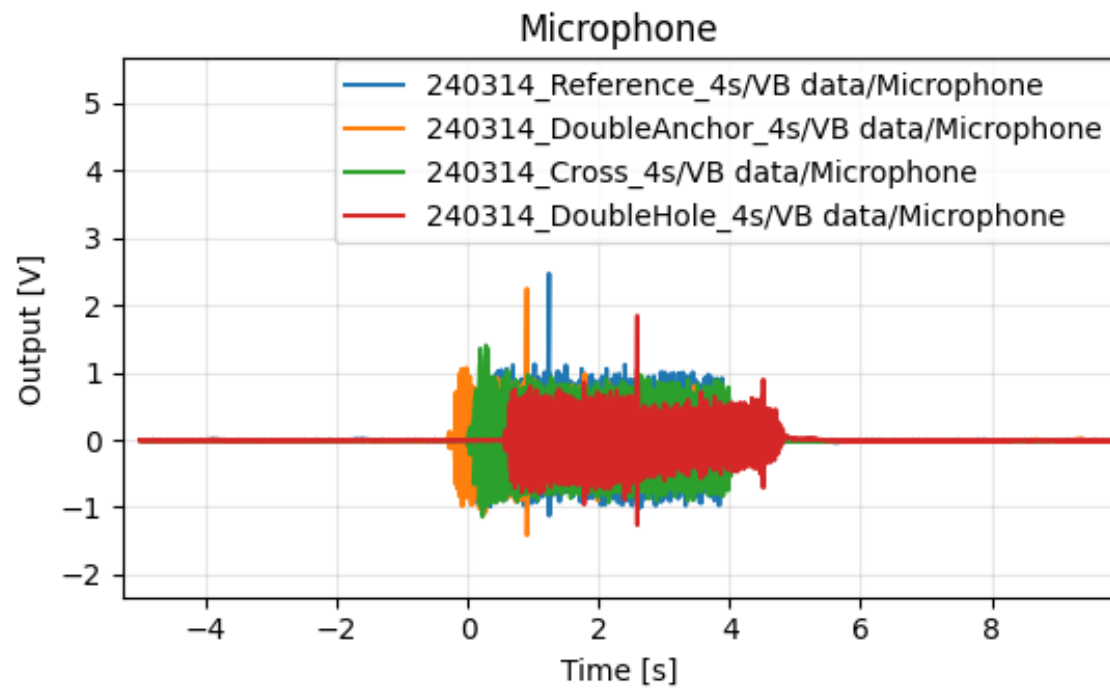
Figure A.6: Microphone sensor data for first test day (14 March 2024)
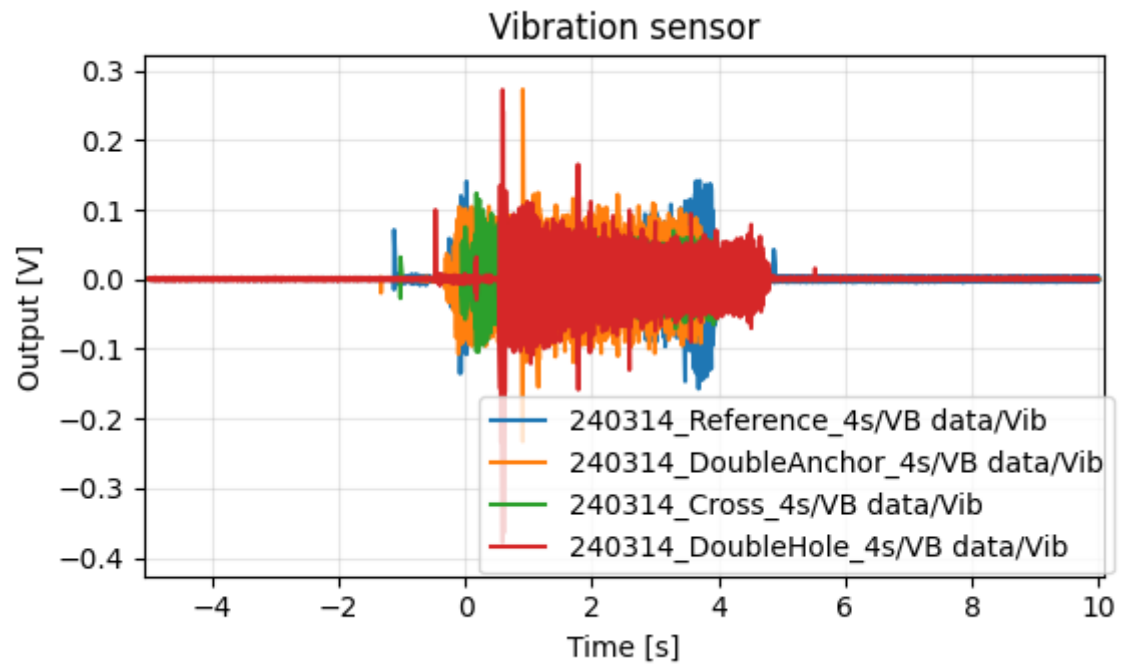
Figure A.7: Vibration sensor data for first test day (14 March 2024)

B

Data Validity - Test 2

In this appendix, all graphs of all sensors from the second test can be found which was used to establish whether particular sensors, from particular motor configurations, had to be ignored due to the values they produced. This could be sensors exceeding their operational range during the test, or otherwise the sensor not returning to a reasonable value. As an example, a pressure sensor that records the pressure within the injector manifold, should return to ambient pressure after a motor test.

B.1. Pressure sensors

Figure B.1 shows all pressure sensor readings collected during the second test. Some abnormalities can be observed, namely during the double anchor CC pressure sensor (figure B.1b) does not return to ambient. This is repeated in figure B.1c. Therefore, this pressure sensor should be treated with some scepticism. Lastly, in figure B.1d, the CC pressure sensor drops to $\{-7.5\ [\text{bar}]\}$ (which is not physically possible), as well as the injector pressure sensor not returning to ambient (it returns to $\{1.5\ [\text{bar}]\}$ while prior to the test it was around $\{0.9\ [\text{bar}]\}$). It can be concluded that these two should not be used in later tests and be replaced.

B.2. Load cells

Figures B.2 and B.3 showcase the load cell sensor readings of the different configurations for the second test. No indications of unusable data.

B.3. Thermocouples

Figures B.4 and B.5 shows the top and bottom temperatures of the run-tank, as well as the temperature of the N_2O prior to the injector manifold. The thermal probe, prior to the injector manifold (shown in figure B.5) does provide an indication, at least for the test with the double hole geometry, as to why the pressure sensors appear non-functional. The readings themselves seem functional.

B.4. Piezoelectric sensors

Figures B.6 to B.8 showcase the piezoelectric sensor measurements taken during the second test day. The readings, while noisy for some sensors and geometries, do not provide an indication of damage, nor that they are not usable for analysis.
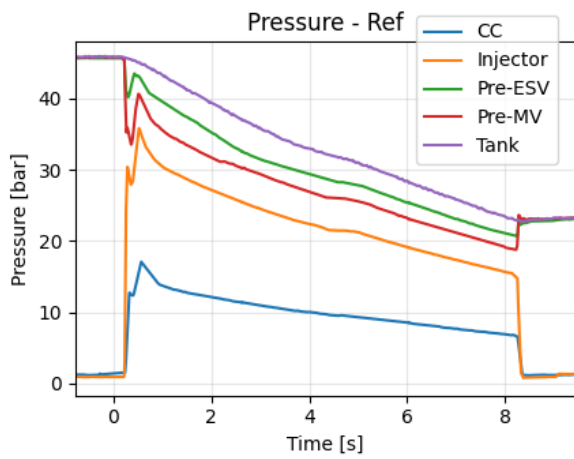
(a) Reference grain geometry
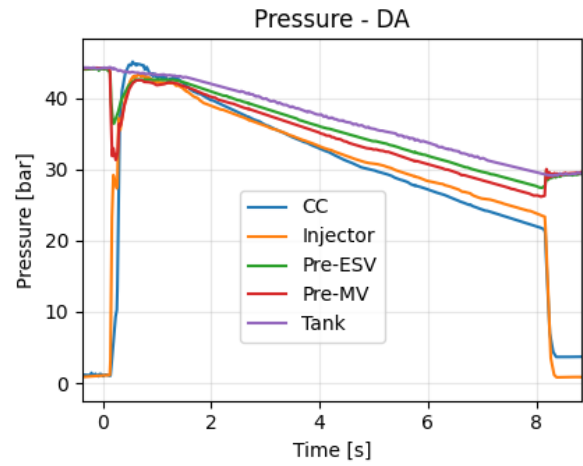
(b) Double anchor grain geometry
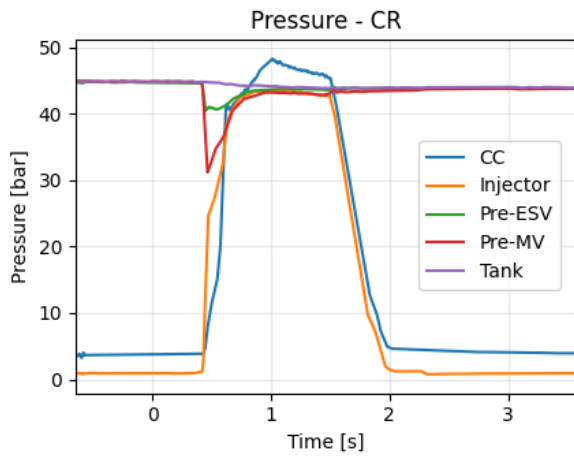
(c) Cross grain geometry
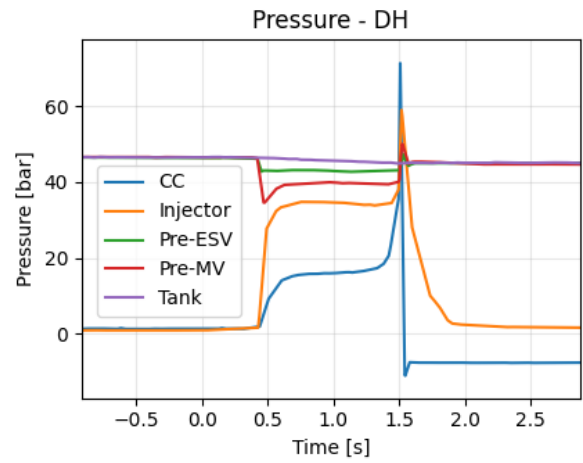
(d) Double hole grain geometry

**Figure B.1:** Pressure sensor data collected on second test day (23 April 2024)
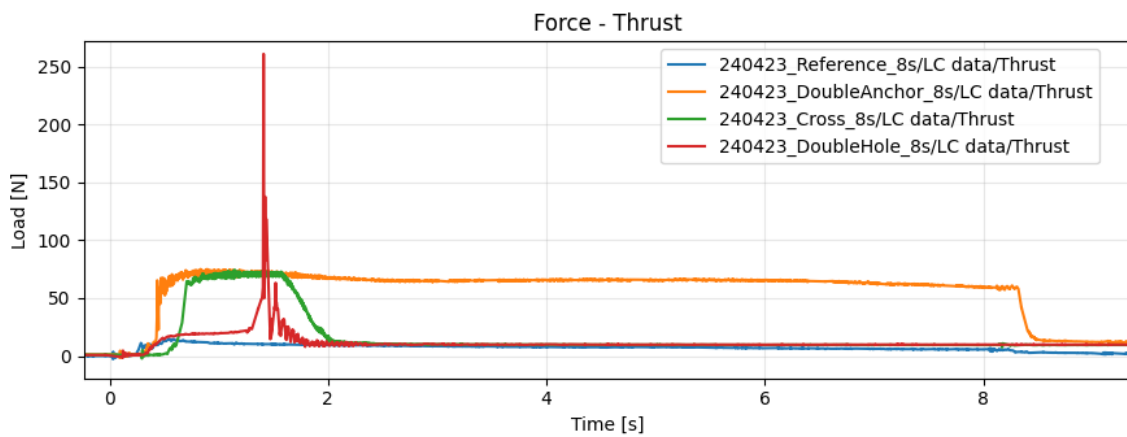
Figure B.2: Thrust data for the second test day (23 April 2024)
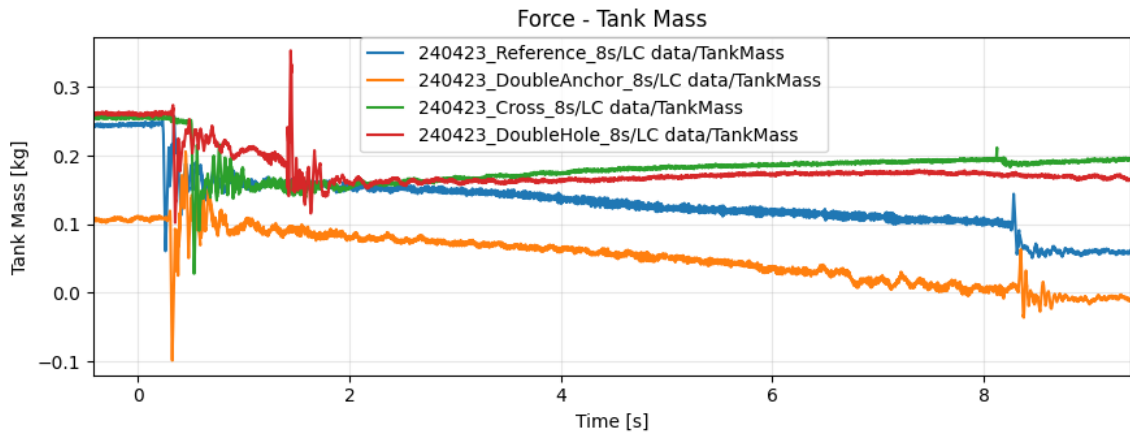
Figure B.3: Tank mass data for second test day (23 April 2024)
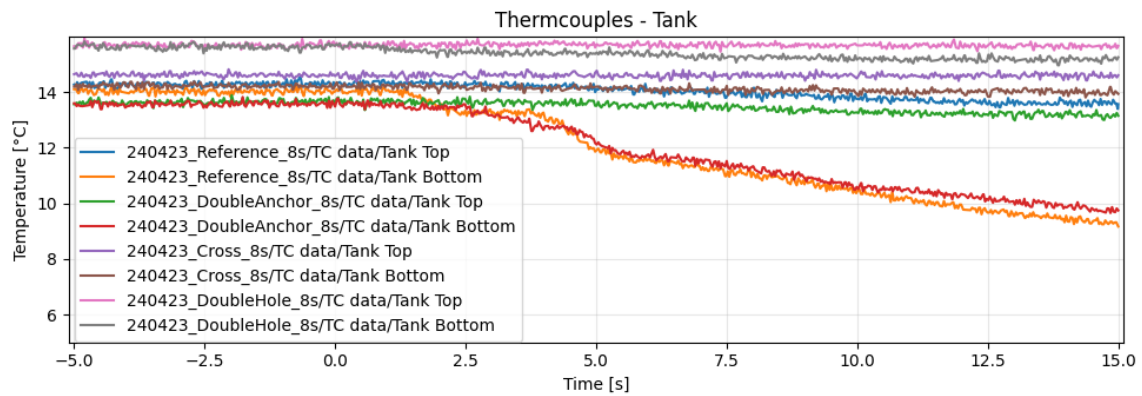
Figure B.4: Thermocouple data for top and bottom of the run-tank (23 April 2024)
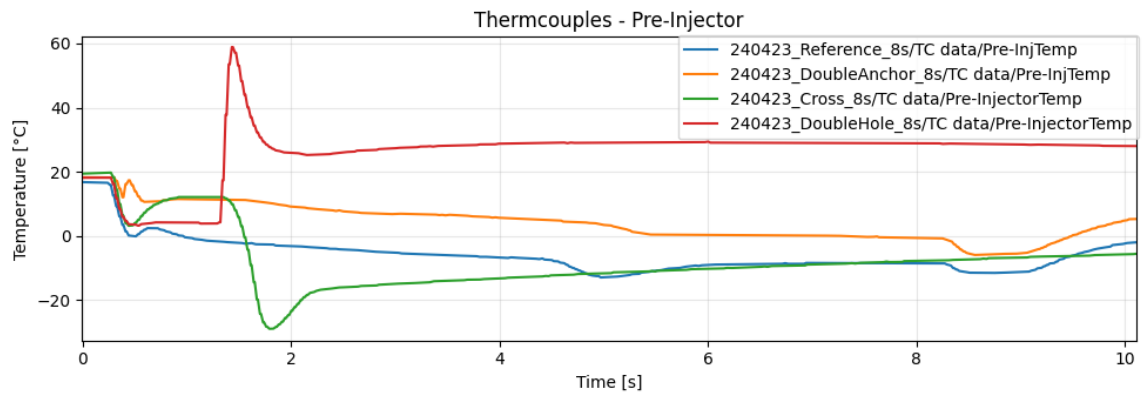
Figure B.5: Thermal probe data pre-injector manifold (23 April 2024)
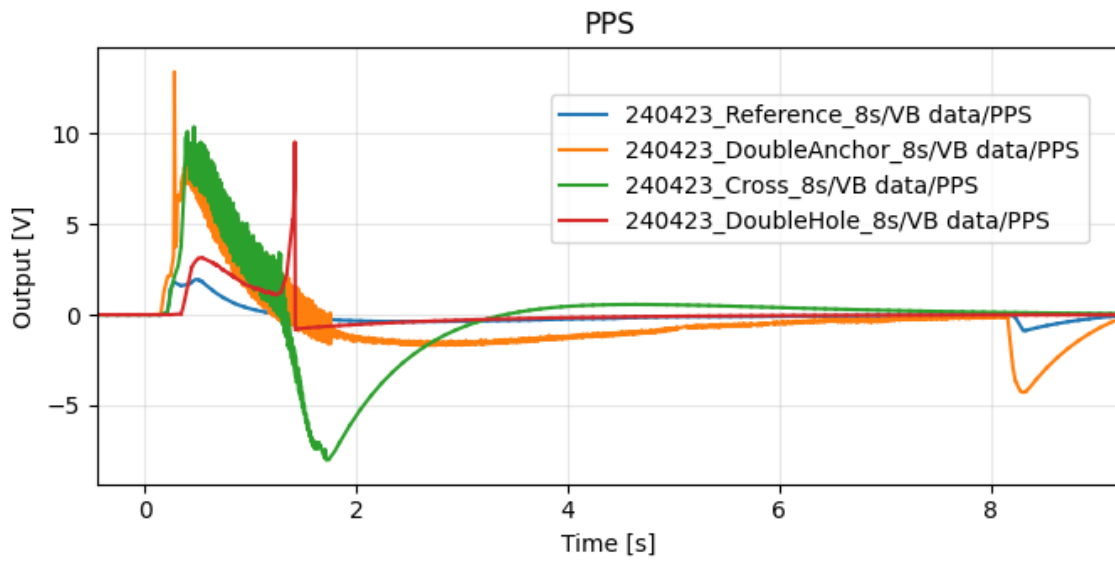
Figure B.6: PPS sensor data for second test day (23 April 2024)
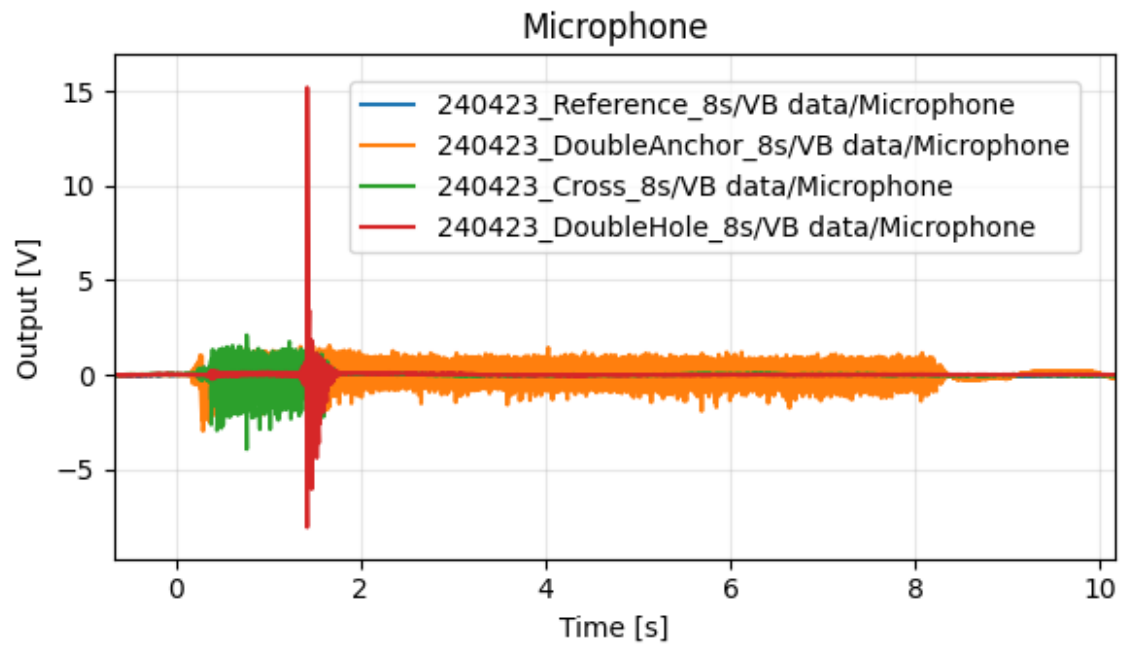
Figure B.7: Microphone sensor data for second test day (23 April 2024)
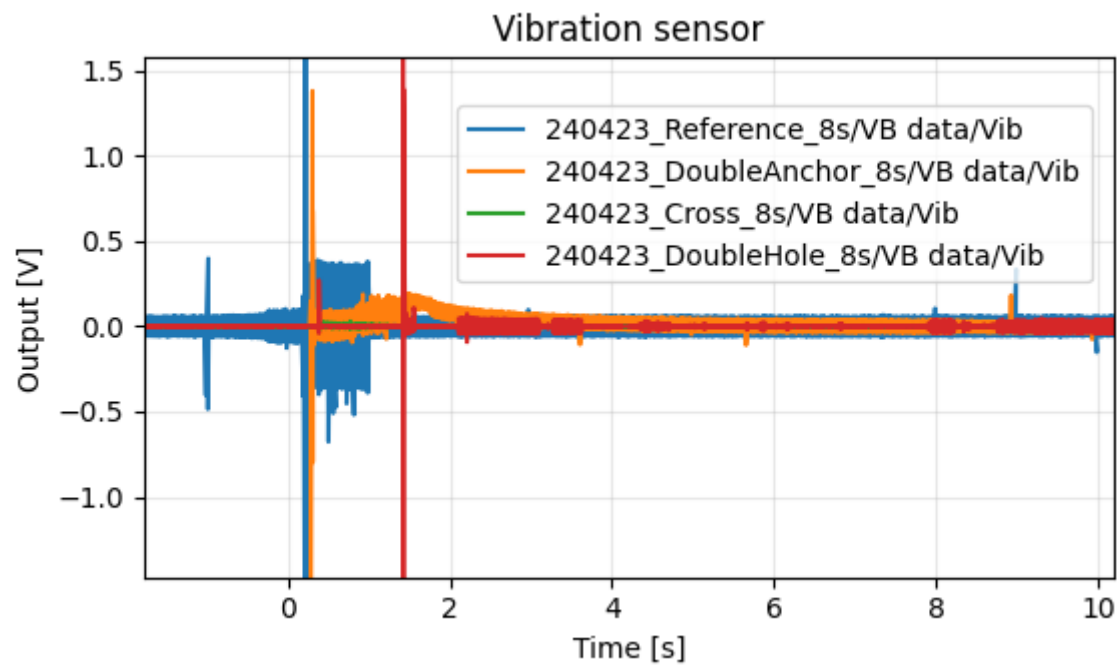
Figure B.8: Vibration sensor data for second test day (23 April 2024)

This page was intentionally left blank

C
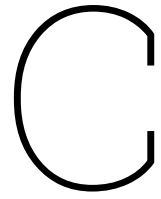
Data Validity - Test 3

In this appendix, all graphs of all sensors from the third (and final) test can be found which was used to establish whether particular sensors, from particular motor configurations, had to be ignored due to the values they produced. This could be sensors exceeding their operational range during the test, or otherwise the sensor not returning to a reasonable value. As an example, a pressure sensor that records the pressure within the injector manifold, should return to ambient pressure after a motor test.

C.1. Pressure sensors

Figure C.1 shows all pressure sensor readings collected during the third test. The only abnormalities are seen in figure C.1d, where both the CC pressure sensor, as well as the injector manifold sensor appear to malfunction (pressure readings indicate pressure is {65 [bar]} and {10 [bar]}, respectively) while the system was at ambient pressure. There is also a spike, indicating abnormal combustion activities (most likely contributing to the anomalous reading). Please note that this data has a Butterworth filter applied.

C.2. Load cells

Figures C.2 and C.3 showcase the load cell sensor readings of the different configurations for the third test. No indications of unusable data.

C.3. Thermocouples

Figures C.4 and C.5 shows the top and bottom temperatures of the run-tank, as well as the temperature of the N_2O prior to the injector manifold. The thermal probe, prior to the injector manifold (shown in figure C.5) does provide an indication, at least for the test with the double hole geometry, as to why the pressure sensors appear non-functional. The readings themselves seem functional.

C.4. Piezoelectric sensors

Figures C.6 to C.8 showcase the piezoelectric sensor measurements taken during the third test day. The PPS sensor (figure C.6) for all tests seem very different compared to previous tests. This sensor will therefore not be used. The microphone (in figure C.7) seems functional. The vibration sensor does provide very different data, especially with respect to the first test. This data is questionable.
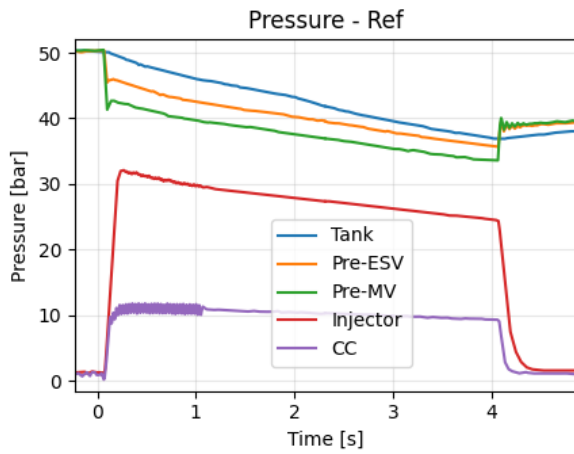
**(a)** Reference grain geometry
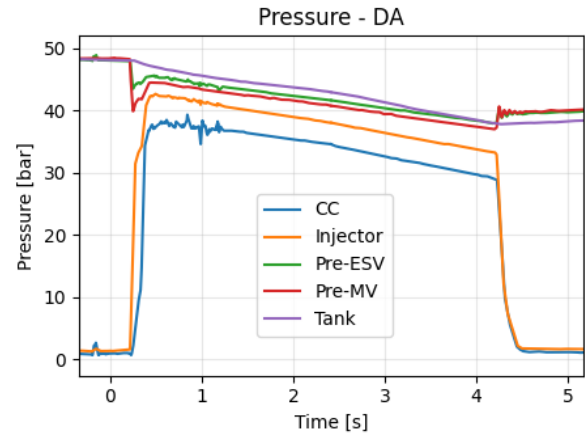
(b) Double anchor grain geometry
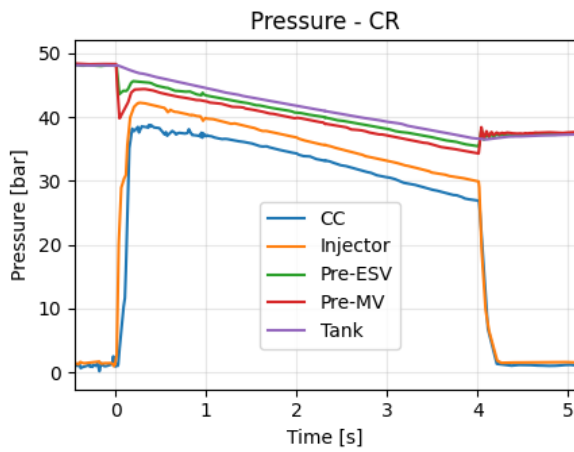
(c) Cross grain geometry
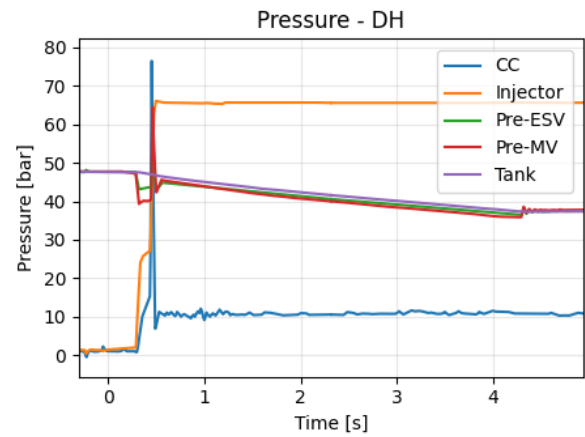
(d) Double hole grain geometry

Figure C.1: Pressure sensor data collected on third test day (7 May 2024)
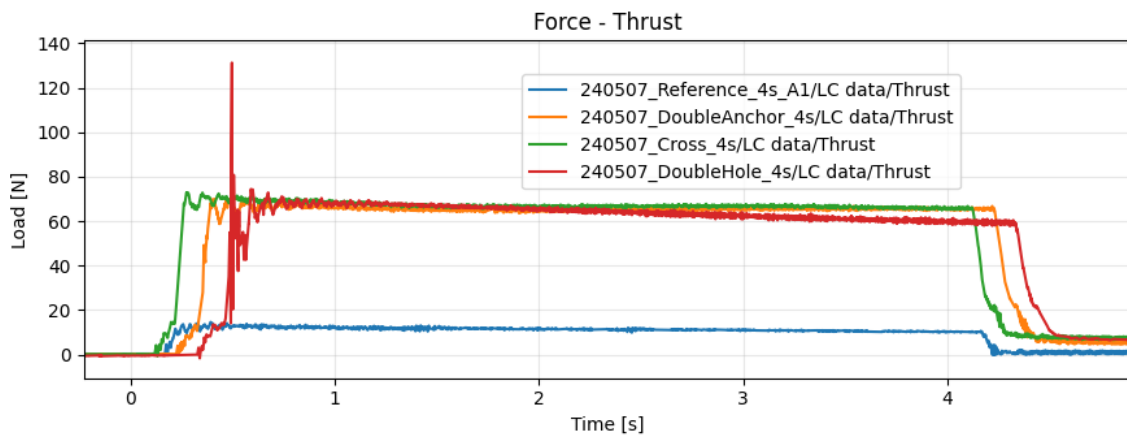
**Figure C.2:** Thrust data for the third test day (7 May 2024)
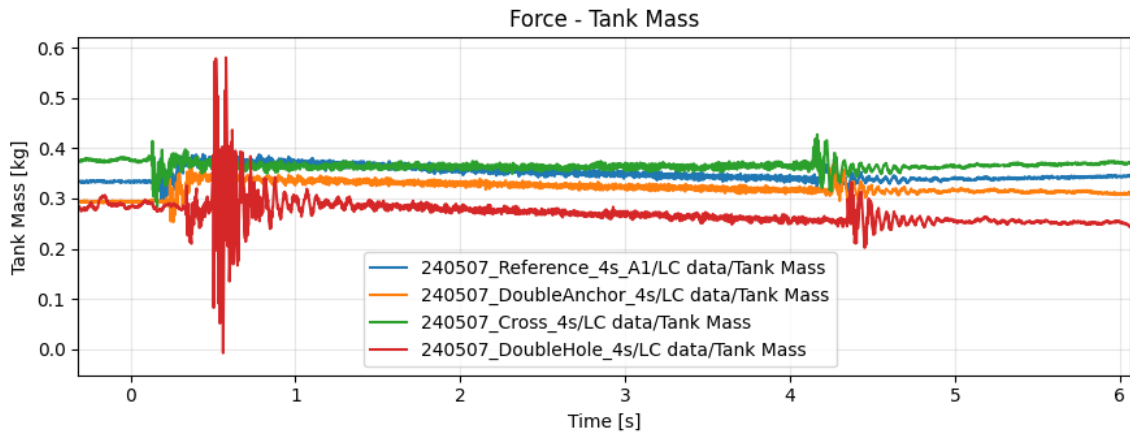
Figure C.3: Tank mass data for third test day (7 May 2024)
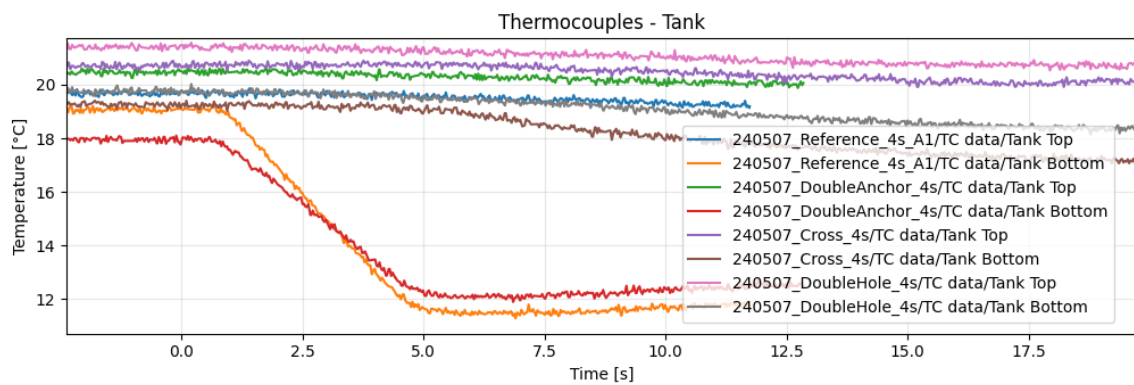
**Figure C.4:** Thermocouple data for top and bottom of the run-tank (7 May 2024)
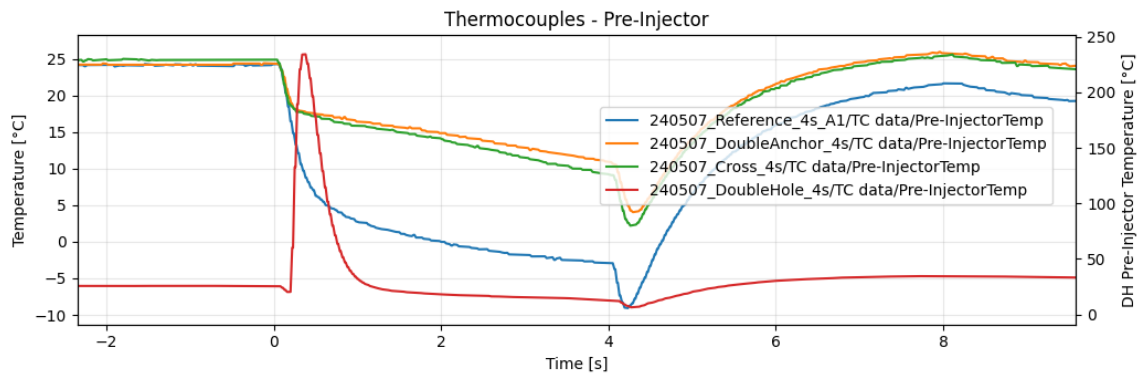
**Figure C.5:** Thermal probe data pre-injector manifold (7 May 2024). The thermal probe data for the double hole test, because of the increased range needed, uses the y-axis on the right side. The reference, double anchor and cross geometry uses the left y-axis.
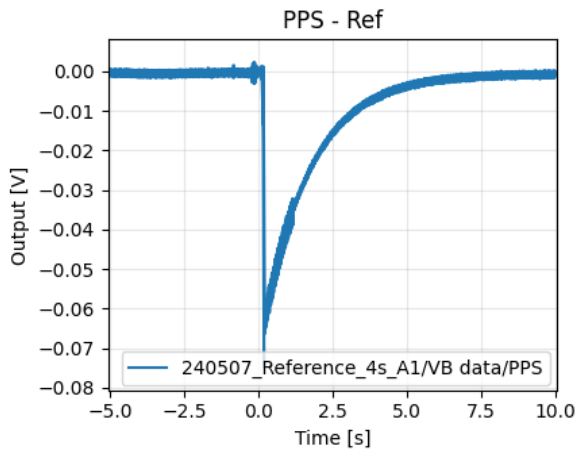
(a) Reference grain geometry
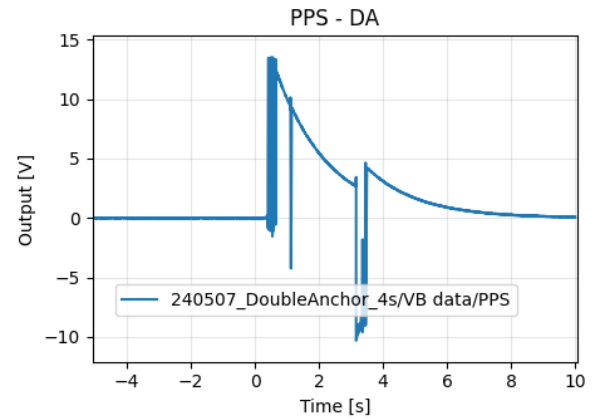
(b) Double anchor grain geometry
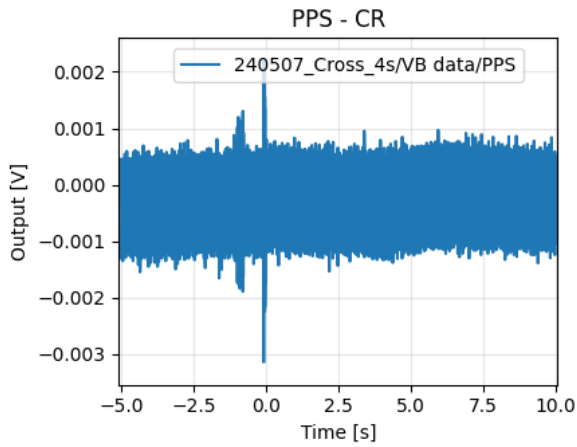
(c) Cross grain geometry
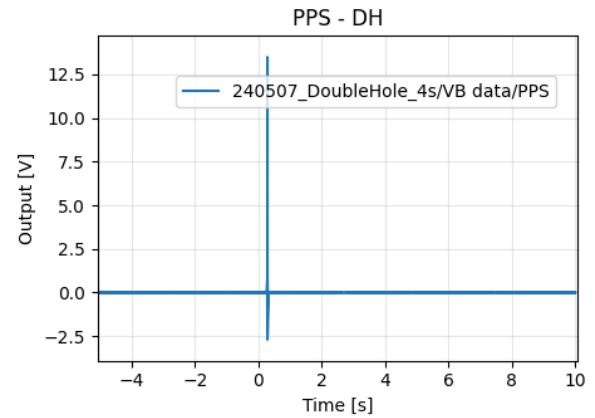
(d) Double hole grain geometry

Figure C.6: PPS sensor data collected on third test day (7 May 2024)
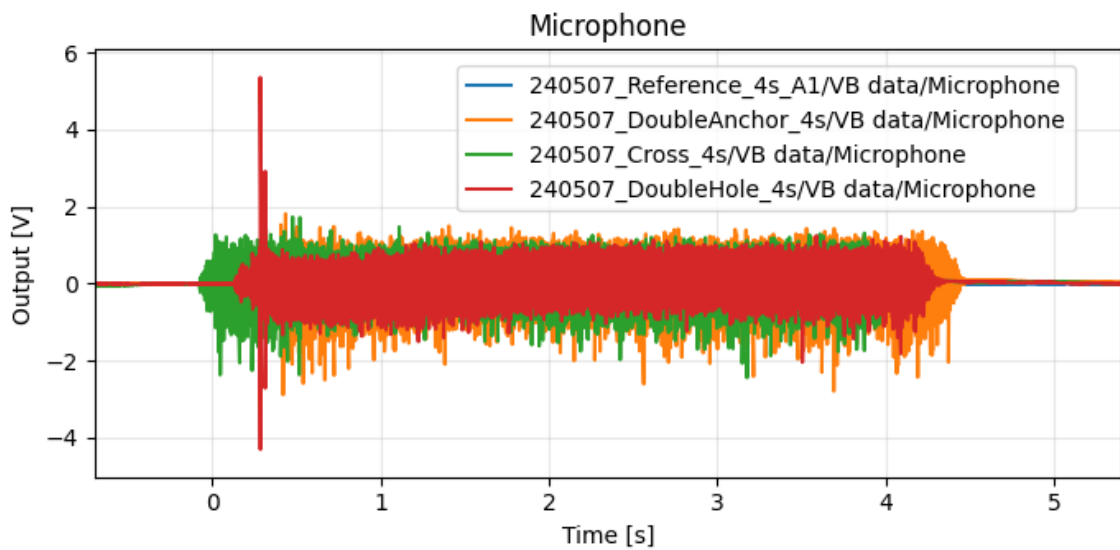
Figure C.7: Microphone sensor data for third test day (7 May 2024)
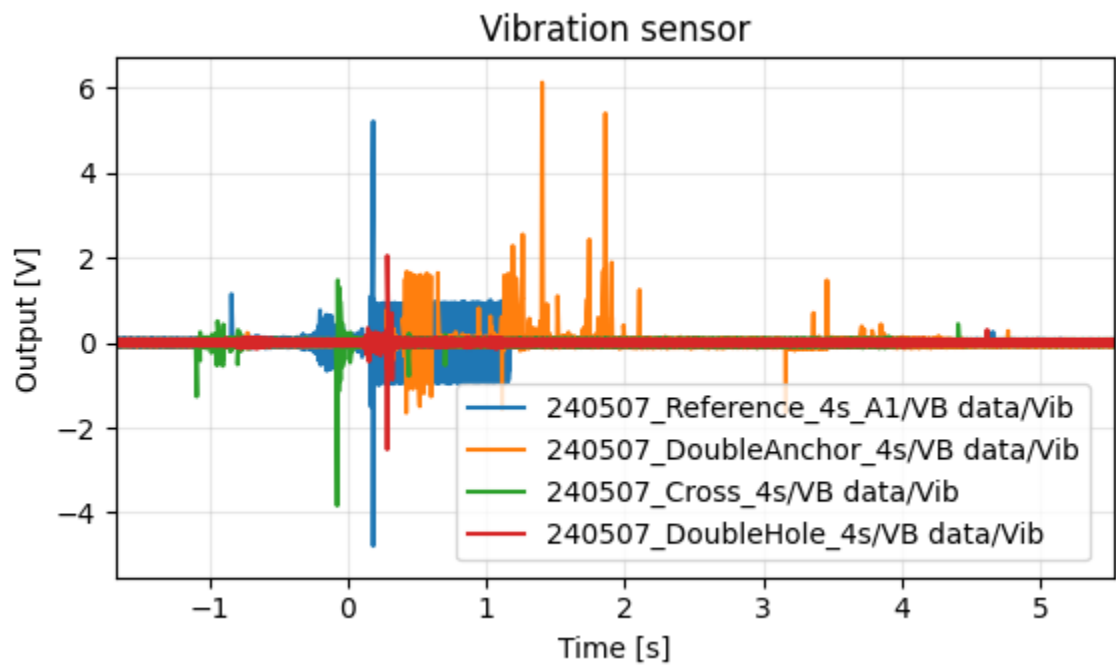
Figure C.8: Vibration sensor data for third test day (7 May 2024)

This page was intentionally left blank

D

Numerical instability for combustion temperature

Figure D.1 shows a numerical instability resulting from a too-large discharge coefficient.
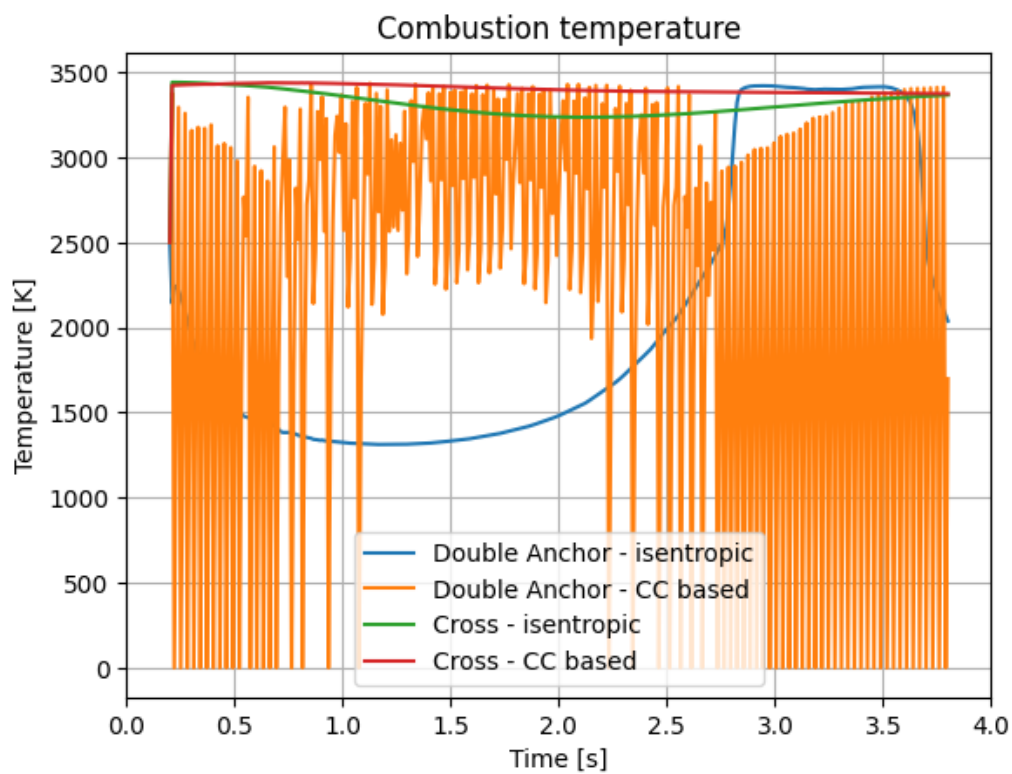
Figure D.1: Numerical instability of combustion temperature due to discharge coefficient

This page was intentionally left blank

E

Verification and Validation data

In this appendix, the individual grain plots from the verification and validation phase (section 6.1) are displayed. The percentage difference can be found in the main report, however the percentage differences come from the following plots.

E.1. Combustion chamber pressure - test 1
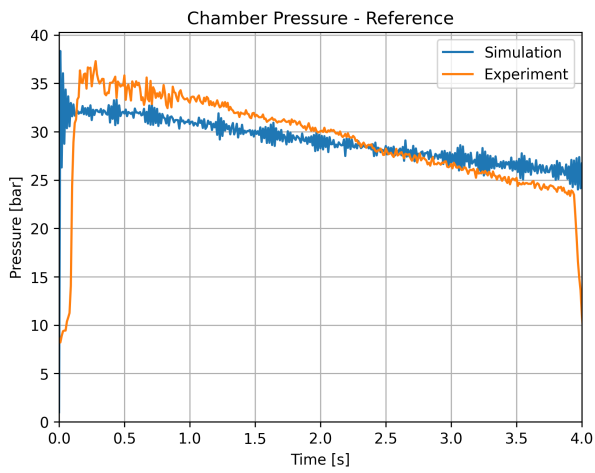
(a) Reference grain CC pressure vs simulation data
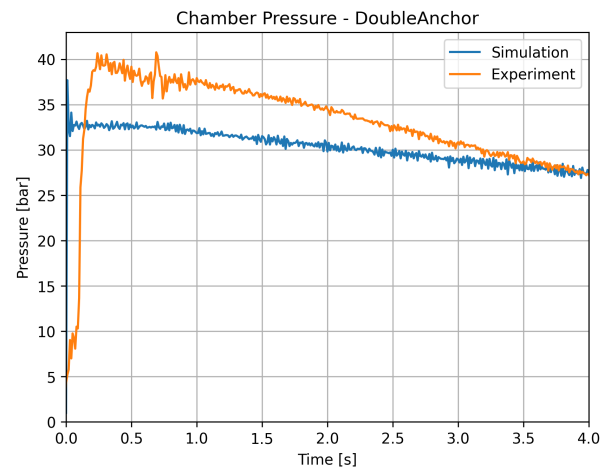
(b) Double anchor grain CC pressure vs simulation data
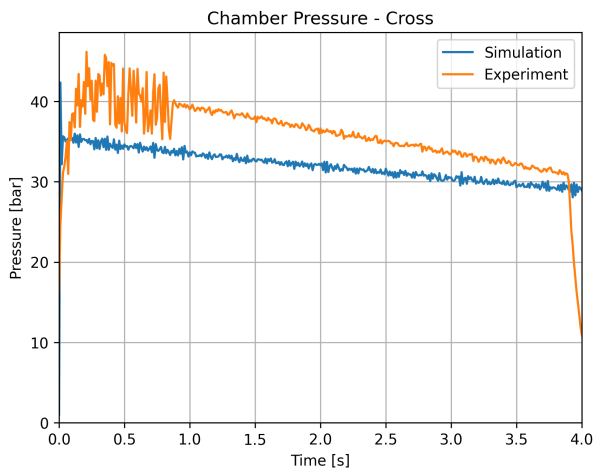
(c) Cross grain CC pressure vs simulation data
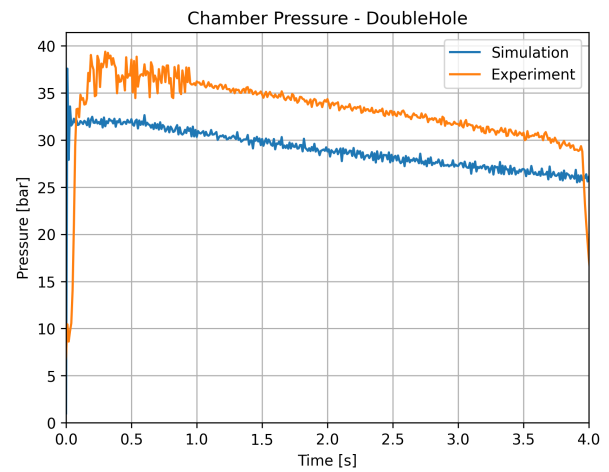
(d) Double hole grain CC pressure vs simulation data

Figure E.1: CC pressure comparison of experimental vs simulation data

E.2. Thrust - test 1
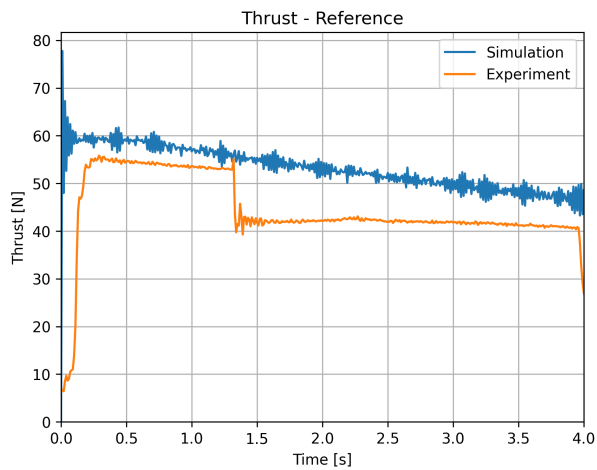
(a) Reference grain thrust vs simulation data
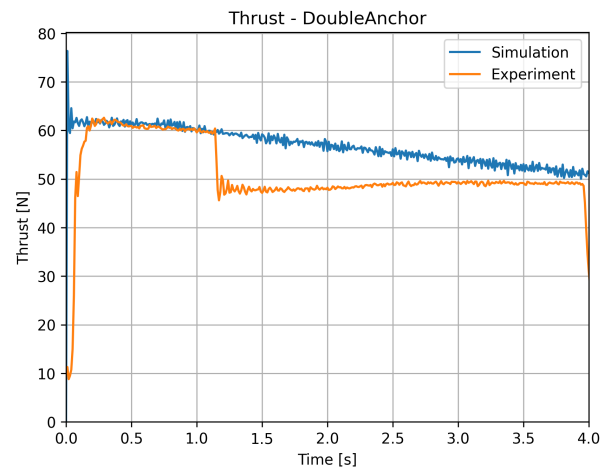
(b) Double anchor grain thrust vs simulation data
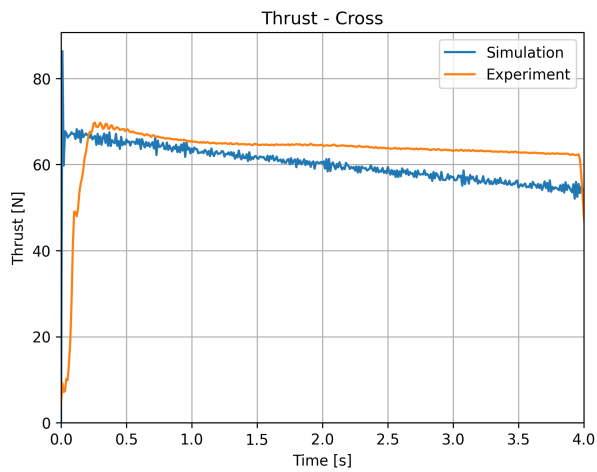
(c) Cross grain thrust vs simulation data
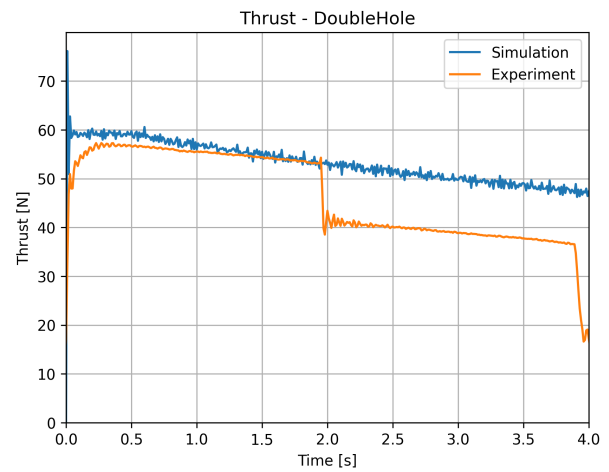
(d) Double hole grain thrust vs simulation data

Figure E.2: Thrust comparison of experimental vs simulation data

E.3. Propellant mass flows - test 3
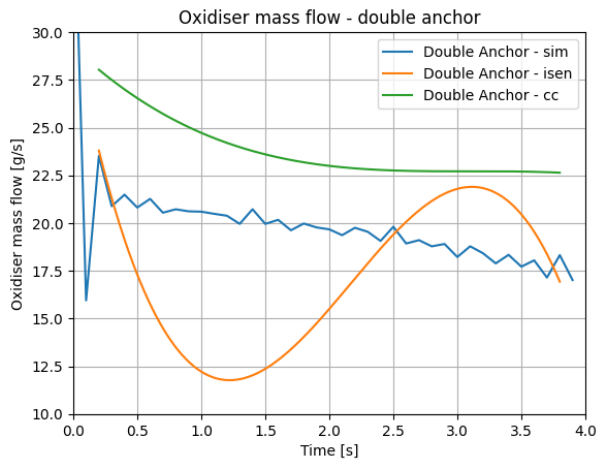
(a) Double anchor oxidiser mass flow with simulation data
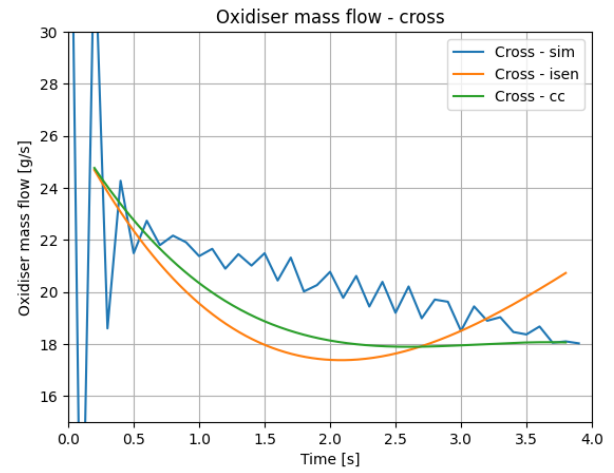
(b) Cross oxidiser mass flow with simulation data
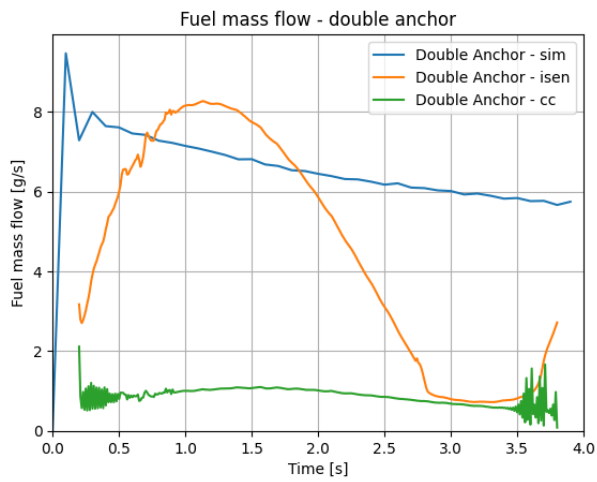
(c) Double anchor fuel mass flow with simulation data
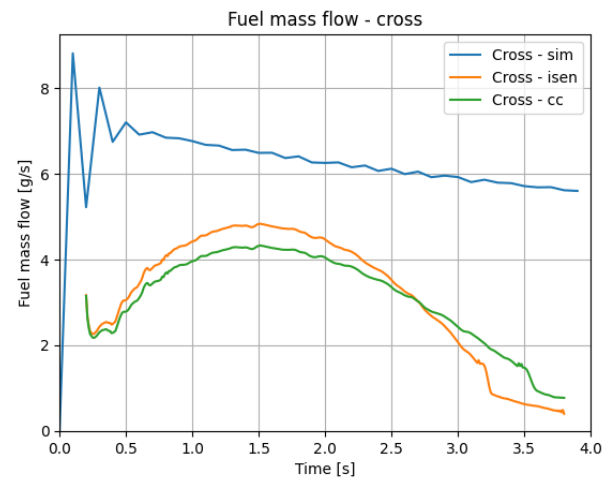
(d) Cross fuel mass flow with simulation data

Figure E.3: Propellant mass flow compared to simulation data

F

Equipment

In this appendix, the various pieces of equipment used are shown - specifically their datasheets (or otherwise).

Appendix F.1 lists the relevant parts of the data sheet for the specific model number of the DAQ system. At the time of writing, the NI website (`https://www.ni.com/docs/en-US/bundle/crio-9035-specs/page/specs.html#d1102e276`) details all information from which the data sheet was gathered.

Appendix F.2 shows the data sheet for the {100 [bar]} variant of the IFM pressure sensors that were used. {60 [bar]} variants were also used, however the data sheet is practically identical (except for the model number of PT5423).

Appendix F.3 shows the data sheet for the piezoelectric pressure sensor. This is followed by appendix F.4 which shows the datasheet for the load cell used to measure thrust. While the data is not used, appendix F.5 concerns the data sheet for the tank load cell which measured the mass of the oxidiser (run-tank). Appendix F.6 is the piezoelectric microphone that was used during testing, while appendix F.7 is the thermal probe used to measure the oxidiser temperature before the injector manifold. Lastly, appendix F.8 is the vibration sensor (officially known as an accelerometer but within this report referred to as a vibration sensor) that was stuck onto the outside of the casing of the HRM used in this thesis.

Appendix F.9 shows the data sheet for the solenoid valve used as a MV in tests 1 and 3.

F.1. cRIO-9035

cRIO-9035 Specifications

This document lists the specifications for the NI cRIO-9035.

In this document, the cRIO-9035 and cRIO-9035 Sync are inclusively referred to as the cRIO-9035.

Definitions

Warranted specifications describe the performance of a model under stated operating conditions and are covered by the model warranty.

Characteristics describe values that are relevant to the use of the model under stated operating conditions but are not covered by the model warranty.

- **Typical** specifications describe the performance met by a majority of models.
- **Nominal** specifications describe an attribute that is based on design, conformance testing, or supplemental testing.

Specifications are **Typical** unless otherwise noted.

Conditions

Specifications are valid for -20 °C to 55 °C unless otherwise noted.

Processor

CPU	Intel Atom E3825
Number of cores	2
CPU frequency	1.33 GHz

© **National Instruments**   **3**

On-die L2 cache	1 MB (shared)

Operating System

> ✎ **Note** For minimum software support information, visit ni.com/info and enter the Info Code swsupport.

> ✎ **Note** LabVIEW FPGA Module is not required when using Scan Interface mode. To program the user-accessible FPGA on the cRIO-9035, LabVIEW FPGA Module is required.

> ✎ **Note** C/C++ Development Tools for NI Linux Real-Time is an optional interface for C/C++ programming of the cRIO-9035 processor. Visit ni.com/info and enter Info Code RIOCdev for more information about the C/C++ Development Tools for NI Linux Real-Time.

cRIO-9035

Supported operating system	NI Linux Real-Time (64-bit)
Application software requirements	
LabVIEW	LabVIEW 2014 SP1 or later, LabVIEW Real-Time Module 2014 SP1 or later, LabVIEW FPGA Module 2014 SP1 or later
C/C++ Development Tools for NI Linux Real-Time	Eclipse Edition 2014 or later
Driver software requirements	NI CompactRIO and Drivers February 2015 or later

cRIO-9035 Sync

Supported operating system	NI Linux Real-Time (64-bit)
Application software requirements	
LabVIEW	LabVIEW 2016 or later, LabVIEW Real-Time Module 2016 or later, LabVIEW FPGA Module 2016 or later
C/C++ Development Tools for NI Linux Real-Time	Eclipse Edition 2016 or later
Driver software requirements	NI CompactRIO and Drivers August 2016 or later

Network/Ethernet Port

Number of ports	2
Network interface	10Base-T, 100Base-TX, and 1000Base-T Ethernet
Compatibility	IEEE 802.3
Communication rates	10 Mb/s, 100 Mb/s, 1,000 Mb/s auto-negotiated
Maximum cabling distance	100 m/segment

RS-232 Serial Port

Maximum baud rate	115,200 b/s
Data bits	5, 6, 7, 8

Memory

Nonvolatile[1]	
SD removable (user supplied)	Up to 32 GB
Solid-state drive	4 GB

> ✏️ **Note** Visit ni.com/info and enter the Info Code ssdbp for information about the life span of the nonvolatile memory and about best practices for using nonvolatile memory.

Volatile	
Processor memory	
Density	1 GB
Type	DDR3L
Maximum theoretical data rate	8.533 GB/s
Data throughput	
System memory to SD removable storage[2]	10 MB/s
Module slots to system memory	20 MB/s, application- and system-dependent

Reconfigurable FPGA

FPGA type	Xilinx Kintex-7 7K70T

---

[1] 1 MB is equal to 1 million bytes. 1 GB is equal to 1 billion bytes. The actual formatted capacity might be less.

[2] Consult the manufacturer specifications of your SD removable storage.

Number of flip-flops	82,000
Number of 6-input LUTs	41,000
Number of DSP slices (18 × 25 multipliers)	240
Available block RAM	4,860 kbits
Number of DMA channels	16
Number of logical interrupts	32

Internal Real-Time Clock

Accuracy	200 ppm; 40 ppm at 25 °C

CMOS Battery

Typical battery life with power applied to power connector	10 years
Typical battery life when stored at temperatures up to 25 °C	7.8 years
Typical battery life when stored at temperatures up to 85 °C	5.4 years

F.2. IFM Pressure Sensors (100 bar variant - PT5402)
PT5402

Pressure transmitter

PT-100-SEG14-A-ZVG/US/   /W
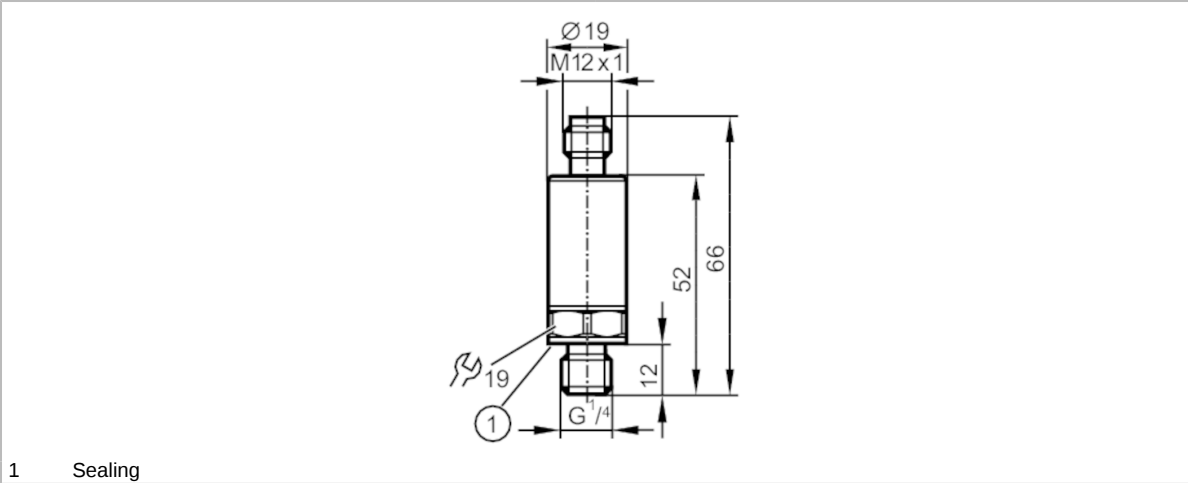
1   Sealing

Product characteristics			
Number of inputs and outputs	Number of analogue outputs: 1		
Measuring range	0...100 bar	0...1450 psi	0...10 MPa
Process connection	threaded connection G 1/4 external thread (DIN EN ISO 1179-2)		
Application			
Application	for industrial applications		
Media	liquids and gases		
Medium temperature [°C]	-40...90		
Min. bursting pressure	1000 bar	14500 psi	100 MPa
Pressure rating	250 bar	3625 psi	25 MPa
Note on pressure rating	static		
Vacuum resistance [mbar]	-1000		
Type of pressure	relative pressure		
Electrical data			
Operating voltage [V]	8.5...36 DC		
Min. insulation resistance [MΩ]	100; (500 V DC)		
Protection class	III		
Reverse polarity protection	yes		
Power-on delay time [s]	< 0.1		
Inputs / outputs			
Number of inputs and outputs	Number of analogue outputs: 1		
Outputs			
Total number of outputs	1		
Output signal	analogue signal		
Number of analogue outputs	1		
Analogue current output [mA]	4...20		
Max. load [Ω]	(Ub – 8,5 V) / 21,5 mA; @8,5V= 0 Ω; @12V max. 160 Ω; @24V max. 720 Ω		

PT5402

Pressure transmitter

PT-100-SEG14-A-ZVG/US/   /W

Short-circuit proof	yes		
Overload protection	yes		
Measuring/setting range			
Measuring range	0...100 bar	0...1450 psi	0...10 MPa
Accuracy / deviations			
Repeatability [% of the span]	< ± 0,05; (with temperature fluctuations < 10 K)		
Characteristics deviation [% of the span]	< ± 0,5; (incl. drift when overtightened, zero point and span error, non-linearity, hysteresis)		
Linearity deviation [% of the span]	< ± 0,1 (BFSL) / < ± 0,2 (LS)		
Hysteresis deviation [% of the span]	< ± 0,2		
Long-term stability [% of the span]	< ± 0,1; (per 6 months)		
Temperature coefficient zero point and span [% of the span / 10 K]	< 0,1 (-25...90 °C) / < 0,2 (-40...-25 °C)		
Response times			
Step response time analogue [ms] output	1		
Operating conditions			
Ambient temperature [°C]	-40...90		
Storage temperature [°C]	-40...100		
Protection	IP 67; IP 69K		
Tests / approvals			
EMC	DIN EN 61000-6-2		
	DIN EN 61000-6-3		
Shock resistance	DIN EN 60068-2-27	50 g (11 ms)	
Vibration resistance	DIN EN 60068-2-6	20 g (10...2000 Hz)	
MTTF [years]	686		
Pressure Equipment Directive	Sound engineering practice; can be used for group 2 fluids; group 1 fluids on request		
Mechanical data			
Weight [g]	59		
Materials	stainless steel (630/1.4542/17-4 PH); stainless steel (316L/1.4404); PEI		
Materials (wetted parts)	stainless steel (630/1.4542/17-4 PH)		
Min. pressure cycles	60 million; (at 1.2 times nominal pressure)		
Tightening torque [Nm]	25...35; (recommended tightening torque; depends on lubrication, seal and pressure rating)		
Process connection	threaded connection G 1/4 external thread (DIN EN ISO 1179-2)		
Process connection sealing	FKM (DIN EN ISO 1179-2)		
Restrictor element integrated	no (can be retrofitted)		
Remarks			
Remarks	BFSL = Best Fit Straight Line		
	LS = limit value setting		
Pack quantity	1 pcs.		

PT5402

Pressure transmitter

PT-100-SEG14-A-ZVG/US/   /W

Electrical connection

Connector: 1 x M12; coding: A

Connection
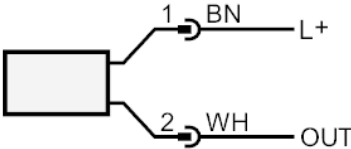
OUT	analogue output
	The following pin connection is available under article number PT53xx Pin 1: L+, Pin 3: OUT
	colours to DIN EN 60947-5-2
	Core colours :
BN	brown
WH	white

F.3. PPS

Outline drawing — Model 124A21, A22, A24 Water Cooled Sensor, Drawing No. 124-1210-90.

APPLICATION			REVISIONS				
NEXT ASS'Y	USED ON	VAR	REV	DESCRIPTION	ECN	DATE	APP'D
			D	REVISED PER ECR	20202	7/14/04	DM 7/04

124-1210-90

PCB Piezotronics Inc. claims proprietary rights in the information disclosed hereon. Neither it nor any reproduction thereof will be disclosed to others without written consent of PCB Piezotronics Inc.

.800(20.32)

1.00(25.4) HEX △1

ELECTRICAL CONNECTOR CO-AXIAL 10-32 UNF-2A

MODEL 006EB004EB ARMORED CABLE 4 FT(1.2M) LG. (SUPPLIED)

WATER INLET TUBES ∅.109 I.D. 5/16-24 UNF-3A (REF:M$33656E2)

SENSOR

MODEL 065A09 SEAL .56 O.D. X .06 THK. (SUPPLIED)

1/2-20 UNF-2A

ROKIDE COATING

2.06(52.3)
1.78(45.2)
.04(1.0)
.985(25.0)
.63(16.0)

MOUNTING HOLE PREPARATION:
∅.453
THRU
1/2-20 UNF-2B
THRU
⌴∅.562
X .050 ▽ △2

.63(16.0)

△2 SEAL SURFACE MUST BE FLAT AND FREE OF TOOL MARKS WITH AT LEAST ⁶³∕ FINISH.

△1 MOUNTING TORQUE ON 1.00 HEX 10-15 FT. LBS.

UNLESS SPECIFIED TOLERANCES		DRAWN	EB	7/14/04	MFG	KL6	7/16/04	⊕PCB PIEZOTRONICS™
DIMENSIONS IN INCHES	DIMENSIONS IN MILLIMETERS [IN BRACKETS]	CHK'D	BM	7/14/04	ENGR	BV	7/14/04	3425 WALDEN AVE. DEPEW, NY 14043 (716) 684-0001 EMAIL: SALES@PCB.COM
DECIMALS XX ±.03 XXX ±.010	DECIMALS X ±0.8 XX ±0.25	APP'D	RF	7/16/04	SALES	DPC	7/16/04	
ANGLES ±2 DEGREES	ANGLES ±2 DEGREES	TITLE						CODE IDENT. NO. 52681	DWG. NO. 124-1210-90
FILLETS AND RADII .003 - .005	FILLETS AND RADII [0.07 - 0.13]		OUTLINE DRAWING MODEL 124A21, A22, A24 WATER COOLED SENSOR					
DD011 REV. C 01/21/03							SCALE: 1.33X	SHEET 1 OF 1

Model Number 124A21			Revision: K ECN #: 51279

Performance

	ENGLISH	SI	
Measurement Range(for ±5V output)	250 psi	1,724 kPa	
Useful Overrange(for ±7V output)	350 psi	3,448 kPa	
Sensitivity(± 15 %)	20 mV/psi	2.90 mV/kPa	
Maximum Pressure	5,000 psi	34,475 kPa	
Resolution	0.005 psi	0.034 kPa	[1]
Resonant Frequency	≥ 15 kHz	≥ 15 kHz	
Rise Time(Reflected)	≤ 30 μ sec	≤ 30 μ sec	
Low Frequency Response(- 5 %)	0.50 Hz	0.50 Hz	
Non-Linearity	≤ 1.0 % FS	≤ 1.0 % FS	[2]

Environmental

Acceleration Sensitivity	≤ 0.002 psi/g	≤ 0.0014 kPa/(m/s^2)	
Temperature Range(Operating)	-100 to +250 °F	-73 to +121 °C	[3]
Temperature Coefficient of Sensitivity	≤ 0.03 %/°F	≤ 0.054 %/°C	
Maximum Flash Temperature	5,000 °F	2,670 °C	
Maximum Vibration	2,000 g pk	19,600 m/s^2 pk	
Maximum Shock	10,000 g pk	98,070 m/s^2 pk	

Electrical

Output Polarity(Positive Pressure)	Positive	Positive	
Discharge Time Constant(at room temp)	≥ 1.0 sec	≥ 1.0 sec	
Excitation Voltage	20 to 30 VDC	20 to 30 VDC	
Constant Current Excitation	2 to 20 mA	2 to 20 mA	
Output Impedance	≤ 100 Ohm	≤ 100 Ohm	
Output Bias Voltage	8 to 14 VDC	8 to 14 VDC	
Electrical Isolation	10^8 Ohm	10^8 Ohm	

Physical

Sensing Geometry	Compression	Compression	
Sensing Element	Quartz	Quartz	
Housing Material	Stainless Steel	Stainless Steel	
Diaphragm	Invar	Invar	
Sealing	Welded Hermetic	Welded Hermetic	
Electrical Connector	10-32 Coaxial Jack	10-32 Coaxial Jack	
Weight	3.9 oz	110 gm	
Cable Type	006 Ruggedized Low Noise	006 Ruggedized Low Noise	
Cable Length	4.0 ft	1.3 m	
Water Flow Rate(at 50 psi)	1.2 gal/min	1.2 gal/min	

OPTIONAL VERSIONS

Optional versions have identical specifications and accessories as listed for the standard model except where noted below. More than one option may be used.

M - Metric Mount
Supplied Accessory: Model 065A16 Seal ring 0.624" OD x 0.553" ID x 0.060" thk brass replaces Model 065A09

N - Negative Output Polarity

S - Stainless Steel Diaphragm

Diaphragm	316L Stainless Steel	316L Stainless Steel

NOTES:
[1]Typical.
[2]Zero-based, least-squares, straight line method.
[3]Refers to operating temperature of the internal sensor without cooling.
[4]See PCB Declaration of Conformance PS023 for details.

SUPPLIED ACCESSORIES:
Model 065A09 Seal ring 0.560" OD x 0.500" ID x 0.060" thk brass (3)
Model 070A08 Cable adaptor (micro 10-32 jack to BNC jack) (1)

CE [4]

Entered: LK	Engineer: NJL	Sales: MV	Approved: RPF	Spec Number:
Date: 12/23/2020	Date: 12/23/2020	Date: 12/23/2020	Date: 12/23/2020	124-1210-80

PCB PIEZOTRONICS
3425 Walden Avenue, Depew, NY 14043
Phone: 716-684-0001
Fax: 716-684-0987
E-Mail: info@pcb.com

All specifications are at room temperature unless otherwise specified.
In the interest of constant product improvement, we reserve the right to change specifications without notice.
ICP® is a registered trademark of PCB Piezotronics, Inc.

F.4. Thrust Load Cell (FSH04532)

FUTEK
ADVANCED SENSOR TECHNOLOGY, INC.

MODEL LCM300
Miniature Threaded In Line Load Cell

FEATURES

- Minimal mounting clearance
- 17-4 PH stainless-steel construction
- For use in both tension and compression
- Utilizes metal foil strain gauge technology
- Environmental Protection, IP67 Rated
- Fast Response time
- Water Resistant and Outdoor Rated

Non-loading surface, do not contact

Active End

Fixed End

+ Output (tension)

− Output (compression)
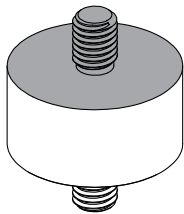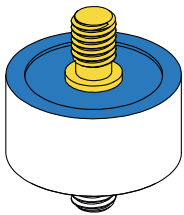
SPECIFICATIONS	
PERFORMANCE	
Nonlinearity	±0.25% of RO
Hysteresis	±0.25% of RO
Nonrepeatability	±0.1% of RO
ELECTRICAL	
Rated Output (RO)	2 mV/V nom
Excitation (VDC or VAC)	15 max
Bridge Resistance	740 Ohm nom
Insulation Resistance	≥500 MOhm @ 50 VDC
Connection	4 Position Micro Receptacle
Wiring/Connector Code	CC19
MECHANICAL	
Weight	1.5 oz [42.5 g]
Safe Overload	150% of RO
Deflection	See chart on next page
Material (flexure)	17-4 PH stainless-steel
IP Rating	IP67
TEMPERATURE	
Operating Temperature	–60 to 200°F (–50 to 93°C)
Compensated Temperature	60 to 160°F (15 to 72°C)
Temperature Shift Zero	±0.005% of RO/°F (±0.01 of RO/°C)
Temperature Shift Span	±0.02% of load/°F (±0.036 of load/°C)
CALIBRATION	
Calibration Test Excitation	10 VDC
Calibration (standard)	5-pt Tension
Calibration (available)	Compression
Shunt Calibration Value	100 kOhm
CONFORMITY	
RoHS	EU 2015/863
CE	EN55011; EN61326-1

Sensor Solution Source
Load · Torque · Pressure · Multi-Axis · Calibration · Instruments · Software

www.futek.com

CE   RoHS   ANSI Z540-1   ISO 17025   ISO 9001   ISO 13485   U.S. Manufacturer

Model LCM300

2

DIMENSIONS inches [mm]

TOLERANCE:
.X ± 0.1" [2.5 mm]
.XX ± 0.01" [0.25 mm]
.XXX ± 0.005" [0.127 mm]

Ø 0.98 [Ø 24.9]

0.32 [8.1]

0.02 [0.5]

4 POSITION MICRO CIRCULAR
(KEY ORIENTATION VARIES)

1.21 [30.7]

0.50 [12.7]

0.29 [7.4]

0.33 [8.4]

2X M6x1 - 6g
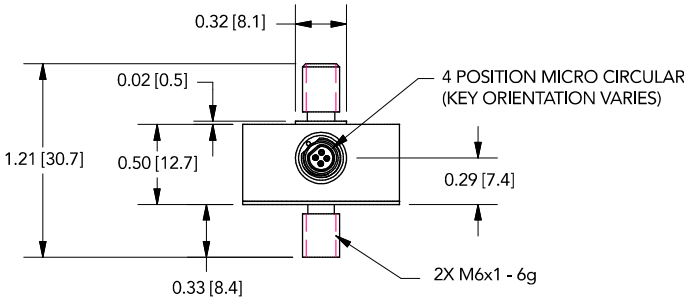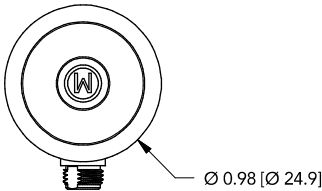
FUTEK 4 PIN MICRO CIRCULAR (CC19)

1	+ EXCITATION	Red
2	– EXCITATION	Black
3	– SIGNAL	White
4	+ SIGNAL	Green

CAPACITIES				
ITEM #	lb	N	Deflection (in)	Natural Frequency (kHz)
FSH04530	50	223	0.002	6.1
FSH04531	100	445	0.001	10.9
FSH04532	250	1112	0.001	17
FSH04533	500	2224	0.001	23
FSH04534	1000	4448	0.001	29

Drawing Number: FI1534

FUTEK reserves the right to modify its design and specifications without notice.
Please visit http://www.futek.com/salesterms for complete terms and conditions.

10 Thomas, Irvine, CA 92618 USA
Tel: (949) 465-0900

www.futek.com

CE   RoHS   ANSI Z540-1   ISO 17025   ISO 9001   ISO 13485   U.S. Manufacturer

F.5. Tank Load Cell (25kg variant)

VPGTransducers

Celtron • Revere • Sensortronics • Tedea-Huntleigh

Model STC

Celtron

S-Type Load Cell

SPECIFICATIONS			
PARAMETER	**VALUE**		**UNIT**
NTEP/OIML accuracy class	NTEP III & IIIL	Non-Approved	
Maximum no. of intervals (n)	III 5000 single* IIIL10000 single*	2000	
Y = E_{max}/V_{min}	10000	5000	Maximum available
Standard capacities (E_{max}) (Aluminum)	5, 10, 20		kg
Standard capacities (E_{max}) (Steel)	25, 50, 75, 100, 250, 500, 750, 1000, 1500, 2000, 2500, 5000		kg
	250, 300, 500, 750, 1k, 1.5k, 2k, 2.5k, 3k, 5k, 7.5k, 10k, 15k, 20k, 40k		lbs
Rated output—R.O. (Aluminum)	2.0		mV/V
Rated output—R.O. (Steel)	3.0		mV/V
Rated output tolerance	0.25		±% of rated output
Zero balance	1		±% of rated output
Non-linearity	0.020	0.020 (SS: 0.05)	±% of rated output
Hysteresis	0.020	0.020 (SS: 0.05)	±% of rated output
Non-repeatability	0.020		±% of rated output
Creep error (20 minutes)	0.030		±% of rated output
Zero return (20 minutes)	0.030		±% of rated output
Temperature effect on min. dead load output	0.0015	0.0026	±% of rated output/°C
Temperature effect on sensitivity	0.0010	0.0015	±% of applied load/°C
Compensated temperature range	−10 to +40		°C
Operating temperature range	−20 to +60		°C
Safe overload	150		% of R.C.
Ultimate overload	200 (Aluminum) / 300 (Steel)		% of R.C.
Excitation, recommended	10		VDC or VAC RMS
Excitation, maximum	15		VDC or VAC RMS
Input impedance	410±5 (Aluminum) / 385±5 (Steel)		Ω
Output impedance	350±3		Ω
Insulation resistance	>5000		MΩ
Construction	Aluminium or Nickel-plated alloy steel **		
Environmental protection	IP67		

*   Capacities 250–20k lbs
** Stainless steel available
All specifications subject to change without notice.

FM Approval
   Intrinsically Safe: Class I, II, III; Div. 1 Groups A-G
   Non-Incendive: Class I; Div. 2 Groups A-D

F.6. Microphone

22929

REVISIONS		
REV	DESCRIPTION	DIN
B	UPDATED [15.88] WAS [5.88]	44838

ELECTRICAL CONNECTOR
CO-AXIAL 10-32 UNF-2A

2.01 [51.1]

MODEL 060A11 2
CLAMP NUT
MAT'L DELRIN
.750 [19.05] HEX

3/4-16 UNF-2A

$\varnothing.686 \begin{smallmatrix}+.000 \\ -.001\end{smallmatrix} \left[17.42 \begin{smallmatrix}+.00 \\ -.03\end{smallmatrix}\right]$

MODEL 065A36
SEAL .060[1.52] THK
MAT'L DELRIN
.700[17.78] O.D.

$\varnothing.618 \begin{smallmatrix}+.000 \\ -.001\end{smallmatrix} \left[15.70 \begin{smallmatrix}+.00 \\ -.03\end{smallmatrix}\right]$

MOUNTING HOLE PREPARATION

$\varnothing.625$ [15.88] THRU
$\sqcup\varnothing.703$ [17.86] ⩒ .460 [11.68]
3/4-16 UNF-2B ⩒ .28 [7.1]

1 .700 [17.78]

2 RECOMMENDED MOUNTING TORQUE ON 3/4 HEX 3-5 FT LBS [.415-.691 Kg-m]

1 DIMENSIONS SHOWN ARE FOR .700 [17.78] THICK WALL. COUNTERBORE THICKER WALLS.

UNLESS OTHERWISE SPECIFIED TOLERANCES ARE:		DRAWN		CHECKED		ENGINEER		**PCB PIEZOTRONICS**
DIMENSIONS IN INCHES	DIMENSIONS IN MILLIMETERS [IN BRACKETS]	BB	12/2/15	ECB	12/2/15	BAM	12/2/15	3425 WALDEN AVE. DEPEW, NY 14043 (716) 684-0001 E-MAIL: sales@pcb.com
DECIMALS XX ±.01 XXX ±.005	DECIMALS X ± 0.3 XX ± 0.13	TITLE INSTALLATION DRAWING MODEL 106B52 OFF-GROUND PRESSURE SENSOR						
ANGLES ± 2 DEGREES	ANGLES ± 2 DEGREES							CODE IDENT. NO. 52681 / DWG. NO. 22929
FILLETS AND RADII .003 - .005	FILLETS AND RADII 0.07 - 0.13							SCALE: 2X SHEET 1 OF 1

Model Number		**ICP® PRESSURE SENSOR**		Revision: B
106B52				ECN #: 33741

Performance	**ENGLISH**	**SI**	
Measurement Range(for ±5V output)	1 psi	6.89 kPa	
Sensitivity(± 15 %)	5000 mV/psi	725 mV/kPa	
Maximum Pressure(Dynamic)	10 psi	68.9 kPa	
Maximum Pressure(static)	50 psi	345 kPa	
Resolution	0.02 mpsi	.00013 kPa	
Resonant Frequency	≥ 40 kHz	≥ 40 kHz	
Rise Time(Reflected)	≤ 12.5 μ sec	≤ 12.5 μ sec	
Low Frequency Response(-5 %)	2.5 Hz	2.5 Hz	
Non-Linearity	≤ 1 % FS	≤ 1 % FS	[1]
Environmental			
Acceleration Sensitivity	≤ 0.002 psi/g	≤ 0.0014 kPa/(m/s²)	
Temperature Range(Operating)	-65 to +250 °F	-54 to +121 °C	
Temperature Coefficient of Sensitivity	≤ 0.03 %/°F	≤ 0.054 %/°C	
Maximum Shock	1000 g pk	9807 m/s² pk	
Electrical			
Output Polarity(Positive Pressure)	Positive	Positive	
Discharge Time Constant(at room temp)	≥ 0.2 sec	≥ 0.2 sec	
Excitation Voltage	24 to 27 VDC	24 to 27 VDC	
Constant Current Excitation	2 to 20 mA	2 to 20 mA	
Output Impedance	<100 ohm	<100 ohm	
Output Bias Voltage	7 to 14 VDC	7 to 14 VDC	
Physical			
Sensing Geometry	Compression	Compression	
Sensing Element	Quartz	Quartz	
Housing Material	17-4 Stainless Steel	17-4 Stainless Steel	
Diaphragm	316L Stainless Steel	316L Stainless Steel	
Sealing	Welded Hermetic	Welded Hermetic	
Electrical Connector	10-32 Coaxial Jack	10-32 Coaxial Jack	
Weight	1.2 oz	35 gm	

CE [2]

All specifications are at room temperature unless otherwise specified.
In the interest of constant product improvement, we reserve the right to change specifications without notice.

ICP® is a registered trademark of PCB Group, Inc.

OPTIONAL VERSIONS

Optional versions have identical specifications and accessories as listed for the standard model
except where noted below. More than one option may be used.

E - Emralon coating

Coating	Emralon	Emralon
Electrical Isolation	10⁸ ohm	10⁸ ohm

J - Ground Isolated   [3]

N - Negative Output Polarity

W - Water Resistant Cable   [4]
Supplied Accessory : Model 060A11 Delrin clamp nut 3/4-16-2A thd 3/4" hex (1)

WM - Water Resistant Cable   [4]
Supplied Accessory : Model 060A13 Metric Delrin clamp nut M20 x 1.5-6g thd 20 mm hex (1)

NOTES:
[1] Zero-based, least-squares, straight line method.
[2] See PCB Declaration of Conformance PS023 for details.
[3] Used with optional mounting adaptor.
[4] Clamp nut installed prior to cable attachment

SUPPLIED ACCESSORIES:
Model 060A11 Delrin clamp nut 3/4-16-2A thd 3/4" hex (1)
Model 060A13 Metric Delrin clamp nut M20 x 1.5-6g thd 20 mm hex (1)
Model 065A36 Seal, .687" OD x .625" ID x .060", Derlin (3)

Entered: omw	Engineer: NTL	Sales: Kww	Approved: GB	Spec Number:
Date: 8/24/10	Date: 8/24/10	Date: 8/24/10	Date: 8/24/10	22933

PCB PIEZOTRONICS
PRESSURE DIVISION
3425 Walden Avenue, Depew, NY 14043

Phone: 716-684-0001
Fax: 716-686-9129
E-Mail: pressure@pcb.com

F.7. Thermal probe

Data sheet
PTMTCA7
RS Stock No. 8240653
RS Stock No. 8240653

ENGLISH

Lp   35   L

Ø1

Measurment area
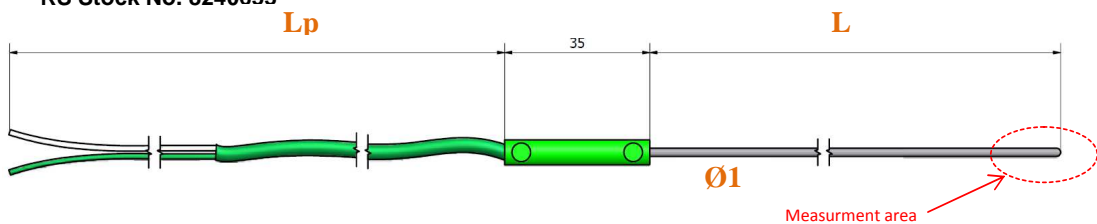
THERMOCOUPLES SHEATHED WITH MINERAL INSULATION FLEXIBLE CABLE END

RANGE :
- -50°C / +1200°C

USE :
- Universal

KEY POINT :
- Economic

SPECIFICATIONS :
- Thermocouple K type (Chromel – Alumel)
- Hot junction ungrounded
- Sheath material: Alloy 600 for 1 and 1.5mm, 310SS for Ø 3 mm
- Cable insulation : PVC/PVC
- Mineral pressed insulation
- Bendable
- Overmould transition unanswerable, Ambiante temperature : -50°C/+100°C

DIMENSIONS :
- Sheath length   - L = 150mm
- Sheath diameter = - ØD = 1.5mm
- Cable length = Lp (1 meter for Ø 1 and 1.5mm, 2 meters for Ø 3 mm)
- Transition housing = Ø 6 per length 35mm

METROLOGICAL DATA :
- As per IEC 584
  Standard tolerance TC ''K'' class 1 :
  -40°C < t°< +375°C = ± 1,5°C
  375°C < t°< +1000°C= ±0.004. [t]
- Time constant in water: Time constant in water: <5 s for Ø 3 mm, <2 s for Ø 1.5mm and 1mm
- Output signal FEM (mV) as per curve of ''K'' type as per norm

Other dimensions:

L / ØD	100mm	150mm	250mm	500mm	1000mm	1500mm	2000mm
1mm	8240635	8240644	8240647	8240641	8240650		
1,5mm		8240653	8240657	8240666	8240669	8240663	8240672
3mm		8240675	8240679	8240688	8240681	8240685	8240694

F.8. Vibration sensor
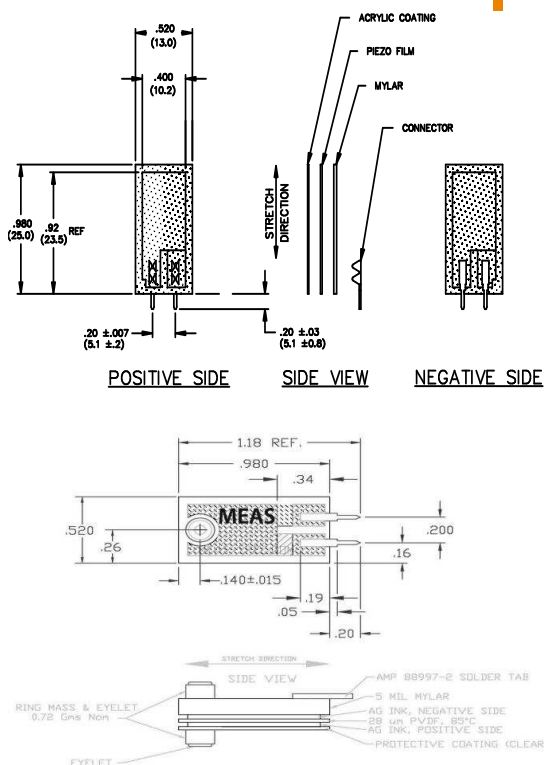
LDT WITH CRIMPS VIBRATION SENSOR/SWITCH

SPECIFICATIONS

- **Piezo Film Sensors**
- **High Sensativity**
- **AC Coupled**
- **Laminated.**
- **Robust**

The LDT0-028K is a flexible component comprising a 28 μm thick piezoelectric PVDF polymer film with screen-printed silver ink electrodes, laminated to a 0.125 mm polyester substrate, and fitted with two crimped contacts. As the piezo film is displaced from the mechanical neutral axis, bending creates very high strain within the piezopolymer and high voltages are generated. When the assembly is deflected by direct contact, the device acts as a flexible "switch", and the generated output is sufficient to trigger MOSFET or CMOS stages directly. If the assembly is supported by its contacts and left to vibrate "in free space" (with the inertia of the clamped/free beam creating bending stress), the device will behave as an accelerometer or vibration sensor. Adding mass, or altering the free length of the element by clamping, can change the resonant frequency and sensitivity of the sensor to suit specific applications. Multi-axis response can be achieved by positioning the mass off center. The LDTM-028K is a vibration sensor where the sensing element comprises a cantilever beam loaded by an additional mass to offer high sensitivity at low frequencies.

DIMENSIONS

ACRYLIC COATING
PIEZO FILM
MYLAR
CONNECTOR

.520 (13.0)
.400 (10.2)
.980 (25.0) .92 REF (23.5)
STRETCH DIRECTION
.20 ±.007 (5.1 ±.2)
.20 ±.03 (5.1 ±0.8)

POSITIVE SIDE   SIDE VIEW   NEGATIVE SIDE

1.18 REF.
.980
.34
MEAS
.520
.26
.200
.16
.140±.015
.19
.05
.20

STRETCH DIRECTION
SIDE VIEW
AMP 88997-2 SOLDER TAB
5 MIL MYLAR
RING MASS & EYELET 0.72 Gms Non
AG INK, NEGATIVE SIDE
28 µm PVDF, 85°C
AG INK, POSITIVE SIDE
EYELET
PROTECTIVE COATING (CLEAR)

FEATURES

- Solder Tab Connection
- Both No Mass & With Mass Versions
- Withstands High Impact
- Operating Temperature: 0ºC to 85ºC
- Storage Temperature: -40ºC to 85 ºC
- Higher Temperature Version up to 125 ºC available on a Custom Basis

LDT WITH CRIMPS VIBRATION SENSOR/SWITCH

APPLICATIONS

- Vibration Sensing in Washing Machine
- Low Power Wakeup Switch
- Low Cost Vibration Sensing
- Car Alarms
- Body Movement
- Security Systems

EXAMPLES OF PROPERTIES

Four different experiments serve to illustrate the various properties of this simple but versatile component.

Experiment #1

LDT0 as Vibration Sensor - with the crimped contacts pushed through a printed-circuit board, the LDT0 was soldered carefully in place to anchor the sensor. A charge amplifier was used to detect the output signal as vibration from a shaker table was applied (using a charge amplifier allows a very long measurement time constant and thus allows the "open-circuit" voltage response to be calculated). Small masses (approximately 0.26g increments) were then added to the tip of the sensor, and the measurement repeated. Results are shown in Table 1 and the overlaid plots in Fig. 1. Without adding mass, the LDT0 shows a resonance around 180 Hz. Adding mass to the tip reduces the resonance frequency and increases "baseline" sensitivity.

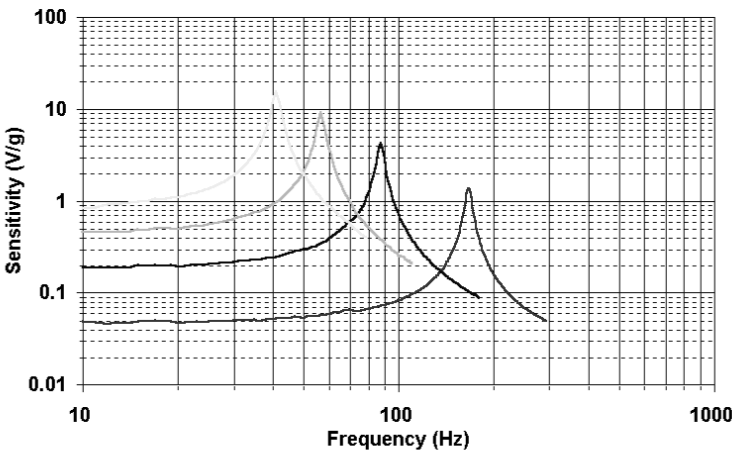**LDT0 Sensitivity: Effect of Added Mass**
(Figure 1)

TABLE 1: LDT0 as Vibration Sensor (see Fig 1)

Added Mass	Baseline Sensitivity	Sensitivity at Resonance	Resonant Frequency	+3 Db Frequency
0	50 mV/g	1.4 V/g	180 Hz	90 Hz
1	200 mV/g	4 V/g	90 Hz	45 Hz
2	400 mV/g	8 V/g	60 Hz	30 Hz
3	800 mV/g	16 V/g	40 Hz	20 Hz

Experiment #2
LDT0 as Flexible Switch - using a charge amplifier to obtain "open-circuit" voltage sensitivity, the output was measured for controlled tip deflections applied to the sensor (supported by its crimped contacts as described above). 2 mm deflection was sufficient to generate about 7 V. Voltages above 70V could be generated by bending the tip of the sensor through 90➡ (see Table 2, Fig. 2).
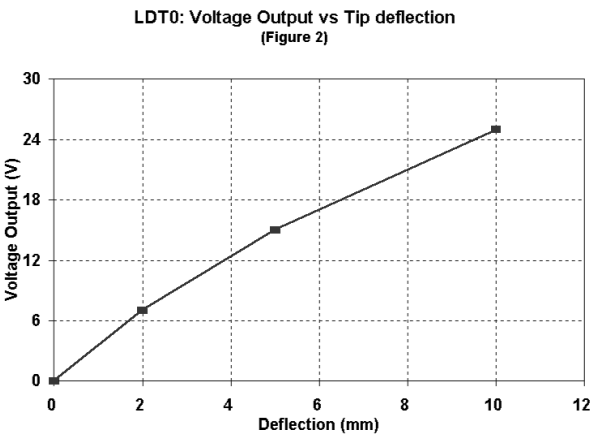
LDT0: Voltage Output vs Tip deflection
(Figure 2)

TABLE 2: LDT0 as Flexible Switch (see Fig 2)

Tip Deflection	Charge Output	o/c Voltage Output
2 mm	3.4 nC	7 V
5 mm	7.2 nC	15 V
10 mm	10 - 12 nC	20 - 25 V
max (90°)	> 30 nC	> 70 V

Experiment #3
LDT0 Electrical Frequency Response - when a source capacitance of around 480 pF is connected to a resistive input load, a high-pass filter characteristic results. Using an electronic noise source to generate broad-band signals, the effect of various load resistances was measured and the -3 dB point of the R-C filter determined (see Table 3, Fig. 3).

LDT0 Electrical Frequency Response
(Figure 3)   C: 480 pF

— 1 Megohm   — 10 Megohm   — 100 Megohm
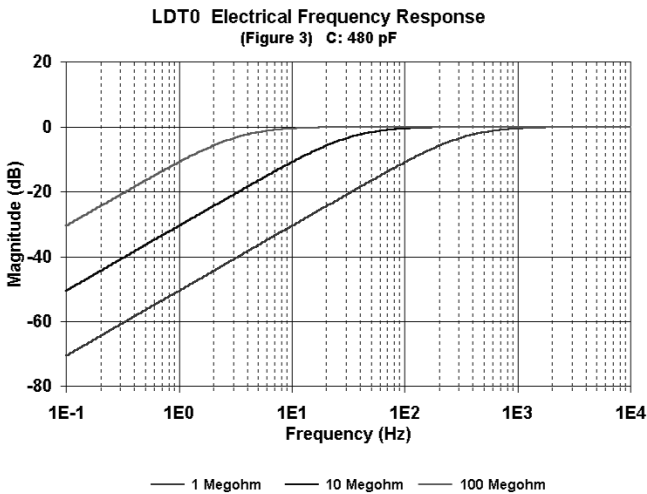
LDT WITH CRIMPS VIBRATION SENSOR/SWITCH

TABLE 3: LDT0 Electrical Frequency Response (see Fig 3)
(480 pF source capacitance)

Load Resistance	-3 db Frequency
1 Megohm	330 Hz
10 Megohm	33 Hz
100 Megohm	3.3 Hz

Experiment #4

LDT0 Clamped at Different Lengths - using simple clamping fixture, the vibration sensitivity was measured (as in (1) above) as the clamp was moved to allow different "free" lengths to vibrate. The sensor may be "tuned" to suit specific frequency response requirements (see Table 4, Fig. 4).

LDT0: Resonant Freq vs Clamped Length
(Figure 4)
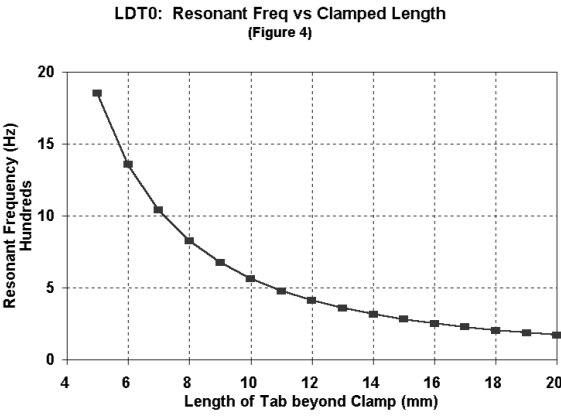
TABLE 4: LDT0 Clamped at Different Lengths (See Fig. 4)

Length Beyond Clamp	Resonant Frequency	Settling Time (5 cyc)
20 mm (no clamp)	180 Hz	28 msec
16 mm	250 Hz	20 msec
11 mm	500 Hz	10 msec
7 mm	1000 Hz	5 msec

LDT WITH CRIMPS VIBRATION SENSOR/SWITCH

ORDERING INFORMATION

Description	Part Number
LDT0-028K	1002794-0
LDTM-028K	1005447-1

NORTH AMERICA
Measurement Specialties, Inc.,
a TE Connectivity Company
Tel: +1-800-522-6752
Email: customercare.dtmd@te.com

EUROPE
MEAS Deutschland GmbH
a TE Connectivity Company
Tel: +49-800-440-5100
Email: customercare.dtmd@te.com

ASIA
Measurement Specialties (China), Ltd.,
a TE Connectivity Company
Tel: +86 0400-820-6015
Email: customercare.chdu@te.com

TE.com/sensorsolutions

F.9. Wizards of NOS solenoid valve

Highpower Systems International Ltd.

PRODUCT DATA SHEETS

Rev. Date - Nov 2013

Picture is for illustration only.

Product Detail

Part Number   : **#2457**
Name   : Solenoid X-10 350 (Pulsoid)
Description   : Direct-Acting 2-Way Normally-Closed Solenoid Valve

The X-10 series of solenoid valves have been designed as a culmination of 35 years of experience in the Automotive Nitrous Oxide injection sector. Due to the demand for ever increasing reliability, response and PWM requirements the X-10 is now highly advanced in design and materials. This now makes these solenoids suitable not only for the sector they were designed but for main stream industrial applications often out-performing and out-lasting generic solenoid valves. Our material choices allow many benefits in product life and allow a wide range of fluids to be controlled ranging from Gasoline's, hydraulics, air, water and cryogenic fluids. The efficient flow path minimises expansions which can be a benefit when dealing with cryogenic fluids that are susceptible to phase change. The following are some of the main features of the X-10 Solenoids:

- Exceptional Lifetime >1000000 operations.
- Designed for PWM flow control.
- Quick action <6μsec response time at max working pressure.
- Adjustable Plunger travel for PWM or Flow optimisation.
- High efficiency flow path – single fluid direction change from input.
- Side Entry – End Exit
- Suitable for a wide range of fluids from gases and liquids to liquefied semi cryogenic gases such as Liquid Nitrous Oxide & Carbon Dioxide.
- Exceptional core heat dissipation properties, due to the integral billet alloy body & internal core.
- Gauge/test port on input.
- Option for gauge/test port on output.
- Compact design.

Physical Data

Input Port	: 1/8th BSP *(Wide variety of outlet adapters available – see footnotes)*
Output Port	: 8 x 1mm Metric Fine *(Wide variety of outlet adapters available – see footnotes)*
Wiring	: 2 x Flying Leads of aircraft quality insulated wire (20 AWG)
Orifice	: 2.6mm [0.102″]
Plunger Lift	: 0.75mm [0.03″ - Adjustable]
Plunger Spring	: 2.5 N/mm [14.77 lbf/in]
Height	: 67.15mm [2.644″] Exc. Cap
	: 72.0mm [2.835″] Inc. Cap
Weight	: 455g [0.959 lb] Exc. input/output fittings & Exc. Cap
	: 490g [1.036 lb] Exc. input/output fittings & Inc. Cap/Bracket
Mounting	: Mounting Bracket with Cap *(Optional – 360Deg Mounting, See diagrams below)*
	: Mounting Thread *(Optional – M8 x 1.25mm Threaded hole for mounting stud)*
Wetted Material(s)	: *Core Materials*
	6262 Anodised Aluminium, Polyurethane, 303 Stainless Steel, 416 Stainless Steel, PTFE Composite coating. (Details on request).
	: *Optional Changes*
	Seals
	- Viton, Polyurethane, NBR (Alternatives on request).
	Orifice Materials
	- POM, 303 Stainless Steel.
Ambient Temperature	: -20 Deg C to +60 Deg C [-4 Deg F to 140 Deg F]
	See Electrical Data for further Information.

Dimensions
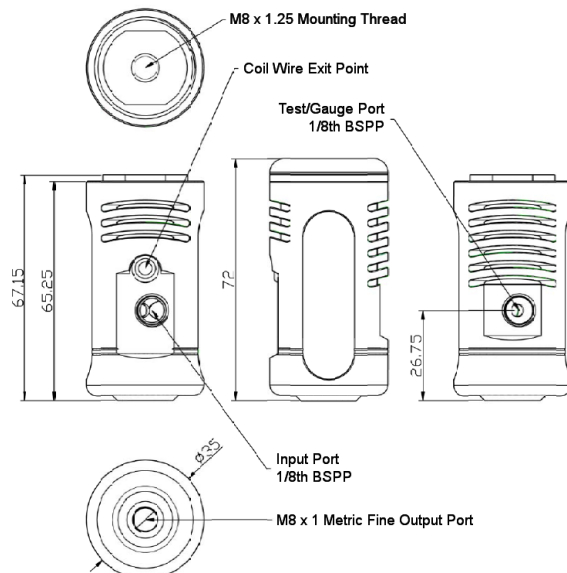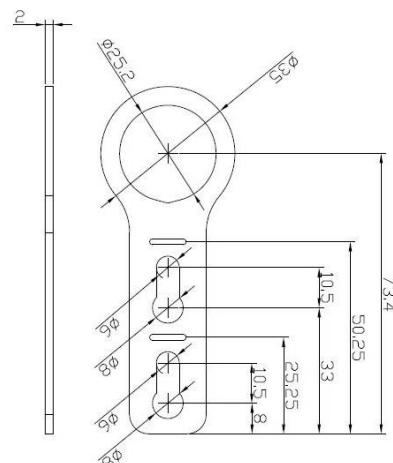
Electrical Data

Operating Voltage	:	12-16v
Power Consumption @ 12v	:	240W

Solenoid Operation

- Continuous Duty	:	Not Suitable.
- Intermittent Duty	:	Ambient Temperature 21 Deg C [69.8 Deg F]

   - On-time without fluid flow (extended use with cold media).
   - On-time without External cooling ie. Fan Assistance.

   5sec On – 15min to Ambient
   10Sec On – 28min to Ambient
   20 Sec On – 45min to Ambient
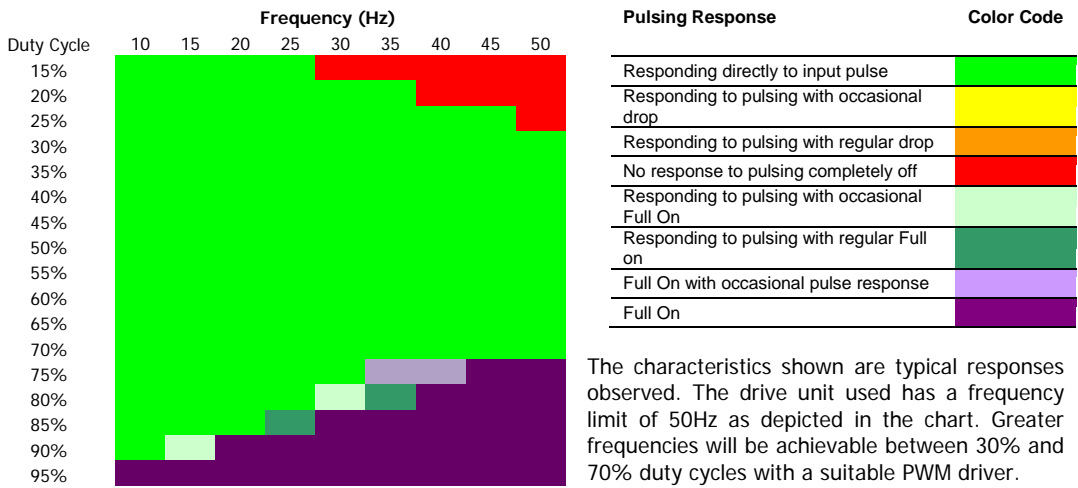   30 Sec On – 1Hr to Ambient (MAX ON TIME)

- Pulse Duty	:	5-10% Duty
Coil Resistance	:	0.8 Ω
Insulation Rating	:	Class H- 180º C
Coil Connection Wire	:	20 AWG PTFE Coated
Wiring	:	2 x Connections, Non-polarity Specific.

PWM Frequency Response Characteristics

All testing was carried out in the following environment with the variables as shown.

Ambient Temperature	:	17°C [62.6°F]
Input Medium	:	Nitrogen
Testing Pressure [68.95Bar]	:	1000 psi
Output Connection from solenoid.	:	None, direct
Power supply	:	12-14 VDC

Pulsing Response / **Color Code**

Response	Color
Responding directly to input pulse	Green
Responding to pulsing with occasional drop	Yellow
Responding to pulsing with regular drop	Orange
No response to pulsing completely off	Red
Responding to pulsing with occasional Full On	Light Green
Responding to pulsing with regular Full on	Teal
Full On with occasional pulse response	Light Purple
Full On	Purple

The characteristics shown are typical responses observed. The drive unit used has a frequency limit of 50Hz as depicted in the chart. Greater frequencies will be achievable between 30% and 70% duty cycles with a suitable PWM driver.

Flow Data

Orifice Diameter   : 2.6mm [0.102"]
Orifice Area   : 5.31mm^2 [0.00823 sqin]
Compatible Media   : Nitrous Oxide (Gas & Liquid), Carbon Dioxide (Gas & Liquid), Nitrogen (Gas)

                          The above list of Media types have been fully tested with this product. Due to
                          the corrosion resistance of the wetted materials and specification of the valve
                          internals many more media types will be suitable. Possible media's may include:

   : Water, Hydraulic Fluids, high pressure gases Etc.

Flow at Factory Max   : 1092 Lbs/Hr (Liquid Nitrous Oxide @ 65.5 Bar)

Flow Characteristics

All X-10 2-way solenoid valves are fitted with a unique and useful adjustable seat/orifice. The internal seat is
capable of being adjusted in height to shorten or increase the throw (lift) of the Solenoid Plunger. This
allows for a vast range of adjustability in flow and PWM response giving tune-ability to each solenoid. No
disassembly is required to adjust the lift height, simply use a screwdriver or flat key to adjust the height
externally through the output port.

The following chart shows the typical flow characteristics at different lift heights:

Lift Degrees	Lift (mm)	Lift (Thou)	Flow Lbs/Hr
18	0.05	0.002"	226
36	0.10	0.004"	402
54	0.15	0.006"	540
72	0.20	0.008"	653
90	0.25	0.010"	747
108	0.30	0.012"	828
126	0.35	0.014"	894
144	0.40	0.016"	948
162	0.45	0.018"	988
180	0.50	0.020"	1020
198	0.55	0.022"	1048
216	0.60	0.024"	1073
234	0.65	0.026"	1092
252	0.70	0.028"	1111
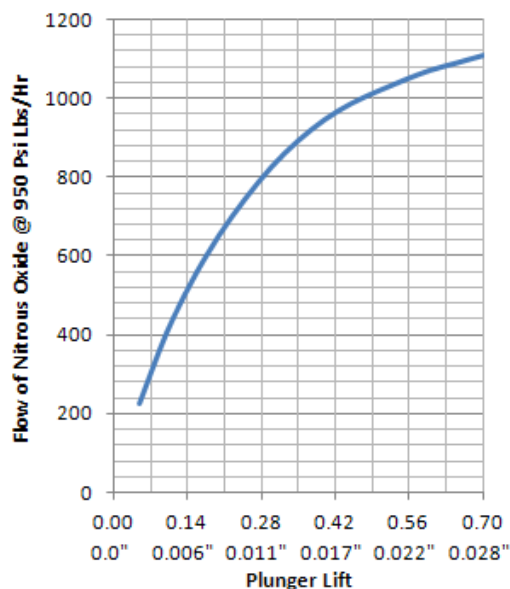
Footnotes:

Connections –

The input thread and purge ports are provided as 1/8th BSPP threaded ports. This thread should allow a significant number of off-the-shelf adapters to be fitted for flexibility of connection methods. Should fittings be required direct, numerous high quality Stainless Steel adapters are available for all inlet, purge and outlet requirements inc. Compact inline filter adapters. The following are typical adapters available to suit the X-10 range of Solenoids:

Input/Gauge Port Adapters

- -6 AN/JIC Male
- -4 AN/JIC Male
- 1/8th BSPP 60Deg Male
- 5mm Compression Fitting (M10 x 1 Female)
- 4mm Compression Fitting (M8 x 1 Female)

Adapters available to suit In-line Filter (1/4 BSPP Input)

- -6 AN/JIC Male
- -4 AN/JIC Male
- 1/8th BSPP 60Deg Male

Outlet Port Adapters

- -4 AN/JIC Male
- -3 AN/JIC Male
- 1/8th NPT Male
- 5mm Compression Fitting (M10 x 1 Female)
- 4mm Compression Fitting (M8 x 1 Female)

If the adapter required is not listed custom fittings will be available subject to order quantity.

This page was intentionally left blank

G

Technical Drawings and Illustrations

In this appendix, the dimensions for the cross-sectional geometry of the different grains can be found in appendix G.1. In appendix G.2, the technical drawing for the second iteration of the graphite nozzle can be found. The technical drawing of the steel retainer and first iteration of the graphite nozzle can be requested from the author. Lastly, the other components for this thesis were directly taken from Wubben 2022 [1, app. B].
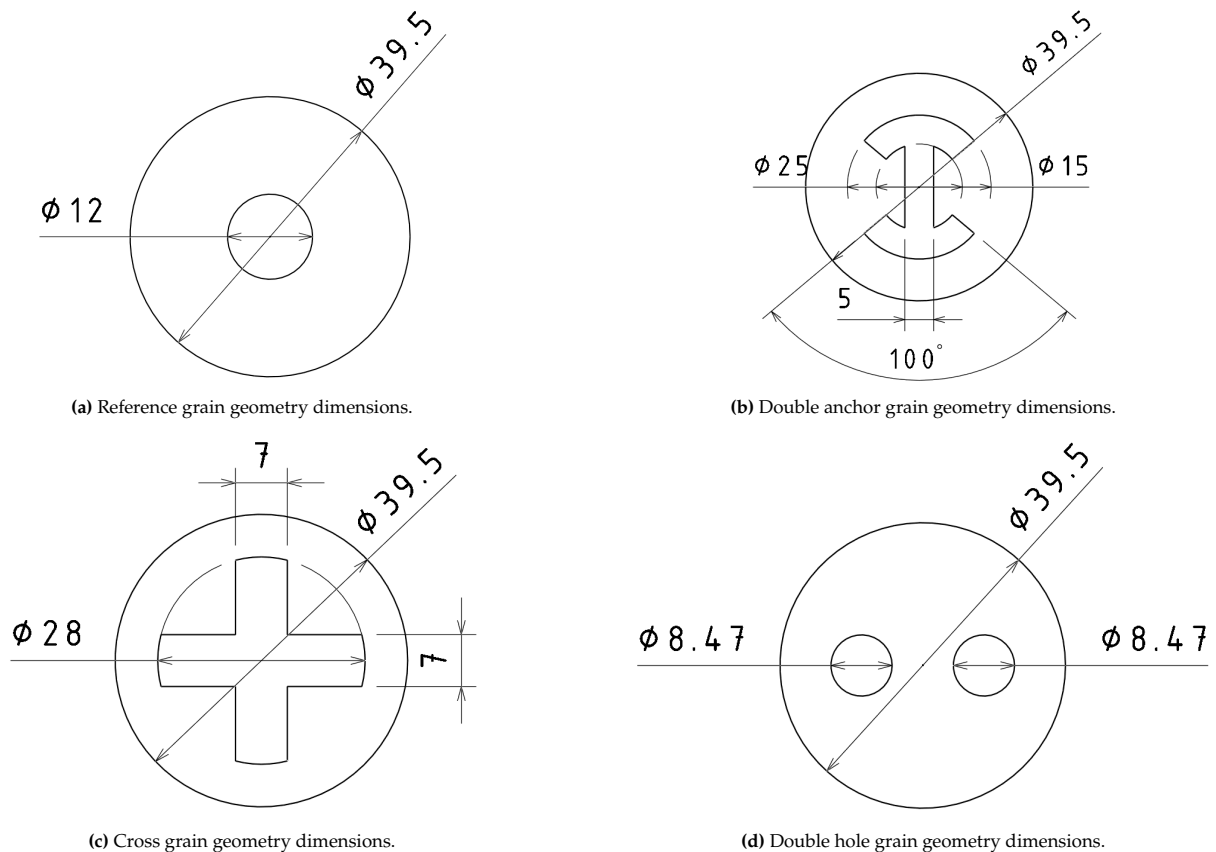
G.1. Grain geometry dimensions

(a) Reference grain geometry dimensions.
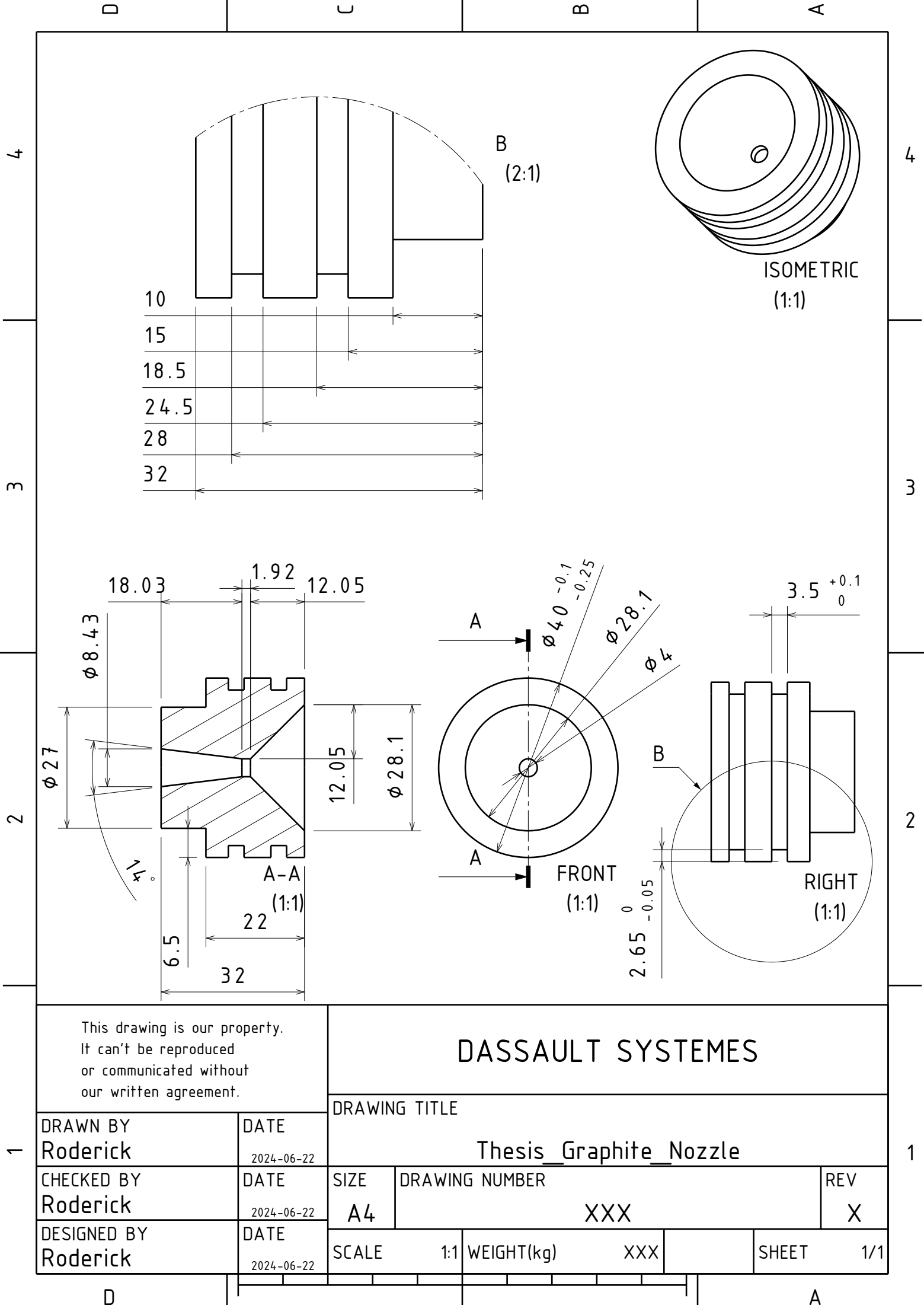

(b) Double anchor grain geometry dimensions.

(c) Cross grain geometry dimensions.

(d) Double hole grain geometry dimensions.

Figure G.1: Grain dimensions.

G.2. Graphite Nozzle v2 technical drawing

B
(2:1)

ISOMETRIC
(1:1)

10
15
18.5
24.5
28
32

18.03 1.92 12.05

Ø8.43

Ø27

Ø28.1

12.05

14°

A–A
(1:1)

22

6.5

32

A

A

Ø40 0 −0.1 −0.25

Ø28.1

Ø4

FRONT
(1:1)

3.5 +0.1 0

B

2.65 0 −0.05

RIGHT
(1:1)

This drawing is our property.
It can't be reproduced
or communicated without
our written agreement.

DASSAULT SYSTEMES

DRAWN BY	DATE	DRAWING TITLE		
Roderick	2024-06-22	Thesis_Graphite_Nozzle		
CHECKED BY	DATE	SIZE	DRAWING NUMBER	REV
Roderick	2024-06-22	A4	XXX	X
DESIGNED BY	DATE	SCALE 1:1	WEIGHT(kg) XXX	SHEET 1/1
Roderick	2024-06-22			